Windowless Gas Targets for Neutron Production

by

Erik B. Iverson

B.S. Nuclear Engineering, Iowa State University (1989)
M.S. Nuclear Engineering, Iowa State University (1990)

Submitted to the Nuclear Engineering Department
in partial fulfillment of the requirements for the degree of

Doctor of Philosophy

at the

MASSACHUSETTS INSTITUTE OF TECHNOLOGY

February 1997

Author ....
Nuclear Engineering Department
December 12, 1996

Certified by ....
Richard C. Lanza
Principal Research Scientist
Thesis Supervisor

Certified by ....
Lawrence M. Lidsky
Professor of Nuclear Engineering
Thesis Supervisor

Accepted by ....
Jeffrey P. Freidberg
Chairman, Departmental Committee on Graduate Students

Windowless Gas Targets for Neutron Production

by

Erik B. Iverson

Submitted to the Nuclear Engineering Department
on December 12, 1996, in partial fulfillment of the
requirements for the degree of
Doctor of Philosophy

Abstract

A windowless deuterium gas target has been constructed for high yield production of either monoenergetic or white fast neutrons. The operation of this target has been demonstrated on a 900 keV deuteron accelerator. The target is capable of operation at 100 mbar target pressure, and can admit a low duty factor beam of 5 mm transverse extent. The target employs an intermittent valve arrangement to reduce the flow rates in the higher pressure stages of a differentially pumped vacuum system. This valve allows operation at much greater target pressures for low duty factor beams than would otherwise be the case. Neutron yield measurements validated the functionality of the target system.

This target will make possible considerable advances in methods of non-destructive testing and evaluation which employ fast neutrons, whether mono-energetic or otherwise. It is further suited to use as a thermal neutron source, with the addition of an appropriate moderator.

The development of this target system has not only provided a functioning and valuable piece of equipment for use in further research, but has also investigated the technological limitations and functional requirements of implementing such a system in a practical setting.

Thesis Supervisor: Richard C. Lanza
Title: Principal Research Scientist

Thesis Supervisor: Lawrence M. Lidsky
Title: Professor of Nuclear Engineering

Acknowledgments

This project was supported by grants from the Federal Aviation Administration (FAA Grant 93-G-053), the United States Air Force Office of Scientific Research (F49620-93-1-0291DEF), and the Schonland Research Centre for Nuclear Sciences.

I would like to thank Doctor Wagih Makky of the FAA and Doctor Staffan Tapper and Professor John Watterson of the SRC for many constructive and inspirational discussions and ideas. I would also like to thank Doctor Robert Hamm of AccSys Technologies, Inc. for his constant help with equipment. I would further like to thank Schlumberger-Doll Research for sponsoring the Schlumberger-Doll Fellowship, which provided me the opportunity to develop this project to a level sufficient to merit directed funding.

Doctor Richard Lanza and Professor Lawrence Lidsky are also due tremendous thanks for their support and inspiration. Dennis Klein, David Fink, and Jess Iverson were of inestimable help in matters both technical and logistical. The completion of this thesis would not have been possible without the aid of Angela Myatt Quick and George FitzGerald.

Contents

1 Introduction **10**
1.1 Neutron Applications 10
1.2 Neutron Production 12
1.3 Intense Monoenergetic Neutron Sources 17
1.4 A Windowless Gas Target for Monoenergetic Neutron Production . . 19
1.5 Scope of this Study 20
1.6 Outline 21

2 Description of the Problem **22**
2.1 Design Goals 22
2.2 Design Constraints 23
2.2.1 Accelerator Description 24
2.2.2 Facility Layout 26
2.3 Previous Work 26
2.3.1 Neutron Sources 26
2.3.2 Solid Targets 26
2.3.3 Liquid Targets 30
2.3.4 Windowed Gas Targets 30
2.3.5 Sacrificial Windows 33
2.3.6 Windowless Gas Targets 33
2.4 Suggested Gas Target Design 36
2.5 Mathematical Theory 40
2.5.1 Viscous Flow 41
2.5.2 Knudsen Flow 46
2.5.3 Molecular Flow 46

3 Static Target **50**
3.1 Methodology 51
3.2 Initial Design 53
3.3 Measurements 64
3.3.1 Blocked Turbulent Flow 65
3.3.2 Blocked Laminar Flow 65
3.3.3 Transition Flow 72
3.4 Revised Design 74
3.5 Conclusions 75

4 Pulsed Target **77**
4.1 Theory 77
4.2 Factors Affecting Valve Efficiency 83
4.3 Predicted Effects 84
4.4 Valve Design 85
4.5 Valve Construction 87
4.6 Valve Performance 90
  4.6.1 Laminar Uncoupled Flow 91
  4.6.2 Turbulent Flow 94
  4.6.3 Coupled Flow 97
4.7 Attainable Pressure Drops 98
4.8 Conclusions 101

5 Gas Target Operating Experience **102**
5.1 Target Installation 102
5.2 Instrumentation 106
5.3 Predicted Yield 108
5.4 Static Target 112
  5.4.1 Gas Measurements 112
  5.4.2 Neutron Production 113
5.5 Pulsed Target 113
  5.5.1 Gas Measurements 114
  5.5.2 Neutron Production 114
5.6 Summary of Operational Results 115

6 Conclusions **116**
6.1 Success of Original Goals 116
6.2 Scalability 116
6.3 Utility of Present Target 117
6.4 Suggestions for Further Work 117
6.5 Contributions of this Thesis 118

A Safety Analysis Report **120**
A.1 Machine Description 120
A.2 Use of Facility 123
A.3 Floor Plan 123
A.4 Potential Hazards 123
A.5 Radiation Shielding 125
A.6 Estimated Dose Rates 126
A.7 Interlock System 128
A.8 Operational Procedure 130
A.9 Usage Factor 131
A.10 Credible Accidents 131
A.11 Interlock Diagram 131
A.12 Interlock Procedure 131

A.13 Emergency Shut Off Procedure 133
A.14 Measurements for d-Be neutrons 134
A.15 Modification for d-D neutrons 135
A.16 Tritium Production 136
A.17 d-D Neutron Production in the Beamline 137

B Beam Optics **138**
B.1 Theory 140
B.2 Results 142
B.3 Measurements 146

List of Figures

2-1 Floor plan of accelerator area. 27
2-2 Reaction kinematics for ^{2}H(d,n)^{3}He. 36
2-3 Angular neutron yield from d-D at 900 keV and 120 μA. 37
2-4 Angular dependence of average neutron energy. 38
2-5 Schematic of the gas target system. 39
2-6 Comparison between nozzle and tube turbulent flow. 44
2-7 Comparison between nozzle and tube laminar flow. 45
2-8 The correction factor ξ. 47
2-9 The transmission probability $\mathcal{P}$. 48

3-1 Schematic of the gas target system. 50
3-2 Naming conventions for pumping stage pressure calculations. 52
3-3 Equilibrium first stage pressure for various target pressures. 57
3-4 Pressure in the second stage as a function of that in the first stage. . 59
3-5 Third stage pressure as a function of second stage pressure. 62
3-6 Measurements and calculations for the first pumping stage. 66
3-7 Measurements and calculations for the second pumping stage. 67
3-8 Inferred flow rate through second aperture. 68
3-9 Comparison of calculated and measured pressures across the second aperture. 70
3-10 Calculated and measured flow rates across the second aperture. . . . 71
3-11 Calculated and measured Knudsen flow rates through long tubes. . . 72
3-12 Calculated and measured pressure drops across the third aperture. . . 73

4-1 Naming conventions for moving and stationary apertures. 78
4-2 First stage pressure for various target pressures and valve efficiencies 84
4-3 Equilibrium second stage pressure for various valve efficiencies 85
4-4 Third stage pressure for various valve efficiencies f_3. 86
4-5 Shop drawings for the gas target assembly. 88
4-6 Schematic of rotor and drive assembly. 89
4-7 Gas target showing installed rotor. 89
4-8 The efficiency of the rotating shutter valve in air. 92
4-9 The efficiency of the rotating shutter valve in helium. 93
4-10 The efficiency $f(g)$ of the rotating shutter valve in laminar flow. . . . 94
4-11 The valve efficiency $f(g)$ as a function of gap width g for turbulent flow. 95
4-12 The valve efficiency $f(g)$ for turbulent and laminar flow. 96

4-13 Comparison of coupled and uncoupled apertures. 97
4-14 Limiting target pressures for air. 99
4-15 Limiting target pressures for helium. 100

5-1 Timing modifications to the DL-1 for external triggering. 105
5-2 The electronics for triggering the accelerator from the rotating shutter. 106
5-3 Theoretical d-D neutron yield from the DL-1. 109

A-1 Neutron source spectrum for 900 keV deuterons on beryllium. 122
A-2 Floor plan of accelerator area. 124
A-3 Safety Interlock circuit for the DL-1 facility. 132
A-4 Thick target d-D yield for DL-1. 135

B-1 The deuteron beam without focusing. 139
B-2 Half-widths of the deuteron beam through the design HEBT system. 143
B-3 Beam profiles through the design HEBT system. 143
B-4 The effect on the beam envelopes of varying the peak beam current. 145
B-5 Beam envelopes for revised HEBT system design. 145
B-6 Beam profiles for revised HEBT system design. 146

List of Tables

1.1 Some two-body reactions used for neutron production. 14
1.2 Commercial manufacturers of sealed tube neutron generators. 15
1.3 Typical d-D and d-T target yields for 900 keV deuterons. 16

2.1 Model DL-1 system specifications. 25
2.2 Beam current through various gas cell foils. 31
2.3 Characteristics of a sample gas target system. 39

3.1 Characteristics of the gas target system. 54
3.2 Evaluation of constriction factor α for second aperture flow rate data. 69
3.3 Characteristics of a sample gas target system. 74

5.1 The differential cross section for the production of neutrons from d-D. 110
5.2 Neutron fluence rates at detector location. 110
5.3 Neutron fluence rates at detector location. 112
5.4 Static gas target pressure profiles without and with beam. 113
5.5 Pulsed gas target pressure profiles without and with beam. 114
5.6 Summary of neutron production for a target length of 270 mm. . . . 115

A.1 Model DL-1 System Specifications. 121
A.2 Dose rates at one meter due to photons coming from target. 127
A.3 The estimated dose rates at various locations. 127
A.4 Comparison of measured and predicted dose rates. 134
A.5 Comparison of dose rate predictions for d-D and d-Be. 136

B.1 Design HEBT system parameters. 144
B.2 Delivered PMQ parameters and resulting drift spaces. 144
B.3 HEBT parameters obtained by observation and manual adjustment. 147
B.4 Beam profile measurements for the HEBT system in Table B.3. . . . 147

Chapter 1

Introduction

Neutrons have many applications in modern research, medicine, and industry. Different techniques employ neutrons in different ways, and can benefit considerably through the tailoring of the energy of the neutrons used. Some techniques are intensity limited, and thus require higher rates of production, not just longer exposure times. Nearly all uses for neutrons are generally limited primarily by the strength of the neutron source. This neutron source can take the form of a charged particle-induced reaction driven by either an accelerator or decay-driven source of charged particles, a decay-driven source resulting directly in neutron production, or a reactor-based source in which the useful neutrons are drained from the dynamic balance of a critical assembly.

There is no one perfect neutron source. The particular application for which the neutrons are intended may require different energies, distributions, or quantities of neutrons to be effective. There is, however, a clear need for more intense neutron sources of all types. This thesis will examine an apparatus for the high-yield production of monoenergetic fast neutrons.

1.1 Neutron Applications

As mentioned above, neutrons have many applications in various fields. While the distinction between the various uses of neutrons can be at some times arbitrary, it is worthwhile to describe some of the more common techniques that employ neutrons.

Radiography/Tomography

Neutron transmission radiography and computed tomography are becoming increasingly widespread tools for the inspection of industrial components. [4, 5] Neutron radiography is an excellent complement to x-ray radiography, as neutrons are typically more strongly attenuated by the lighter elements (those with lower atomic numbers) than by the heavier elements—the reverse of the situation for x-rays. Furthermore, neutrons have a considerable degree of penetration, thus allowing the imaging of very large components.

Bulk Materials Analysis

Neutrons can be used for so-called bulk materials analysis, in which streams of material can be sampled to ascertain various properties important to the industrial uses of the material. For example, prompt gamma neutron activation analysis, neutron transmission, and neutron moderation can be used in the determination of the moisture content of coke and coal. [6, 7, 8] Neutron activation can also be used to determine the sulphur content in coal, and thus the ash. [9] These methods of materials analysis are quite useful as they sample a very large fraction, often approaching 100%, of the material stream (thus avoiding sampling errors), and they are done on-line, permitting rapid feedback and control of the process.

Substance Identification

Neutrons can identify many specific materials that one may wish to non-invasively detect in a qualitative sense rather than a quantitative sense, whether explosives, drugs, or some other contraband. This is in contrast to the previously mentioned methods of bulk materials analysis, in which the goal is the quantitative determination of a well-defined quantity. Here, the purpose is to determine the presence (or lack thereof) of a specific, arbitrary material or class of materials which is typically localized in a large amount of innocuous material. There is a great deal of work going on at this time in the application of neutron beams to contraband detection. [10, 11, 12, 13, 14, 15]

Condensed Matter Study

Neutron scattering, diffraction, and reflectometry are very common tools for the study of the atomic structure of condensed matter. Such methods yield information about the atomic structure of a material, whether that information concern the physical locations of the atoms, the energy which binds them into such locations, or the modification of the locations due to external influences. [16, 17] While a great deal of attention has been paid recently to large, world-class sources of neutrons for such research, [18, 19, 20, 21] smaller institutional sources can also contribute enormously. [22]

Other Applications

There are many other uses for neutrons, both established and under development. Some of them include neutron therapy for cancer treatment; isotope production for medical treatment and diagnosis, and for radiochemical analysis; neutron depth profiling; boron welding; etc.

1.2 Neutron Production

In general, neutron sources can be divided into three categories: radioisotope sources, reactor-based sources, and accelerator-based sources. Nuclear fission reactors are very commonly used sources of neutrons. [23] They can be operated either continuously or in a pulsed manner. The chain reaction that defines a fission reactor is self-sustaining, and therefore cannot be stopped as quickly as is sometimes desirable, whether this implies higher background levels between neutron pulses, or logistical difficulties with regulation and operation. Nuclear reactors are very closely regulated, and the requirements of satisfying those regulations can often be tremendous. Research reactors used for neutron production have traditionally been distinct from those used for power reactors, but are often perceptually associated with nuclear power and with nuclear weapons. Thus the current socio-political environment is extremely unfriendly towards reactor-based sources. Finally, while portable reactors do exist, [24] they typically have very small yields.

Radioisotope sources have a number of obvious advantages. They are small and very portable. They are relatively inexpensive, completely maintenance-free, and have a reliable yield of predictable intensity and spectrum. They also have significant limitations. The yield of a radioisotope source is directly proportional to its decay rate and the amount of material. High yield sources therefore require either large quantities of the relevant isotope or short decay rates. These requirements can result in the source becoming more cumbersome, expensive, or short-lived. Furthermore, all radioisotope neutron sources emit other forms of radiation as well, usually as their primary means of decay. This other radiation can complicate or preclude the use of the source. A further complication in the use of radioisotope neutron sources is that, while fission reactors can not be turned off quickly, isotope sources cannot be turned off at all.

The most common radioisotope neutron source is the isotope ^{252}Cf, which has a half-life of 2.65 years and produces 2.34×10^{12} neutrons per second per gram from spontaneous fission. All other practically usable sources are based on alpha-emitting isotopes such as ^{239}Pu, or ^{241}Am mixed with a target material, the neutrons coming from (α,n) reactions on that target material (most often beryllium). These sources have varying yields, half-lives, and spectra, but are typically not available with yields as large or as consistent of that from ^{252}Cf.

Charged particles produced by accelerators can also be used to generate neutrons. Such a source has the considerable advantage over either isotopes or reactors (even pulsed reactors) of being capable of very rapid shutdown. There are a great many two-body reactions that can practically be used in accelerator-based sources. These include some reactions which can under the appropriate conditions produce nearly mono-energetic neutrons. Some such reactions are listed in Table 1.1.

In addition to specific two-body reactions, there are also "break-up" and spal-

Reaction	Q (MeV)	Minimum Energy (MeV) Threshold	Neutron
^{3}H(p,n)^{3}He	-0.8	1.0	—
^{3}H(d,n)^{4}He	17.6	—	14.5
^{2}H(d,n)^{3}He	3.3	—	2.5
^{7}Li(p,n)^{7}Be	-1.6	1.9	—
^{7}Li(d,n)^{8}Be	15.0	—	13.3
^{9}Be(p,n)^{9}B	-1.9	2.1	—
^{9}Be(d,n)^{10}B	4.4	—	—[a]

[a]The ^{10}B nucleus has excited levels for which $Q < 0$.

Table 1.1: Some two-body reactions used for neutron production, together with their Q-values and the minimum reaction or neutron energy.

lation reactions which produce more than two reaction products. Spallation is typically taken to imply incident particle energies of greater then 100 MeV on heavy metal targets (which produce cascades of neutrons over a broad energy range from a single reaction), while there are three-body breakup reactions that set in as low as, for example, 3.7 MeV for the d-T reaction. The most significant limitations of accelerator-based neutron sources are the cost and operation of the accelerator, and the behavior of the target, which must maintain its integrity at very high levels of energy deposition.

In addition to purely technical details that differentiate the of means neutron production, there are logistical differences between them. For example, both radioisotopes and nuclear reactors have a broad base of socio-political resistance in the United States at the present time. Whether or not one feels that such resistance is justified is in some ways irrelevant; it is still very difficult to build or even relicense a research reactor, and some isotope sources (anything involving plutonium, for example) are simply unavailable. These considerations must enter into any practical discussion of neutron production. [25]

Monoenergetic neutron sources

As described above, monoenergetic neutrons can be produced by specific two-body reactions in systems which have low reaction rates for other neutron producing channels. Kinematics dictates that the energy of the resulting neutrons will be determined by the energy of the incident particle. Thus, monoenergetic neutrons may be produced by incident particles of low energy. Low energy in this case implies an energy that is small compared to the Q-value (for exothermic reactions), or very near the reaction threshold (for endothermic reactions). This obviously limits the energy of neutrons that can be produced in this way to those few discrete energies provided by the prolific neutron producing reactions. For example, the ^{2}D(t,n)^{4}He reaction has a Q-value equal to 17.6 MeV, which implies that the resulting neutrons will have an energy of 14 MeV for deuteron energies below about 1 MeV. Neutron sources of this type are quite commonly available (see the manufacturers listed in Table 1.2), but are in general limited only to 14 MeV or 2.4 MeV neutron production, as they are only practical with the d-D or d-T reactions. Not only are the neutrons produced only at given energy or energies, but they are produced completely isotropically.

Manufacturer	Model	Energy	Yield
Kaman Instrumentation Corporation Colorado Springs, Colorado	A-711	14 MeV 2.5 MeV	1×10^{11} 1×10^{9}
Martin Marietta Specialty Components, Inc. Largo, Florida	Zetatron	14 MeV	1×10^{11}
Emile Haefeley Ltd. Basel, Switzerland	n.a.	14 MeV	4×10^{12}
Cyclotron Corporation Berkeley, California	TCC4100	14 MeV	8×10^{12}
Sodern Limeil Brevannes Cedex, France	TN 46	14 MeV	4×10^{11}

Table 1.2: Commercial manufacturers of sealed tube neutron generators.

Providing the incident particle with energies comparable to the reaction Q-value will result in neutron energies which depend on the angle of neutron emission. For example, the ^{2}D(d,n)^{3}He reaction, at a deuteron energy of 5 MeV, will produce neutrons that range in energy from 1.8 to 8.3 MeV, depending upon the angle of neutron emission. Two-body reaction kinematics will not be discussed here, but such discussions can be found in any nuclear physics text. [26]

As an ion beam interacts with the target material, the energy of the ions decreases quickly, typically on the order of 100 keV/μm in metals, for example. This causes the neutrons produced from the reactions to have a spread in energy representative of the spread in the energy of the reacting ions. This broadening of the neutron energy can be limited by selecting the physical thickness of the target material so that the reduction in ion energy across the target material is small compared to the initial energy. Targets of this sort are commonly referred to as "thin" targets, as opposed to "thick" targets, in which the material thickness is greater than the range of the incident ion.

Thus monoenergetic neutrons of arbitrary energy may be produced by tailoring the incident particle energy and the particular reaction to the desired neutron energy. The energies of the incident particle and the resulting neutrons can enhance the value of one reaction over another. As an example, consider the d-D and d-T reactions at an incident deuteron energy of 900 keV. The thick target neutron yield is much greater for the d-T reaction than the d-D reaction (given the same form of target), as shown in Table 1.3. However, the thin-target monoenergetic yield of d-D is slightly greater than for d-T in the forward direction.

Reaction	Target Form	Thick Target Yield n/μC	Cross Section at 0°, mb/sr
$D(d,n)^3He$	D_2	1.1×10^5	25.7
$D(d,n)^3He$	D_2O	4.1×10^4	25.7
$D(d,n)^3He$	$TiD_{1.2}$	4.1×10^4	25.7
$T(d,n)^4He$	$TiT_{1.2}$	1.5×10^6	24.8
$T(d,n)^4He$	T_2	1.4×10^6	24.8

Table 1.3: Yields of typical target forms for d-D and d-T reactions with 900 keV deuterons. [1, 2]

White neutron sources

Of course, a thick target neutron source, which produces a broad spectrum of neutron energies, will produce more neutrons for a given incident particle beam than will a thin target source (with the same target). White neutron sources (so-called because they produce neutrons across a broad range of energies) are thus commonly used for applications in which the exact energy of the neutron is not of particular importance.

Some neutron sources are only capable of producing neutrons that would meet the definition of a white spectrum. Most isotope neutron sources, as described above, will produce neutrons with a broad range of energies. Fission reactors produce primary neutrons from the fission process, which are then very similar to those from spontaneous fission sources. Needless to say, any neutrons produced at energies greater than those desired can be moderated and/or filtered to useful energies at a penalty in intensity.

Thermal neutron sources

When such moderation is taken to the extreme case, the energy distribution of the neutrons follows the Maxwell-Boltzman distribution for the temperature of the moderating medium. The energy dependence of the neutron spectrum itself is then not determined primarily by the source reaction. However, the yield of "thermalized" neutrons, in units of thermal neutron flux per source neutron, will be higher for lower initial neutron energies, representing the decreased number of scattering collisions and attendant diffusion required to reach the ambient energy.

1.3 Intense Monoenergetic Neutron Sources

All of the neutron applications described previously are limited, both in the theoretical sense and in practical experience, by the intensity of the available neutron sources. This is especially the case for monoenergetic neutron production.

Monoenergetic neutrons, as described above, are produced by reactions between incident ions and target atoms, in which the target material causes the incident ion energy to be reduced by a relatively small amount during the traversal of the material by the ion beam. The very short range of ions in most material is a consequence of very rapid energy loss of the incident ions. This rapid energy loss also implies a very high rate of energy deposition within the target material. Thus, the production of intense monoenergetic neutron beams is limited by the deposition of large quantities of beam power in the target material, even more so than the production of white neutron beams in thick targets. This limitation is exacerbated by the fact that many uses of monoenergetic neutrons may require a physically small source point.

As will be described below, a tremendous amount of work has gone into various schemes for heat removal for targets and the maintenance of target integrity. These schemes include elaborate cooling systems, the use of highly refactory target materials, rapidly changing the position of the ion beam upon the target, and using target materials in liquid or gaseous forms. Liquid or gaseous targets can be advantageous, as they are less damaged by high heat deposition rates. Unfortunately, the state of the target material can be antithetical to the operation of the accelerator system providing the ion beam, which typically requires a reasonably good vacuum for proper operation. Such target arrangements often have windows—thin sheets or foils of solid material to rigidly define the target region and prevent the target material from corrupting the accelerator vacuum. These windows still have deleterious effects, however, ranging from heat deposition limits of their own (typically 5–50 W/cm^2), to reducing the useful ion energy (by 100-400 keV), to introducing unwanted nuclear reactions which create undesirable levels of background radiation (often on the order of 10-50% of the yield of the primary source).

A windowless gas target for monoenergetic neutron production with low-energy particle beams will allow beam currents higher than would a solid or windowed target, and thus will provide greater neutron yield. The primary characteristic of such a target is that there is a pressure change from the target to the accelerator covering several orders of magnitude. This pressure difference is supported by one or more stages of differential pumping through beam guide tubes with very small gas conductances. A windowless gas target will also provide a cleaner source spectrum of neutrons, especially important in monoenergetic neutron production, as many window materials not only result in a deterioration of the ion energy and energy width, but also contribute large quantities of reaction products (including neutrons) to the radiation produced by the target system.

1.4 A Windowless Gas Target for Monoenergetic Neutron Production

A great many uses of monoenergetic neutrons as described above require an intense source of neutrons in the energy range of 2–10 MeV. Presently available systems that can provide neutrons in this energy range cannot do so at a great enough intensity or with great enough reliability for the research and industrial uses under development. The purpose of this thesis is to develop a target system that can be used to produce 2—10 MeV neutrons at a very high rate. As part of other ongoing research projects at MIT, there is an accelerator (Model DL-1, from AccSys Technologies, Inc., Pleasanton, California) operated by the Nuclear Engineering Department which can produce up to 120 μA of 900 keV deuterons. This accelerator, which will be described in greater detail below, can be used to test such a target and demonstrate its characteristics. Such an accelerator can, when used with a deuterium target system, provide neutrons from 1.78–4.02 MeV with the yield and line width determined by the form and thickness of the target and the angle of emission.

Deuterium is the target material of choice for a number of different reasons. First of all, the d-D reaction allows access to a useful range of neutron energies. The d-D reaction is the most prolific thin target reaction at the 900 keV deuteron energy produced by the available accelerator. Deuterium is the only target material (with the exception of tritium) for deuteron-induced reactions which is readily available in a pure gaseous material. Tritium, which has obvious advantages as a target material for lower energy ions, loses these advantages at higher ion energies. Furthermore, deuterium is far easier to use than is tritium, because of the concerns surrounding radiological protection from the tritium gas.

This thesis describes a windowless deuterium gas target for the DL-1 machine described above, which can provide a well-defined beam of monoenergetic fast neutrons. The target is capable of long term operation at pressures sufficient for adequate target thickness in a reasonable space. As will be described below, this requirement implies a pressure of at least 150 mbar. The DL-1 accelerator facility, as currently installed, can provide a beam footprint of approximately 5 mm diameter at the desired target location.

1.5 Scope of this Study

The purpose of this work is to determine whether or not a windowless differentially pumped D_2 gas target of pressure greater than 150 mbar can be constructed in such a way as to accept a 5 mm diameter beam spot. Such a target will be scalable to a broad variety of beams from a number of different types of accelerators. Deuterium will provide a desirable target not only from the point of view of the neutron production from it, but also because it is one of the most challenging gasses from which to build such a target (in every way except radiological). Thus, the experience gained from such a target will be applicable to targets using other gasses, including ordinary hydrogen, tritium, helium, oxygen, nitrogen, or argon. If it is determined that such a target is feasible, it will be built and tested upon the existing accelerator facility.

The main goals of the project are to:

1. explore the accuracy of standard methods of gas dynamic calculations for differential pumping systems,

2. provide a windowless D_2 gas target capable of operation at 150 mbar or greater for use with the DL-1 accelerator, and

3. demonstrate the feasibility of such targets which can be scaled up to much greater power/energy/current with a minimum of effort.

1.6 Outline

Chapter 2 describes the problem of constructing a windowless gas target, and examines the goals of and constraints on this project. Chapter 2 also examines previous work in this area, and the theory behind the low-pressure flow of gasses through small orifices. Chapter 3 describes the theoretical calculations and experimental measurements surrounding the design and testing of a static gas target system. Chapter 4 describes an apparatus for the reduction of gas flow across a differentially pumped aperture, and its implementation in a practical gas target system. Chapter 5 outlines the experimental measurements performed with the resulting gas target system as installed on the DL-1 accelerator system.

Chapter 2

Description of the Problem

The construction of a windowless gas target for monoenergetic neutron production with the DL-1 accelerator facility and demonstration of the feasibility of such a target implies a certain set of goals, and must satisfy a number of constraints. The enumeration of both the goals and constraints will serve to determine the direction of the design.

2.1 Design Goals

Qualitative goals which the design must meet include:

- no physical window separating the target region from the accelerator region during the injection of the deuteron beam; as described previously, and will be elaborated upon below, a thin window unacceptably limits the yield of the neutron source by limiting the amount of beam current (for a given energy) that can be delivered to the target,
- a lack of significant radiological contamination of the target system; this forbids, in practical terms, the use of tritium as a target material, and encourages the use of pumping technology that does not bring radioactive reaction products into intimate contact with pump oils,

- reasonably inexpensive and safe operation; this requires recirculation of the target gas,
- reasonably useful as a "point" source of either monoenergetic or white fast neutrons,
- reasonably scalable to considerably higher-yield beams

These qualitative goals determine the quantitative goals of the project. As the range of a 900 keV deuteron in D_2 gas is approximately 50 mm·bar, a thick target region of 300 mm length implies a target pressure of at least 150 mbar. A 300 mm long target region, in which the beam is approximately 5 mm in diameter, provides an aspect area of 26 mm for a viewing angle of 5°. The thick target yield is strongly forward-biased, so any use of the target as a white neutron source would indeed use the 0° emission. If the neutrons were to be thermalized, a 300 mm source would be of a reasonable size when compared with any reasonable storage moderator. A 900 keV deuteron beam will suffer an energy loss of 50 keV over 4.5 mm·bar, which implies an interaction length of 30 mm at 150 mbar. This is small enough to be considered a reasonable "point" source of monoenergetic fast neutrons.

Finally, the gas target must admit an ion beam which maintains a maximum size of approximately 5 mm over the length of the set of differentially pumped apertures—approximately 400 mm. This figure is determined from the beam calculations which appear in Appendix B. It is also generous enough that nearly any beam of similar energy produced from a practical accelerator should be capable of being focused to nearly that extent.

2.2 Design Constraints

The dominant constraints in the construction of the gas target system will be the physical nature of the existing DL-1 facility. The accelerator available is a 900 keV deuteron machine. It has no provision for focusing the accelerated beam, and produces a pulsed beam of several milliamperes peak current with a duty cycle of less than 2%.

The accelerator is further described in Section 2.2.1. The accelerator is installed in an existing concrete vault which cannot be modified to any great degree. This vault is described in Section 2.2.2. The source must be operable in such a way that radiation protection concerns within and around the vault are satisfactorily met. Guidelines for radiation protection are given in the Analytical X-Ray Equipment Safety Program, provided by the MIT Radiation Protection Office. [27] The safety report for the neutron source facility is detailed in Appendix A.

2.2.1 Accelerator Description

The AccSys Model DL-1 Linac Neutron Generator system is a compact Radio Frequency Quadrupole (RFQ) linear accelerator (linac) that accelerates deuterium ions to an energy of 900 keV and bombards a beryllium target to produce neutrons. This final deuteron energy cannot be varied. The Model DL-1 Linac Neutron Generator was specifically designed as a replacement for the Kaman A-711 sealed neutron generator tube which utilizes the D(d,n) reaction. The pertinent operating parameters for the Model DL-1 are listed in Table 2.1.

The Model DL-1 Linac Neutron Generator produces a positive ion beam by the ionization of deuterium gas in a duoplasmatron ion source. The ion source and the power supplies required to operate it are isolated at 25 kV. This voltage results in an ion beam being extracted from the plasma in the ion source anode and accelerated across the high voltage gap through the grounded extraction electrode. The extracted deuterium ion beam (80–90% d^+, 10–20% d_2^+) exits from the accelerating gap through an aperture in the extraction electrode and is focused into the RFQ linac by an electrostatic einzel lens.

This source is designed to produce 10^{10} neutrons per second from a beryllium target. The filament and ion source are designed to produce up to 10 mA of peak current. The figure of 10^{10} neutrons per second is based on the 120 μA (time-averaged) of beam current produced by operation at the typical operating point of 2% duty factor with 6 mA peak current. The beryllium target consists of a 0.75 mm thick disk of beryllium brazed to a copper disk at the end of a 25 mm diameter, 150 mm long

Accelerated Particle	d^+	
Operating Frequency	425	MHz
Input ion energy	25	keV
Final ion energy	900	keV
Acceptance (normalized)	0.04	π cm-mrad
Current limit	21	mA
Final synchronous phase	-28.0	degrees
Average bore radius	1.60	mm
Maximum vane modulation	2.26	
Intervane voltage	45.0	kV
Maximum surface gradient	38	MV/m
Cavity RF power (w/o beam)	39.5	kW
Vane length	726	mm
Total length	1.016	m
RF drive loop	1 5/8"	coaxial
System weight	450	lbs
Vacuum pumps (2)	8"	cryopumps
Design input current	5–15	mA
Input emittance (normalized)	0.02	π cm-mrad
Beam transmission at 10 mA	> 90	%
Output energy spread (90%)	$< \pm 15$	kV
Beam pulse length	5–100	μsec
Cavity fill time	2	μsec
Pulse repetition rate (max)	640	Hz
Total RF power	48	kW
Maximum Duty Cycle	2.00	%

Table 2.1: Model DL-1 system specifications.

stainless steel tube. This target will be replaced by the deuterium gas target in the course of this project.

2.2.2 Facility Layout

For this target to be tested, and the project to satisfactorily demonstrate its success, the target must be installed in the existing neutron source facility, using the existing accelerator system. The facility in question is a concrete vault with 0.81 m walls. It has a monolithic concrete door 0.61 m thick, and auxiliary rooms for accelerator setup and control.

The accelerator is installed in room NW13-038b, with the target assembly in room NW13-020 (the vault). There are two beam ports in the walls, both fourteen inches in diameter. One of the ports opens into room NW13-038b, and one into NW13-038a. This second room (NW13-038a) is used for another accelerator by a different group. The floor plan of the area appears in Figure 2-1

2.3 Previous Work

2.3.1 Neutron Sources

Neutron sources in general are a very broad and extensive topic, and will not be considered further here, as exhaustive references are readily available. [28]

2.3.2 Solid Targets

Stationary Targets

The most frequently used solid target using hydrogen isotopes is titanium-tritide with a tritium-to-titanium ratio of approximately 1.7. [29] Tritide target yields decrease markedly with operation time due to tritium depletion in the target, tritium diffusion (enhanced by deuterium implantation), tritium desorption (which takes place at 200°C for titanium and zirconium, and 450°C for yttrium, scandium, and erbium),

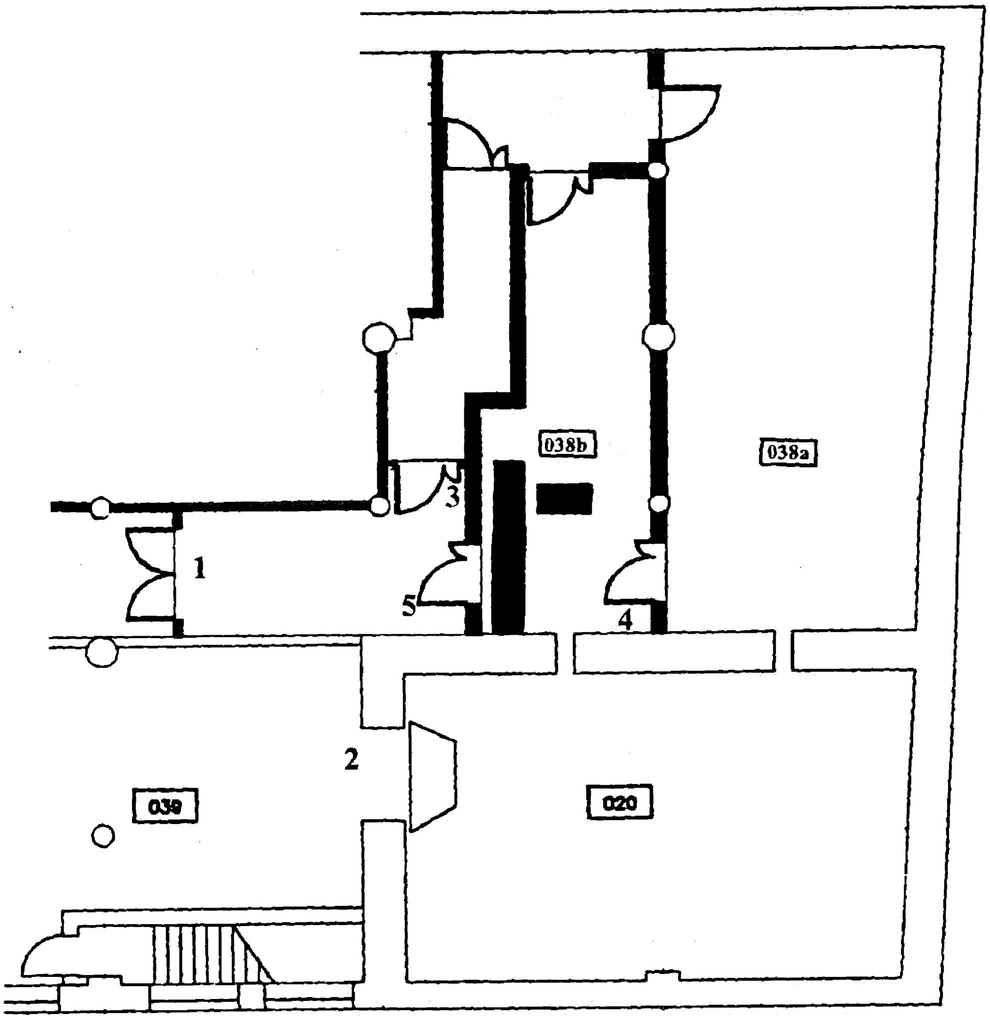

Figure 2-1: Floor plan of accelerator area showing new construction for DL-1 installation.

target sputtering (primarily due to contaminating ions in unanalyzed beams), target oxidation (due to oxygen contamination in the ion beam), and target carbonization (due to vacuum pump oil contamination of the beam line). Typically, target lifetimes run to about 3 mA·h/cm^2 for unanalyzed beams, and 20 mA·h/cm^2 for analyzed beams. These targets also have a contaminating neutron source of 2.8 MeV neutrons resulting from the d-D reactions between deuteron ions in the beam and previously implanted deuterium atoms in the target. This contamination from deuterium buildup reaches saturation after several hours of operation. The yield and spectrum shift can be avoided by using a mixed deuterium-tritium beam. This results in a more consistent neutron source, although the d-D contamination is still present.

Bacon et al. [30, 31] describe a a 14 MeV neutron source developed for research on cancer therapy. The test facility consisted of a 200 mA d.c. 200 keV deuterium beam on a scandium deuteride target which produced 1.1×10^{11} neutrons per second. This scales to 1×10^{13} neutrons per second from a mixed DT beam on a ScDT target. In this case, the d-D contamination was not of concern. This facility exemplifies a very common practice, which is the use of d-D system to accurately model a d-T system without the difficulties attendant upon the use of tritium.

Metal tritide targets, as mentioned above, will lose tritium once the temperature of the target begins to exceed about 250°C for zirconium or titanium, and 450°C for erbium or scandium. With reasonable one-sided cooling schemes, this typically implies power limitations of about 0.15 and 4 kW for a 1 cm^2 beam spot (for stationary targets). [32]

Sealed neutron tubes, which use a mixed DT beam and continually recycle the gas in a completely sealed system, have been commercially available and quite popular for some time. [29] Typical yields from d-T tubes are as high as 10^{12} neutrons per second, with ion energies approaching 400 keV, and currents approaching 500 mA (often from multiple ion sources). These tubes will generally contain as much as 100 TBq (3 kCi) of tritium, and have lifetimes of up to 10000 hours (see Table 1.2 in Section 1.2).

Rotating Targets

To deal with the large quantities of heat deposited by high current low energy beams, target systems in which the target continually presents a "fresh face" to the incoming beam have been used (rotating targets), as have beams that are scanned across a stationary target (so called "flying spot" targets). Typical limits for beam power in rotating tritide targets are as high as 100 kW/cm^2.

One such target was the Rotating Target Neutron Source (RTNS) at Lawrence Livermore National Laboratory. The RTNS facility had a 20 mA 400 keV deuteron beam impinging upon a 230 mm diameter target that rotated at 1100 rpm. [33] The externally cooled target was composed of tritiated titanium. This source produced 6×10^{12} neutrons per second from a 6 mm beam spot. The target inventory was approximately 2 kCi of tritium, and the typical target lifetime was 100 hours.

The RTNS-II facility [34, 35, 36] operated at 150 mA and 370 keV, and produced 3.7×10^{13} neutrons per second from a 10 mm beam spot. It used a 500 mm TiT_2 disk rotating at 3500 rpm. Obviously, a significant part of both the RTNS-I and -II target designs involved the vacuum seal that permitted rotation at speeds of thousands of rpm.

The OKTAVIAN facility at Osaka University uses a 20 mA beam of 300 keV deuterons on a Ti-T target. The 15 mm beam spot produced 3×10^{12} d-T neutrons per second from a 200 mm target rotating at 400 rpm. This target contained some 400 Ci of tritium, and had a typical lifetime of one amp-hour. [37, 38]

The LANCELOT facility in Valduc, France is a rotating target source which produced 6×10^{12} neutrons per second from a 160 keV 200 mA dc deuteron accelerator. The target region was some 50 mm in diameter, leading to a instantaneous average heat load of 1.63 kW/cm^2, which in practice ranged from 1.2–10 kW/cm^2. [39] The target had a typical lifetime of seven hours.

2.3.3 Liquid Targets

The FMIT neutron source was designed to use a 100 mA, 35 MeV deuteron beam incident upon a liquid lithium target.[40] The SUPER-FMIT was a proposed upgrade to the postponed FMIT design, involving 1 A of accelerated beams. This source was intended to provide high fluxes (on the order of 10^{16} neutrons per square centimeter per second of fast neutrons (8–12 MeV) over large volumes (8 cm^3).

The NBINS system was a proposal for a source of fusion-like neutrons to use for materials testing. [29] This system involved a 50 A mixed D-T space-charge-neutralized beam at 120 keV impinging on a liquid lithium target. The system also examined pure tritium beams on lithium deuteride or deuterium gas targets. This system took advantage of the very large neutral beam injection systems developed for magnetic fusion energy programs.

2.3.4 Windowed Gas Targets

The most common use of gaseous materials as targets involves the presence of a thin window intended to contain the target gas while causing minimal degradation in the beam characteristics. Typically, window materials are metals with high strength at elevated temperatures. Such windows degrade the quality of the source by several mechanisms, including the reduction in the energy and the energy width of the incident beam, reactions between the beam and the window materials, and reactions between the beam and target gas that diffuses into the window material. The energy deposited in the window material by the beam is a limiting factor in use of the window, as the window will typically burst in some more or less catastrophic fashion at high densities of deposited energy. Diffusion of the target material into the window is also accelerated at higher beam power. Typical window materials include Havar, stainless steel, platinum, gold, tungsten, titanium, and nickel. [41, 3]

Foil Type	Thickness		Max. Current w/o permanent leak (μA)	Power in foil at maximum current (W)	Current at onset of diffusion leak[b] (μA)
	(μm)	(keV)[a]			
Mo	5.0	222	20	4.4	15.5
Mo	10.0	444	10	4.4	—[c]
W	8.0	513	17	8.7	15.0
Havar	2.5	114	10	1.1	6.5
Ni	2.5	120	< 5	< 0.6	—[c]

[a] Energy loss of a 4 MeV proton.

[b] Pressure in gas cell falling at rate of approximately 40 torr/hour.

[c] Diffusion not observed prior to development of permanent leak.

Table 2.2: Beam current through various gas cell foils for a 4 MeV dc proton beam of 4 mm diameter passing through a gas cell filled with 1100 torr of D_2 gas. Taken from Carlson. [3]

Window Integrity

Considerable study has gone into the failure of gas target windows, especially those used to define tritium gas targets. The typical modes of window failure include diffusion leak, pinhole rupture, and catastrophic disintegration. One study used a 4 MeV dc proton beam to test molybdenum, tungsten, Havar, and nickel foils for failure modes. Table 2.2, taken from Carlson [3] shows the beam current at which various modes of failure occurred for 4 mm beam spots of varying current. Tests with a more sharply focussed beam (1 mm diameter) developed pinhole leaks at one-half the currents indicated in Table 2.2.

Mostafa [41] describes a system with pairs of nickel windows at both the entrance and exit of a tritium gas cell. The space between the pairs of windows was filled with flowing helium used to cool the windows. The cooling gas also provided a straightforward means of monitoring the gas target for tritium leaks. This target also relied upon a "defocusing" window (Havar of 2.2 μm thickness) to guarantee a larger beam spot on the actual target window. The nickel windows, of 12.7 μm thickness, could tolerate 15 μA of 10.2 MeV protons at target pressures of 3 atm with a cooling gas flow of 10 ℓ/min, but was in practice used 1.3 atm for 5 hour irradiations at 5 μA currents. The targets showed no sign of damage after 50 hours of irradiations.

However, approximately 20 μCi of tritium was lost through the window into the flow of cooling gas. The initial pair of windows and the cooling gas flow between them degraded the beam energy by 4 %.

Ongoing experiments at the Schonland Research Centre with 2.5 μm foils of Havar indicate that a 5 mm beam spot of 1.5 μA of 5 MeV deuterium causes the window to rupture catastrophically within 2 minutes at gas pressures of 2 bar. [42] However, further experiments with 2.5 μm Havar windows on 4 bar helium targets cooled to liquid nitrogen temperatures permit operation with 25 μA of 1.2 MeV deuterium in a 5 mm beam spot of 1–5 hours. The rupture is mild; a pinhole develops at the hot spot, allowing the gas to gently escape. [42]

Window performance can be enhanced by supporting the window with a metal grid. This grid, which does block out some of the beam, provides both physical support and additional cooling capacity to the foil. One such project [43] used a gold grid with 1.34 mm square holes separated by a 0.25 mm web, resulting in a transmission of about 75 %. These grids were made covering areas of up to 1.5 cm^2. This particular target diffused a (smaller) beam spot over the large window to reduce the average power density. Nickel windows of thickness from 1.8–3.5 mg/cm^2 (2.0–3.9 μm) would regularly survive for 24 hours at about 15 μA of deuteron current, with repeated cycling of the target pressure from 0–2 atm. Steady pressures and lower currents would allow lifetimes as long as 100 hours.

Alternatively, some study has been made of liquid windows for gas targets. Rostek et al. [44] describe a mercury vapor jet produced by a Laval nozzle. This jet covered an aperture of 1 cm^2 area with a target pressure of up to 36 mbar. However, the "vacuum" supported downstream of the window was no better than 0.1 mbar.

Source Degradation

An additional concern in the use of windowed targets is the degradation of the source characteristics by the production of "wrong-energy" neutrons and photons in the entrance and exit windows. Meadows [43] shows time-of-flight spectra from d-D experiments that indicate that the ratio of "right" to "wrong" neutrons (more accurately, the ratio of yields without gas to yields with gas) increases from approximately 2% at deuteron energies of less than 2 MeV to greater than 20% at deuteron energies of 7 MeV. These experiments were done with evacuated target cells and filled cells. Thus, the background neutrons measured were from (d, n) reactions which occurred in the nickel, gold, and tantalum which composed the window, grid, and aperture, respectively. By contrast, Cramer [45] measures the yield of protons on a tritium gas target when filled with gas and immediately after evacuation of the target following prolonged use. This study demonstrated that the bulk of the background neutron production from the molybdenum target was actually due to p-T reactions within the molybdenum foil, into which tritium was diffusing at a significant rate. The experiments also demonstrated that the diffusion of the target gas into the beam stop at the end of the gas cell resulted in significantly less neutron production than the gas in the entrance foil. Klien [46] performed a detailed analytical study, together with Monte Carlo simulations and experimental measurements, of the energy and angle broadening seen in the window of a gas target system.

2.3.5 Sacrificial Windows

For particularly short pulses at low frequency, a system has been proposed which involved a metallic foil seal that is pierced by the particle beam. [47] Between pulses, the foil is advanced to reseal the opening between the stages. This system was intended for 100 ns pulses at frequencies of about 1 Hz.

2.3.6 Windowless Gas Targets

Many of the difficulties of using gas targets are centered around the window material (background, energy sharpness, energy level, rupture). Furthermore, a static target shows a considerable change in local gas density as a function of beam current, changing the yield, average energy, and resolution of the neutron production. For one case [43], this effect resulted in a 30% decrease in the source strength when the temperature of the target gas went from 30°C to 180°C. These effects are not typically seen with windowless gas targets flowing at relatively high speeds. [48] Windowless gas targets have been examined many times before, especially with the goal of providing a very high intensity source of fast neutrons.[49, 50, 51, 52]

Colombant [49] at MIT performed a theoretical study of a high intensity 14 MeV source in which the neutrons were to be produced via the t-D reaction. The deuterium target was the large density gradient which occurs at the sonic line of a free-jet expansion. The heat deposited by the incoming tritium beam was carried out of the target volume by the flow of deuterium. This allowed the power density within the target to be several orders of magnitude greater than that in conventional targets. The system modeled included a 1 A 400 keV dc tritium beam and a hypersonic wind tunnel through which flowed deuterium gas. The source produced 10^{15} neutrons per second in a volume of one cubic centimeter. The expelled deuterium went through an isotopic separation system to extract the deposited tritium. The tritium was then recycled to the ion source, and the deuterium to the target. The design required some 50 kCi of tritium. There were many complications associated with the hypersonic jet, but the goals of the design required such a target to achieve a very localized fast flux. Additional work was performed at MIT over the next decade examining the effect of high rates of energy deposition within a free-jet expansion on the expansion.[53, 54] Further work on the effect of beam heating on gas flows was performed at the University of Toronto [50], where a six-stage differentially pumped target was explored.

A project to build such a source a Los Alamos National Laboratory was attempted [52]. Prototype experiments [55] promised good results for the 1.1A 300 keV tritium beam. This design had a tritium inventory of 290 kCi. The project was abandoned before construction began. [29]

A somewhat related source was built at the University of Wisconsin [51, 56]. This source was meant to produce 14 MeV neutrons for radiotherapy. The source was a windowless tritium target bombarded by a 3.6 mA 210 keV dc deuteron beam, which produced 10^{12} neutrons per second. This target, unlike Colombant's, was a low-pressure flow of gas (10 mbar), separated from the accelerator vacuum system by a set of differentially pumped apertures. This device had an inventory of 150 Ci of tritium [29]. The exhausted target gas was recirculated, but not isotopically separated. The yield of the target decreased with a half-life of two hours, due to tritium-hydrogen exchange in the gas manifold/pumping system. [51]

One can also find a good deal of information surrounding gas targets for experiments with optical radiation. These experiments sometimes use gas targets defined by windows, as do particle beam experiments. However, there are no bulk materials which transmit at shorter wavelengths than the 1050 Å cutoff of LiF.[57] For experiments with shorter wavelength light, windowless gas targets are required for any power levels. Differentially pumped slits are often used to avoid the drawbacks associated with thin windows of material that suffer at higher power levels, and are not particularly rugged or effective even at lower power levels. Capillary arrays, on the other hand, provide a large rugged window into a gas cell. These arrays have been made of perforated stainless steel plates or small diameter glass capillaries in tightly packed arrays.

In addition to requiring pressure gradients, these optical experiments sometimes involve very expensive gases. Some windowless systems have been constructed with the goal of reducing the flow rate of the target gas into a laser medium, both for expense and for maintaining the quality of the lasing material. One such system[58] used a rotating disk valve to reduce the flow rate across a small pressure gradient. Such a valve is useful if (and only if) the system involved operates with a low duty factor.

Bussiere and Robson [59] describe a differentially pumped gas target for use in spectroscopy, where both sides of the gas cell are pumped. This provides a thin target with very little background from the downstream reactions.

Localized gas densities of several hundred mbar can be obtained by the use of pulsed jets of various sorts. The gas is not defined by any physical barrier at all, but is merely "puffed" into the path of the beam. Kung et al. [60] describe one such system. A similar system is described by Sanna et al. [61], which uses a programmable valve to deliver pulses of gas. This system was able to deliver pulses of gas having a rise time of about 45 μs and durations of 250 μs (FWHM) and greater. It was also operated as a beam chopper with frequency in the range 0–270 Hz. This article did not discuss the actual pressure in the vicinity of the nozzle during the pulse.

2.4 Suggested Gas Target Design

We have examined several characteristics of differentially-pumped windowless gas targets employing the D-D reaction, which has a positive Q-value of 3.28 MeV. This reaction produces neutrons that are, for the thin target case, kinematically collimated. The relationship between incident deuteron energy, neutron energy, and neutron direction is shown in Figure 2-2.

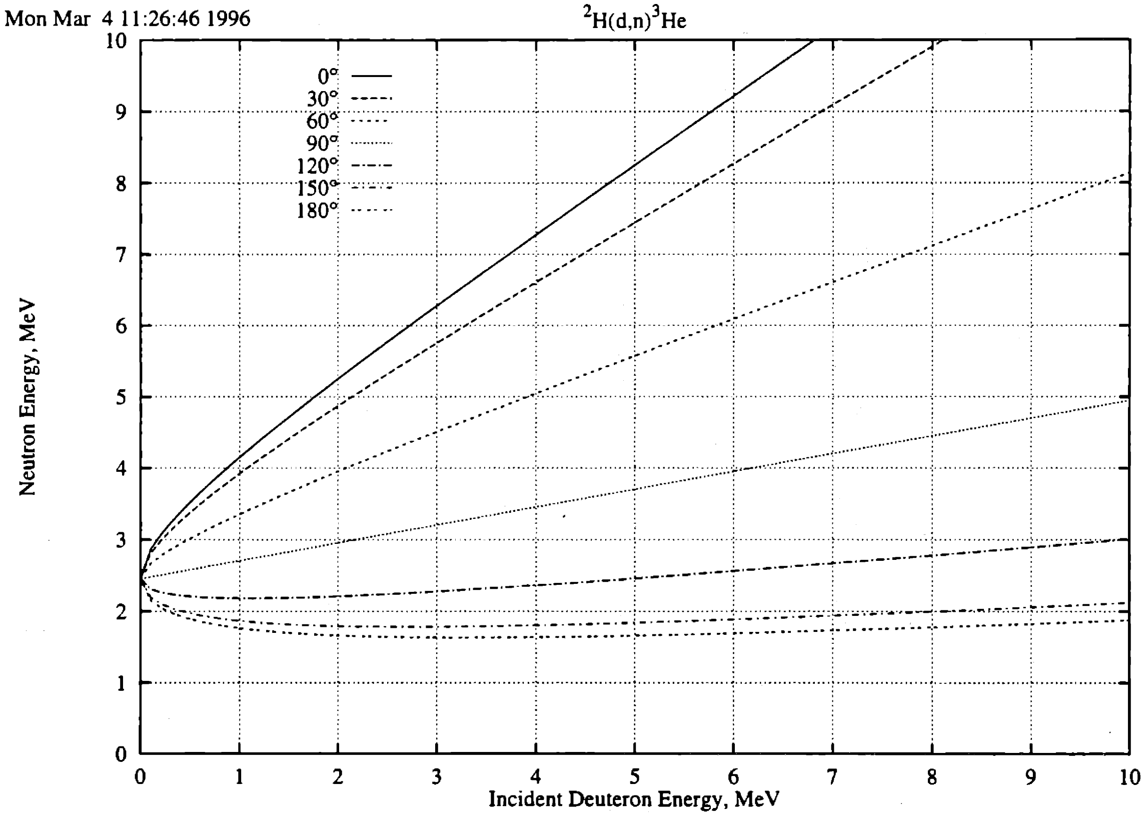

Figure 2-2: Reaction kinematics for ^{2}H(d,n)^{3}He.

This target system was designed for use with an AccSys Technologies, Inc. DL-1 accelerator. This accelerator is commercially available as a neutron generator that uses a thick beryllium target for neutron production, and is further described in

Section 2.2.1. This Radio Frequency Quadrupole (RFQ) machine will supply 6 mA of 900 keV deuterons with a duty factor of 2%. The thick target yield from 120 μA of 900 keV deuterons on D_2 is shown as a function of angle in Figure 2-3. The total yield is 1.48×10^{10} neutrons per second at the maximum current available from the machine of 120 μA (time-averaged). The average neutron energy from the thick target source is 2.71 MeV. The dependence of neutron energy on angle is shown in Figure 2-4. The target we have constructed was also intended to demonstrate the feasibility of such a target in general, and can easily be installed or scaled to a different machine.

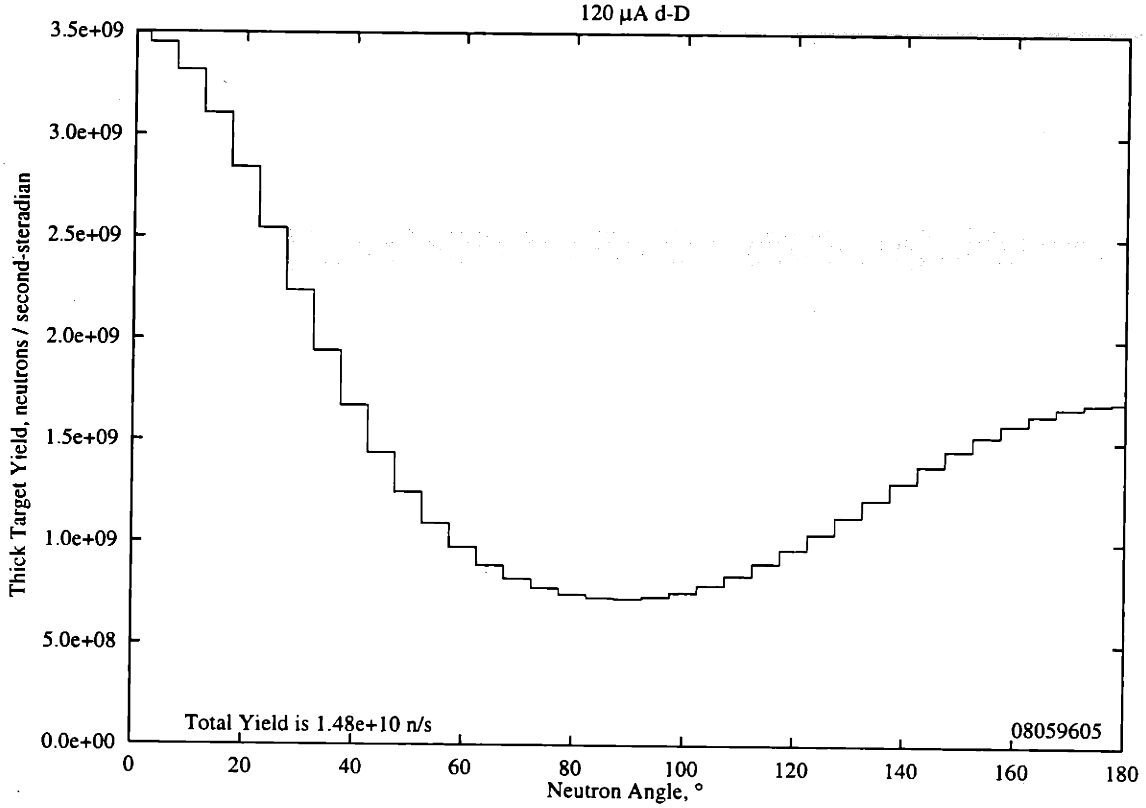

Figure 2-3: Angular neutron yield from d-D at 900 keV and 120 μA.

The differentially pumped gas target consists of three pumping stages. The goal of the design is to have a target pressure of greater than 150 mbar, and an accelerator pressure of no more than 1.33×10^{-6} mbar. The target region is separated from the accelerator by four differentially pumped apertures. A vacuum pump is situated between each pair of apertures. A rough schematic of the target system appears

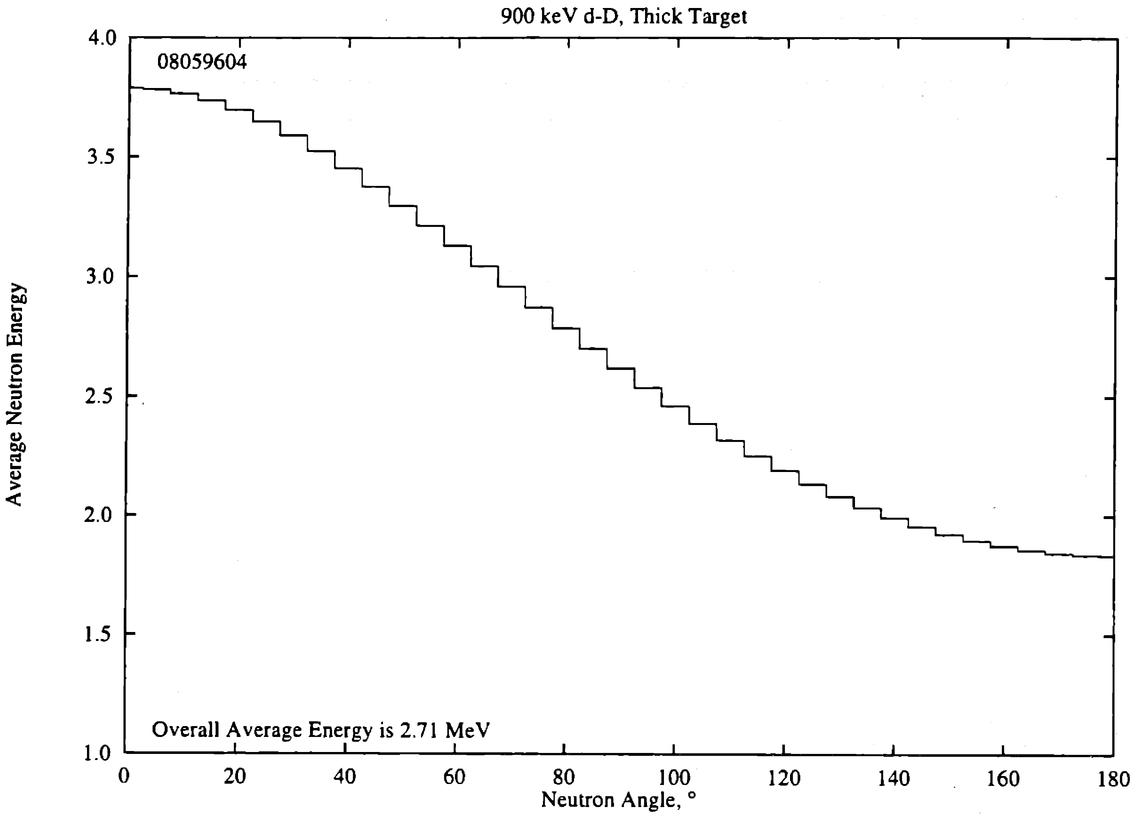

Figure 2-4: Angular dependence of average neutron energy.

in Figure 2-5. The conductance of the apertures between stages determines the flow rate that takes place through the apertures. For example, consider a deuterium target with a pressure of 200 mbar that exhausts through an aperture 25 cm long and 0.5 cm in diameter to a pumped chamber at less than 25 mbar; the flow through the aperture is viscous, turbulent, and blocked (as will be shown later). The flow rate into the pumped chamber will be 1.89 bar·liter per second. This flow rate, the flow rate out of the chamber into the next pumped chamber (which can be calculated in much the same way), and the throughput of the first stage's pump determine the pressure that will be maintained in that stage. For this case, a Roots blower capable of pumping speeds on the order of 1000 m^3 per hour at pressures up to 8 mbar will give a pressure of 6.55 mbar in the first pumping stage. All of these calculations assume that the gas flow is constant and steady over time.

This process can be repeated for the remaining stages of the target. To continue

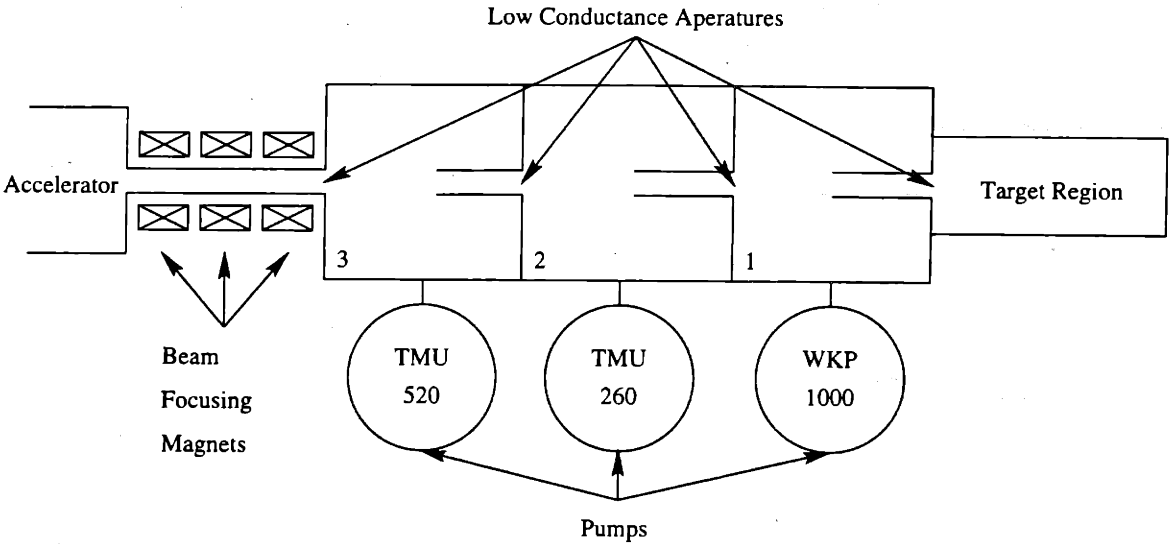

Figure 2-5: Schematic of the gas target system.

the target described above, consider a system in which all apertures have a diameter of 0.5 cm. The first aperture is 25 cm long, and the remaining apertures are both 10 cm long. For this particular case, the target will have the parameters shown in Table 2.3. This target design offers a unique advantage for modeling the behavior of other target systems. The flow through each differentially pumped aperture is in a different flow regime; transition, laminar, and turbulent. This permits study of the important parameters of nearly any target system.

Stage	Pressure (mbar)	Pump Type	Inlet Pressure	Capacity (at pressure)	Entrance		Pump	
					l	d	l_K	d_K
Target	2.00×10^{2}	—	—	—	—	—	—	—
1	6.55×10^{0}	Roots	6.55×10^{0}	278 l/sec	25	0.5	10	16
2	1.68×10^{-1}	Turbo	1.68×10^{-1}	250 l/sec	10	0.5	10	10
3	1.90×10^{-4}	Turbo	1.34×10^{-4}	560 l/sec	10	0.5	10	10

Table 2.3: Characteristics of a sample gas target system. Dimensions are in centimeters.

2.5 Mathematical Theory

Flow in a vacuum (which can be defined as a region in which the gas pressure is anywhere between 10^{-12} mbar and 10^3 mbar) depends on whether the gas flows as a continuum or as a collection of independent molecules. If the gas flows as a continuum, its molecular structure may be disregarded, and the flow is termed viscous, as the viscous forces (the forces between molecules in a fluid) are dominant. If the gas flows as a collection of independent molecules, where there is little interaction between the molecules of the gas, the flow is termed molecular. This distinction is quantified by the Knudsen number, denoted Kn, defined as

$$Kn = \frac{\lambda}{d}, \tag{2.1}$$

where λ is the molecular mean free path of the gas, and d is the characteristic physical dimension of the system, e.g., the width of the flow channel. If $Kn < 0.01$, the flow is considered viscous, while if $Kn > 0.5$, it is considered molecular. The region where $0.01 < Kn < 0.5$ is defined as Knudsen flow. A simpler metric to use in determining the flow characteristics through a tube is the product of the pressure in the tube with the diameter of that tube. If this product is greater than 0.6 mbar·cm, the flow is considered to be viscous, while $p \cdot d < 0.01$ indicates that the flow is molecular.

Viscous flow can be further differentiated into laminar and turbulent flow. Laminar flow is characterized by flow which takes place in layers. At higher flow velocities these layers are destroyed by particles of the fluid moving from one such layer to another, which is known as turbulent flow. The Reynolds number Re is used to distinguish laminar flow from turbulent flow. It is defined as

$$Re = \frac{\rho \cdot v \cdot d}{\eta}, \tag{2.2}$$

where ρ is the density of the fluid, v is the mean flow velocity, d is again a characteristic physical length, and η is the dynamic viscosity of the gas. Laminar flow is typically considered to have $Re < 2300$, while turbulent flow is considered to have $Re > 4000$.

Flow in which $2300 < Re < 4000$ is termed transition flow.

Finally, the velocity of sound in a gas provides an upper limit to the flow velocity of the gas through a tube of constant cross section. Such flow is defined as critical, or blocked, flow. A very important characteristic of blocked flow is the Mach cone; the shock wave that demarks the location where the flow velocity reaches the velocity of sound. This shock wave is the crucial part of the gas target design, as it provides a very sharp density gradient in the gas flow at a specific location.

The different flow regimes require different relationships to describe the flow rates between two chambers of different pressure. As was mentioned, blocked flow conditions limit the flow rate for viscous flow. In our system, we will therefore attempt to have blocked flow across every differentially pumped aperture in the viscous flow regime.

2.5.1 Viscous Flow

Nozzles

For viscous flow through a nozzle whose diameter is small compared to its length, the exit pressure at which blocked flow occurs, defined as the critical pressure p^*, is given by

$$\frac{p^*}{p} = \left(\frac{2}{\kappa+1}\right)^{\kappa/(\kappa-1)} . \tag{2.3}$$

The corresponding critical flux is

$$q^* = Ap\left(\frac{2}{\kappa+1}\right)^{1/(\kappa-1)} \sqrt{\frac{2\kappa}{\kappa+1} \cdot \frac{RT}{M}}, \tag{2.4}$$

where A is the minimum flow area of the nozzle. This flow area A is often somewhat smaller than the geometrical area $\pi d^2/4$ of the nozzle. Constriction factors α of 0.7–0.9, in agreement with experience, are typically used. [62, p. 84]

For air at 20°C, we then have

$$q^* = 15.7\alpha d^2 p, \tag{2.5}$$

using units of cm, mbar, and mbar·ℓ/s. For gasses other than air, this flux should be multiplied by the ratio of the viscosity of air to the viscosity of the gas, approximately equal to the square root of the ratio of the molecular masses. For deuterium, Equation 2.5 then becomes

$$q^* = 42.2 a d^2 p. \tag{2.6}$$

In the case of helium, one must nominally change the value of κ from 1.4 to 1.67, as helium is monatomic. However, performing this substitution into Equation 2.4 changes the constant appearing in Equation 2.6 from 42.2 to 42.5 (less than 1%). As a result, one can in general assume that helium and deuterium will behave identically in such circumstances.

Long Tubes

In the case of turbulent viscous flow through long smooth tubes, the critical pressure p^* is given by

$$\frac{p^*}{p} = \frac{4.51 \cdot \left(\frac{d^3 p^2}{2l}\right)^{4/7}}{d \cdot p}, \tag{2.7}$$

where p is the pressure in the chamber, and d and l are the diameter and length, respectively, of the tube; all pressures are in millibar, and all lengths in centimeters. The gas flux (for air) under these conditions is

$$q^* = 134 \cdot d \cdot \left(\frac{d^3 \left(p^2 - p^{*2}\right)}{2l}\right)^{4/7}, \tag{2.8}$$

where q^* is in millibar·liters per second.

For laminar viscous flow, the critical pressure is [62]

$$\frac{p^*}{p} = 2.3 \cdot \frac{d^2}{l} \cdot p, \tag{2.9}$$

and the gas flux (air) is

$$q^* = 135 \cdot d \cdot \frac{d^3}{l} \frac{p^2 - p^{*2}}{2}. \tag{2.10}$$

The pumping speed of a pump, S, is reduced if the pumping takes place through a flow restriction such as a tube. The effective pumping speed S_K at the chamber is given by

$$\frac{S_K}{S} = \frac{p}{p_K} = \frac{1}{\sqrt{1+x}}, \tag{2.11}$$

where p is the pressure in the chamber, and p_K is the pressure at the pump inlet. For a circular tube of length l and diameter d, the value x is

$$x = 0.32 \left(\frac{\pi}{4}\right)^{-7/4} \cdot \eta^{1/4} \cdot \left(\frac{RT}{M}\right)^{-3/4} \cdot \frac{lS^2}{d^5} \cdot \left(\frac{pS}{d}\right)^{-1/4} \tag{2.12}$$

for turbulent flow, and

$$x = \frac{2 \cdot 128 \cdot \eta l_K S}{\pi d_K^4 \cdot p_K} \tag{2.13}$$

for laminar flow, where M is the molar mass of the gas, R is the gas constant, and T is the gas temperature.

The Reynolds number, defined in Equation 2.2, can also be calculated as

$$Re = \frac{4M}{\pi \eta RT} \cdot \frac{q}{d}. \tag{2.14}$$

It is instructive to compare the flow rate through a short nozzle with the flow rate through a long tube. Figure 2-6 shows the effect of tube length on critical fluxes of air for tubes (turbulent flow) and nozzles of various diameters at a constant upstream pressure. An equivalent comparison for laminar flow through tubes appears in Figure 2-7. Note that in neither case does the tube flow approach the nozzle flow as the tube length approaches zero.

Figure 2-6 clearly shows several things. First of all, the equations for flow through long tubes clearly become non-physical at lengths $l < 100 \cdot d$. This is in conflict with Wutz [62], who claims that the "long" criterion is satisfied for l/d ratios of greater than approximately 50. Additionally, however, one sees that the advantage of going to long tubes, especially if one is referring to the range $l/d < 100$, is somewhat marginal, giving reductions in flow rates on the order of 10% or less. Finally, one sees that the effect of decreased flow diameter is far greater than the effect of increased length, as one might expect from Equation 3.7.

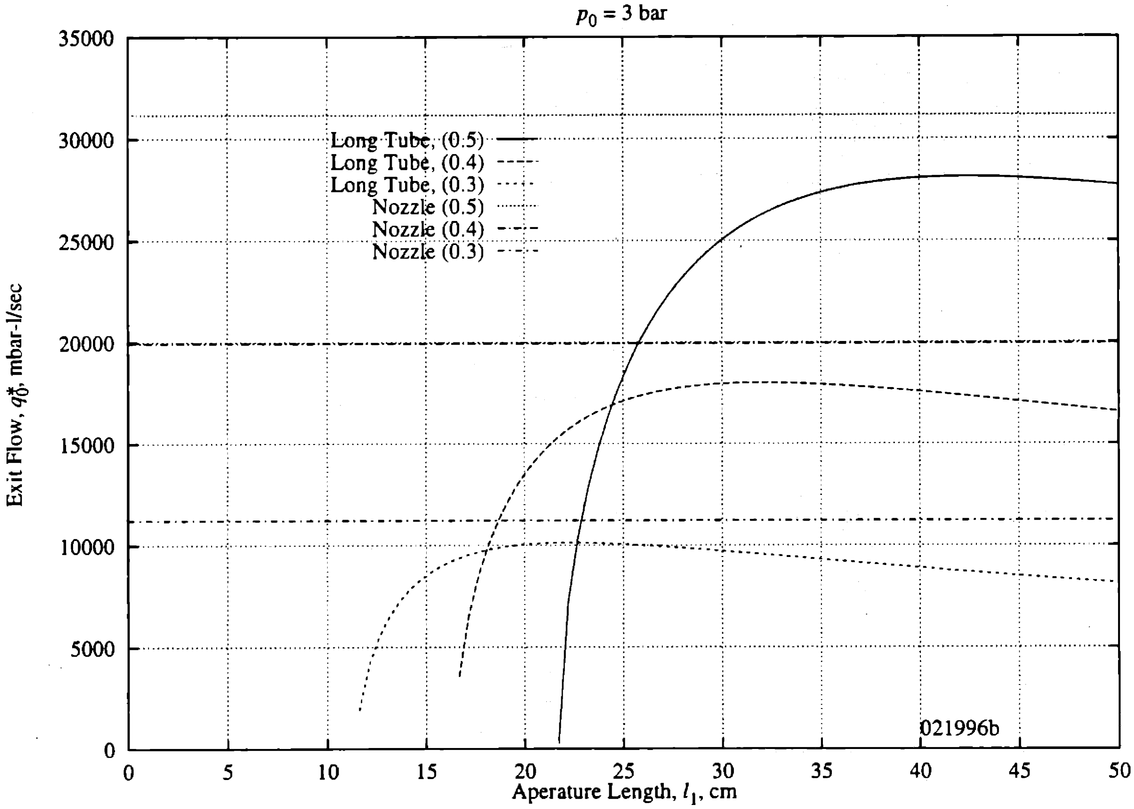

Figure 2-6: Comparison between blocked nozzle flow and blocked turbulent tube flow for air.

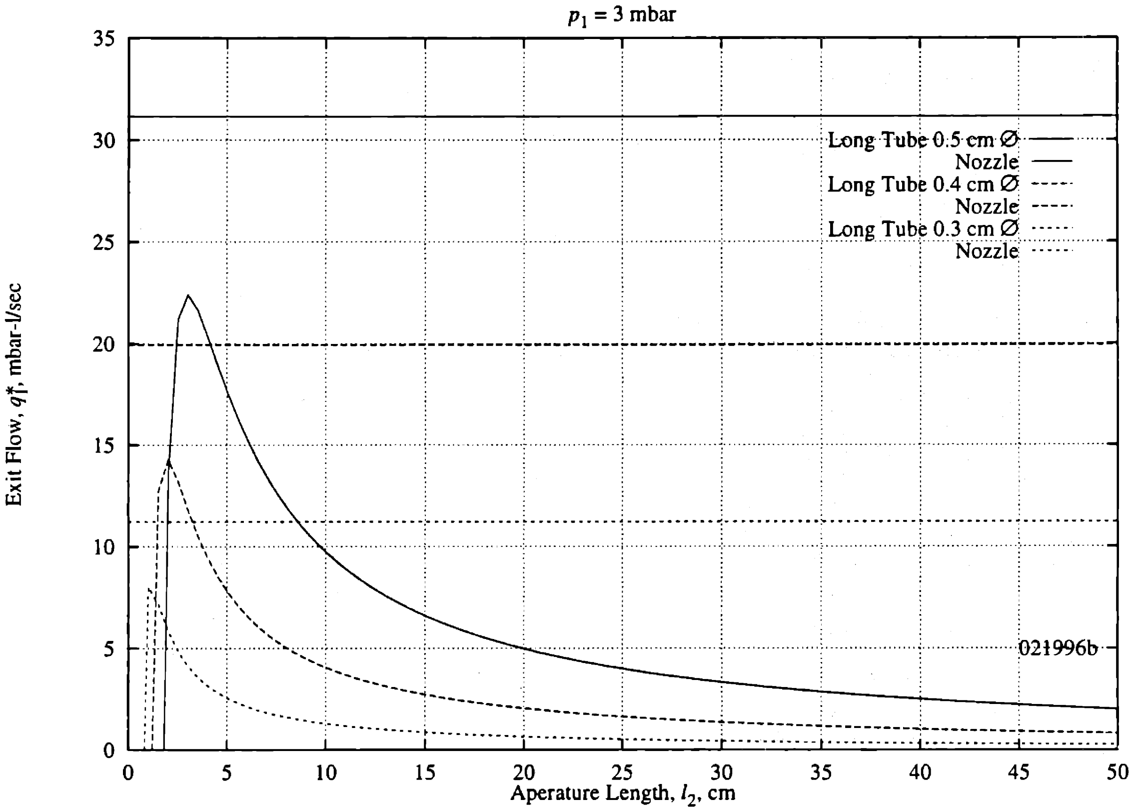

Figure 2-7: Comparison between blocked nozzle flow and blocked laminar tube flow for air.

2.5.2 Knudsen Flow

For Knudsen flow through a long tube of diameter d and length l between pressures p_u and p_d, where $p_u > p_d$, the gas flow rate is given by [62]

$$q = \frac{\pi}{128} \cdot \frac{d^4}{\eta l} \cdot \frac{(p_u - p_d)^2}{2} + \frac{1}{6} \cdot \sqrt{\frac{2\pi RT}{M}} \cdot \frac{d^3}{l} \cdot \frac{1 + \sqrt{\frac{M}{RT}} \cdot \frac{d}{\eta} \cdot \frac{p_u + p_d}{2}}{1 + 1.24 \cdot \sqrt{\frac{M}{RT}} \cdot \frac{d}{\eta} \cdot \frac{p_u + p_d}{2}} \cdot (p_u - p_d). \quad (2.15)$$

Equation 2.15 is independent of the units used—none of the numeric constants are dimensional.

2.5.3 Molecular Flow

Nozzles

In the molecular flow regime the conductance L_e of a thin-walled orifice is given by

$$L_e = \frac{\bar{c}}{4} A, \quad (2.16)$$

where $\bar{c}$ is the mean gas particle velocity, equal to 464 m/s for air at room temperature.

The flow rate through the orifice is

$$q = L_e(p_u - p_d), \quad (2.17)$$

where p_u is the pressure upstream of the orifice, and p_d is the pressure downstream of the orifice.

Long Tubes

The conductance L of a long tube in the molecular flow regime can be calculated by first calculating the value for the conductance of the entrance of the tube, L_e, as in the previous section. This conductance is then scaled by a transmission probability

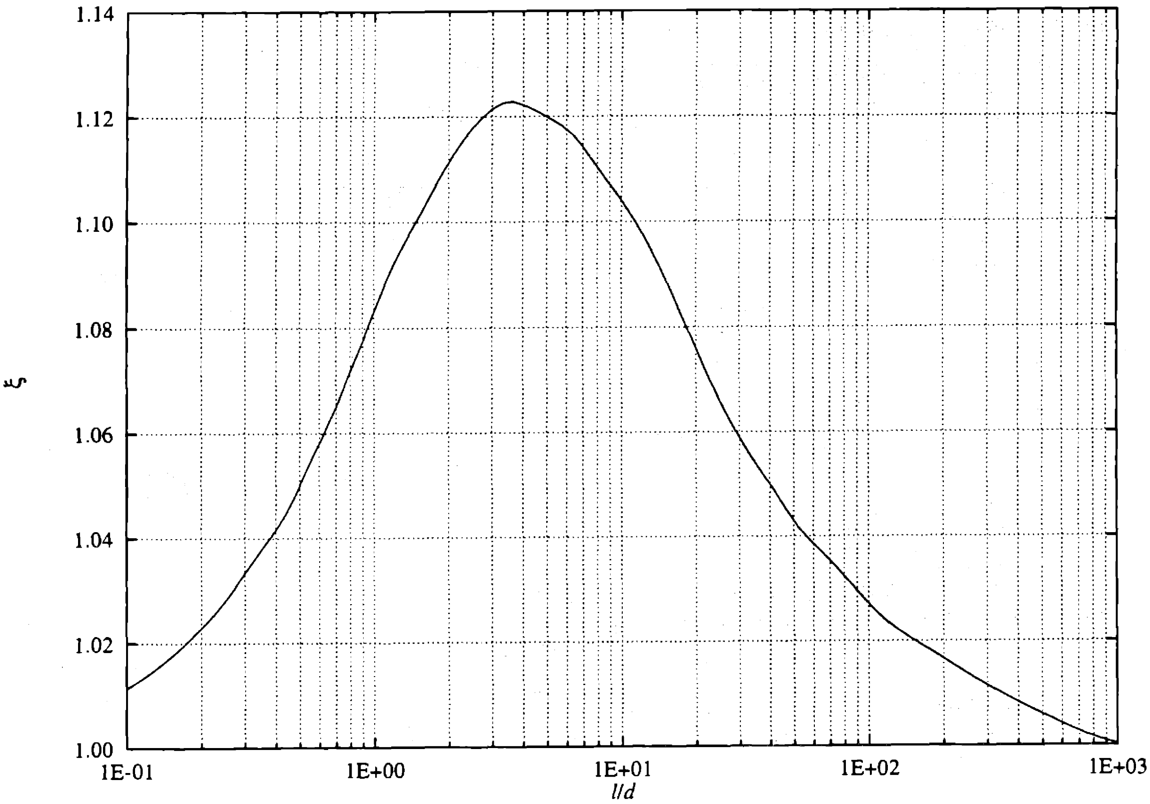

Figure 2-8: The correction factor ξ used in Equation 2.19.

$\mathcal{P}$,

$$L = L_e \cdot \mathcal{P}, \tag{2.18}$$

which is calculated from the ratio of length to diameter of the tube,

$$\mathcal{P} = \left(1 + \frac{3}{4}\frac{l}{d}\right)^{-1} \xi^{-1}, \tag{2.19}$$

where ξ is a tabulated correction factor, dependent on l/d. The correction factor ξ is given in Figure 2-8, taken from Wutz et al. [62] The transmission probability appears in Figure 2-9.

The flow rate through that long tube is

$$q = L(p_u - p_d), \tag{2.20}$$

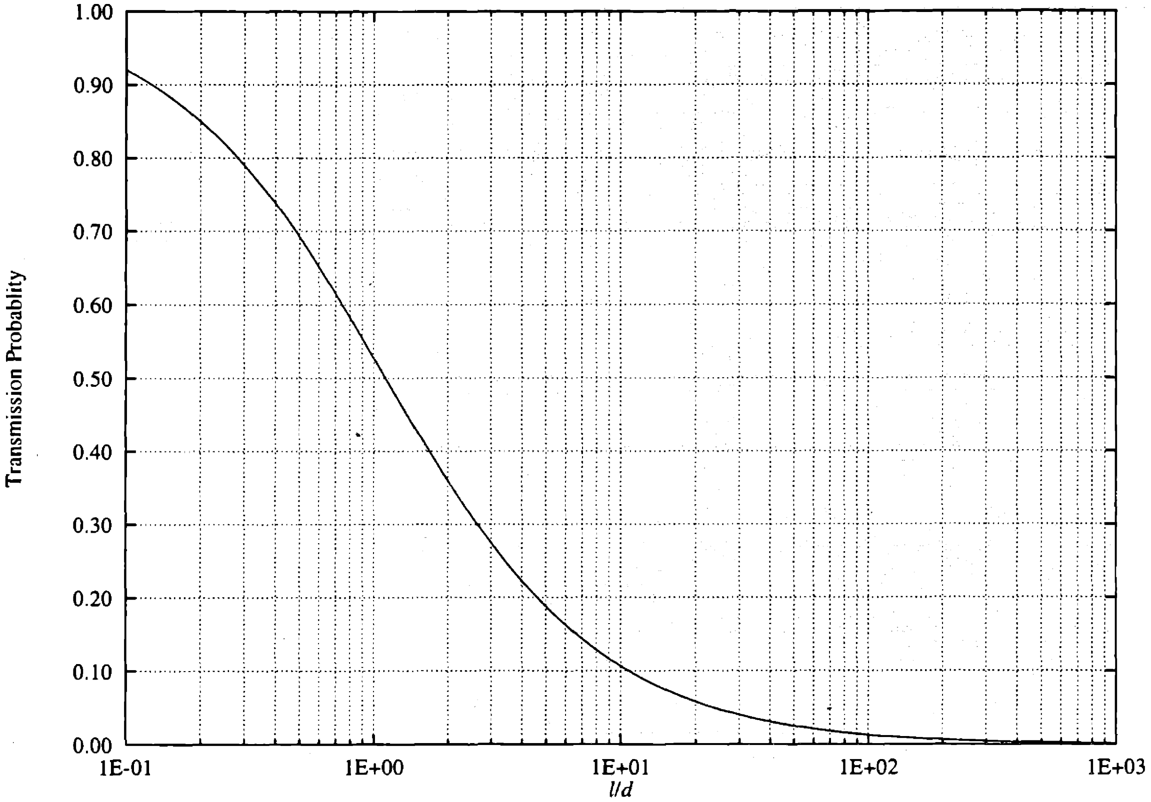

Figure 2-9: The transmission probability $\mathcal{P}$ calculated in Equation 2.19.

where p_u is the pressure upstream of the tube, and p_d is the pressure downstream of the tube. Alternatively, the effective pumping speed of a pump operating in molecular flow is

$$S_K = \frac{S}{1 + \frac{S}{L_K}}. \tag{2.21}$$

Chapter 3

Static Target

The target system described in Section 2.4 consists of a target region separated from the accelerator by four differentially pumped apertures. A vacuum pump is situated between each pair of apertures. A schematic of the target system appears in Figure 3-1. The conductance of the apertures between stages determines the flow rate that

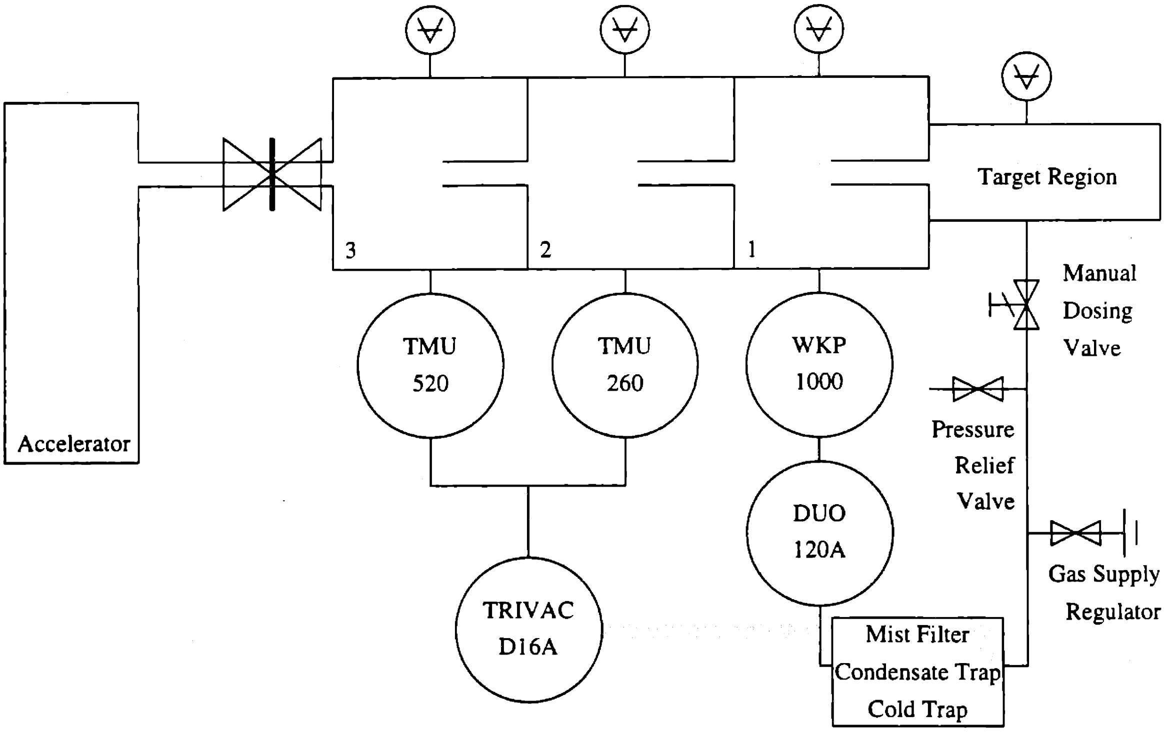

Figure 3-1: Schematic of the gas target system.

takes place through the apertures. For example, the target described in Section 2.4 has a target region with a pressure of 200 mbar that exhausts through an aperture 25 cm long and 0.5 cm in diameter to a pumped chamber at less than 25 mbar; the flow through the aperture is viscous, turbulent, and blocked (as will be shown below). The flow rate into the pumped chamber will be 1.89 bar·liter per second. This flow rate, the flow rate out of the chamber into the next pumped chamber (which can be calculated in much the same way), and the throughput of the first stage's pump determine the pressure that will be maintained in that stage. In this case, a Roots blower capable of pumping speeds on the order of 1000 m^3 per hour at inlet pressures up to 8 mbar will give a pressure of 6.55 mbar in the first pumping stage. All of these calculations assume that the gas flow is constant and steady over time.

3.1 Methodology

Consider a pumped volume with low conductance apertures leading to a higher pressure region and a lower pressure region (see Figure 3-2). In calculating the equilibrium pressure of this volume, we perform a pressure-volume balance. We begin with a given pressure upstream of the volume, and assume certain pressures in the volume and downstream of the volume. We then iterate upon the pressure in that volume until we reach equilibrium. In the flow through some apertures, the pressure difference is great enough that the flow is *blocked*, i.e., the flow velocity reaches the speed of sound, and the gas flux reaches a limiting value. In such a case, the calculation of the pressure upstream of the blocked flow does not depend upon the pressure downstream, provided it is such that blocked flow conditions are maintained.

The following naming conventions will be used throughout the calculations discussed (see Figure 3-2).

- the pressure in pumping stage i is referred to as p_i, e.g., the first pumping stage is at p_1,
- the gas flux leaving a stage by any route is subscripted the same as the pressure

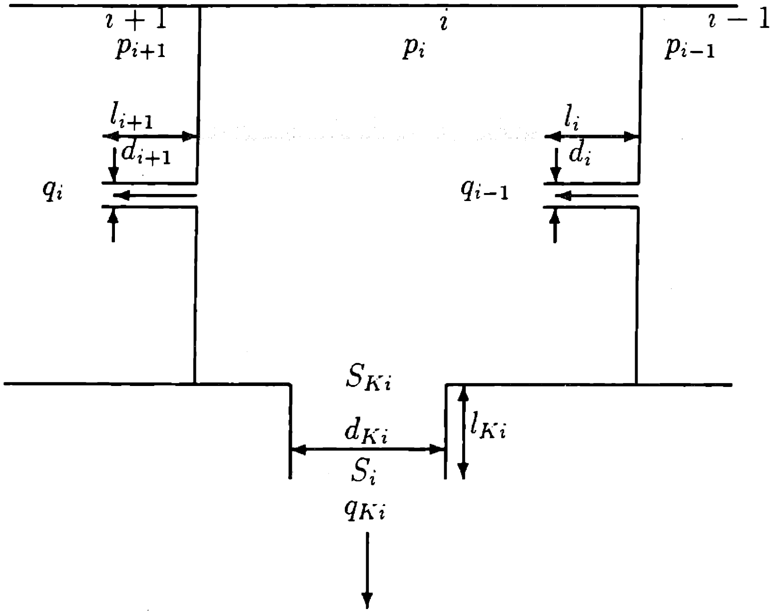

Figure 3-2: Naming conventions for pumping stage pressure calculations ($p_{i+1} < p_i < p_{i-1}$).

in that stage—it is also subscripted with a K if it is an exhaust flow to a pump,

- the dimensions of the exhaust line of a stage are subscripted as the pressure in that stage, and with a K,
- the dimensions of the low-conductance apertures between stages are subscripted as to the stage they are entering, and
- pumping stages will be indexed beginning with the target as $i = 0$.

For cases in which the target is only partially assembled, the "stages" will be named such that the flow conditions at the inlet and exhaust of the stage will match that of the complete target. Thus, a stage described as the first pumping stage will have a turbulent blocked inlet, and a laminar blocked exhaust. A laminar blocked inlet and transition flow exhaust will describe a "second pumping stage," and transition flow inlet with molecular flow exhaust will describe a "third pumping stage."

The following procedure is followed to calculate the pressure in each stage of a differentially pumped system:

1. estimate the pressure p_{i+1} in the stage,
2. calculate the gas flux q_i from the upstream stage (i) to the present stage ($i+1$) as a function of the (given) upstream pressure p_i and the estimated pressure p_{i+1},
3. calculate the gas flux q_{i+1} from the present stage ($i+1$) to the downstream stage ($i+2$), using the estimated pressure p_{i+1} and, if necessary, an estimated pressure p_{i+2},
4. calculate the gas flux $q_{K(i+1)}$ through the exhaust of the present stage given the pressure p_{i+1},
5. perform a mass balance

$$\Delta p_{i+1} = q_i - q_{i+1} - q_{K(i+1)}, \tag{3.1}$$

6. and iterate on p_{i+1} until $\Delta p_{i+1} = 0$.

3.2 Initial Design

The initial design for the gas target appears in Section 2.4, with all apertures having a diameter of 0.5 cm, the first aperture having a length of 25 cm, and the remaining apertures having a length of 10 cm. The pressure in the target region is 200 mbar, and the pressure in the first pumped region is such that the flow through the first aperture is viscous, turbulent, and blocked. Pressures across this target system appear in Table 3.1, repeated from Table 2.3.

To maintain blocked flow through the first aperture, the pressure in the first pumping stage (p_1) must be less than the critical pressure p_0^*. To determine whether the flow is turbulent or laminar examine Equation 2.9, which indicates (for laminar flow) critical pressures $p^* > p$ for

$$p > 0.43 \cdot \frac{l}{d^2}. \tag{3.2}$$

Stage	Pressure (mbar)	Pump Type	Inlet Pressure	Capacity (at pressure)	Entrance		Pump	
					l	d	l_K	d_K
Target	2.00×10^2	—	—	—	—	—	—	—
1	6.55×10^0	Roots	6.55×10^0	278 l/sec	25	0.5	10	16
2	1.68×10^{-1}	Turbo	1.68×10^{-1}	250 l/sec	10	0.5	10	10
3	1.90×10^{-4}	Turbo	1.34×10^{-4}	560 l/sec	10	0.5	10	10

Table 3.1: Characteristics of the gas target system. Dimensions are in centimeters.

This can be used as a rough guide to determine whether blocked viscous flow through an aperture is laminar or turbulent—if the upstream pressure $p \gg 0.43 \cdot \frac{l}{d^2}$, the flow is turbulent, while if $p \ll 0.43 \cdot \frac{l}{d^2}$ the flow is laminar. The assumption of laminar or turbulent conditions will be verified after the calculations are performed. In this case, $0.43 \cdot \frac{l}{d^2} = 43$ mbar, so the flow through the first aperture is assumed to be turbulent.

Referring to Equations 2.7 and 2.8 for turbulent blocked flow, the critical pressure for the first stage, p_0^*, is given by

$$\frac{p_0^*}{p_0} = \frac{4.51 \cdot \left(\frac{d_1^3 p_0^2}{2l_1}\right)^{4/7}}{d_1 \cdot p_0}, \tag{3.3}$$

and the critical flux by

$$q_0^* = 360 \cdot d_1 \cdot \left(\frac{d_1^3 \left(p_0^2 - p_0^{*2}\right)}{2l_1}\right)^{4/7}. \tag{3.4}$$

The critical pressure is then calculated to be 125 mbar, while the critical flux is 1.89 mbar·ℓ/s.

For the differential pumping system to be at all effective, the bulk of the flow exiting the first pumping stage must exit through the pump, rather than through the second aperture. If we assume that the entire flow of 1.89 mbar·ℓ/s goes through the pump, the resulting pump inlet pressure would be

$$p_{K1} = \frac{q_{K1}}{S_1}, \tag{3.5}$$

which is 6.8 mbar. This pressure can be multiplied by the diameter of the second aperture (0.5 cm), and by the diameter of the exhaust port (16 cm), to obtain 3.4 and 109 mbar·cm, respectively. This is much greater than the 0.6 mbar·cm required for this product for viscous flow conditions to be maintained. From Equation 2.14, the flow rate further implies $Re < 200$ through the exhaust, indicating laminar flow. If we assume that no more than 1% of the flow went through the second aperture, Equation 2.14 gives $Re < 32$, indicating laminar flow through the second aperture as well.

From Equations 2.9 and 2.10 for laminar viscous flow, we have

$$\frac{p_1^*}{p_1} = 2.3 \cdot \frac{d_2^2}{l_2} \cdot p_1, \tag{3.6}$$

for the critical pressure for the flow through the second aperture, and

$$q_1^* = 363 \cdot d_2 \cdot \frac{d_2^3}{l_2} \frac{p_1^2 - p_1^{*2}}{2}, \tag{3.7}$$

for the critical flow through that aperture.

The flow through the exhaust of the first stage is given by

$$q_{K1} = p_1 \cdot S_{K1}, \tag{3.8}$$

where S_{K1} is the effective pumping speed, given by

$$S_{K1} = \frac{S_1}{\sqrt{1 + x_1}}, \tag{3.9}$$

and

$$x_1 = \frac{2 \cdot 128 \cdot \eta l_{K1} S_1}{\pi d_{K1}^4 \cdot p_{K1}}. \tag{3.10}$$

The flow through the first aperture q_0^* does not depend upon the pressure p_1, provided that $p_1 < p_0^*$. We can estimate the value p_{K1} as something less than the critical pressure p_0^*, as given by Equation 3.3. We then calculate S_{K1} using Equations 3.9

and 3.10. We can then calculate p_1 as

$$p_1 = p_{K1} \cdot \frac{S_1}{S_{K1}}, \tag{3.11}$$

which allows us to calculate p_1^* and q_1^* from Equations 3.6 and 3.7, respectively. The value of q_1^*, of course, does not depend upon p_2, provided that $p_2 < p_1^*$. The balance condition is then

$$\Delta p_1 = q_0^* - q_1^* - q_{K1}. \tag{3.12}$$

We then iterate on p_{K1} until $\Delta p_1 = 0$. Iteration on p_{K1} is not required if $p_{K1} \approx p_1$, and $q_1^* \ll q_0^*$. However, if the conductance of the exhaust line is dependent upon the chamber pressure, as is the case in Equation 3.10, and significant in magnitude, then iteration is necessary.

If we perform such calculations for the first pumped stage of the target system for a range of target pressures and a variety of inlet apertures, we obtain the data shown in Figure 3-3. The actual pressure reached in the first stage at the end of the iteration process is 6.55 mbar, and the flow rate through the second aperture is 41.8 mbar·ℓ/sec. The flow rate through the Roots blower is 1.85 bar·ℓ/sec.

Upon reaching a solution for p_1, the assumptions that went into its calculation must be verified. First, viscous flow is indicated by the product of pressure in a tube and the diameter of the tube being greater than 0.6 mbar·cm. For the flow through the first aperture, we could estimate a lower limit for this value by using the actual pressure in the first stage and the diameter of the first aperture, $p_1 \cdot d_1$. However, this would be overly conservative, in that the pressure in the aperture itself (a long, thin tube) clearly never reaches p_1. A less conservative estimate might be the critical pressure p_0^*. Rearranging Equation 3.3, we see that this condition is satisfied for

$$p_0 > 0.2421\sqrt{\frac{l_1}{d_1^3}}. \tag{3.13}$$

Turbulent flow is, of course, indicated by a Reynolds number $Re > 4000$. For the flow through the first aperture, with deuterium at room temperature, we have from

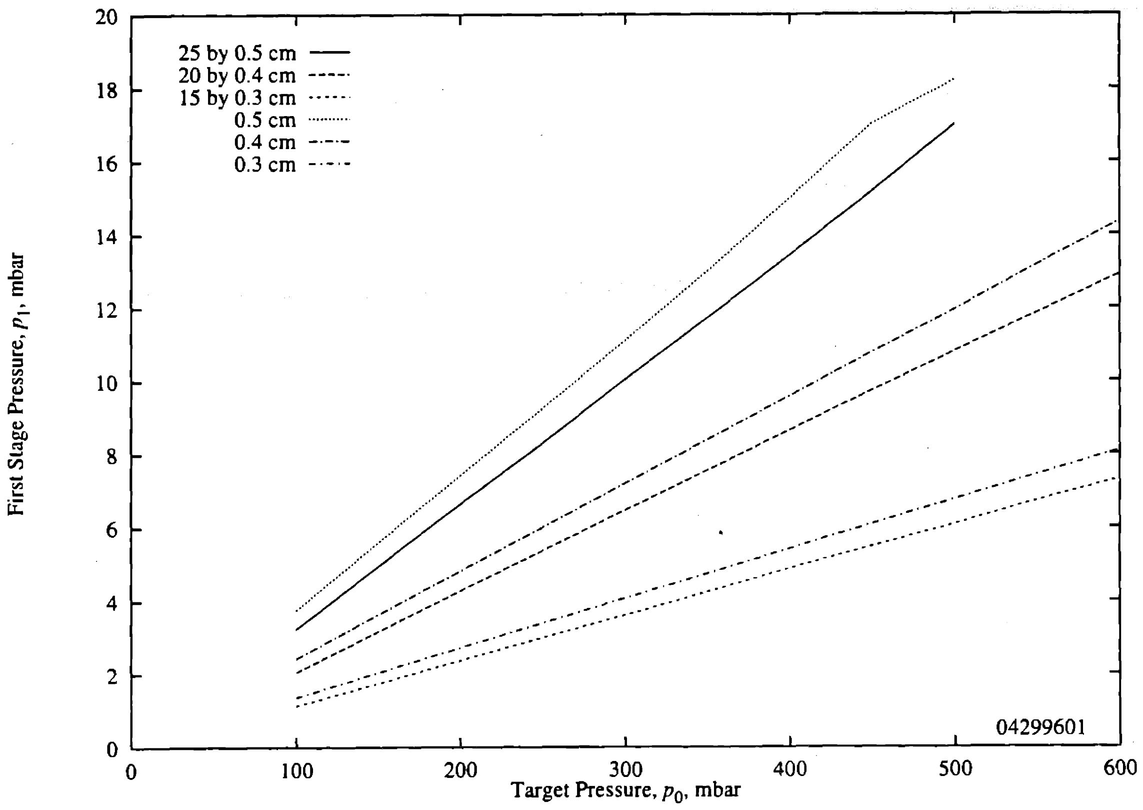

Figure 3-3: Equilibrium first stage pressure for various target pressures and various inlet apertures. The lower pressure aperture is 10 cm long and 0.5 cm in diameter.

Equation 2.14

$$Re_0 = 1.67 \cdot \frac{q_0^*}{d_1}, \tag{3.14}$$

where q is in mbar·liter per second, and d is in centimeters. Substituting in from Equations 3.4 and 3.14, we have

$$p_0 > \sqrt{54.9\frac{l_1}{d_1^3} + \frac{0.36}{d_1^2}}. \tag{3.15}$$

Equation 3.13 is satisfied only in regions in which Equation 3.15 is also satisfied.

The viscous flow criterion for the flow through the second aperture requires that $p_1^* \cdot d_2 > 0.6$ mbar·cm. Rearranging Equation 3.6, we see that this implies

$$p_1 > 0.5108\sqrt{\frac{l_2}{d_2^3}}. \tag{3.16}$$

The Reynolds number

$$Re_1 = 1.67 \cdot \frac{q_1^*}{d_2}, \tag{3.17}$$

for the flow through the second aperture must be less than 2300 for the flow to be considered laminar. This implies that

$$p_1 < \sqrt{\frac{7.5777 \cdot l_2/d_2^3}{1 - 2.3 \cdot d_2^2/l_2}}. \tag{3.18}$$

The exhaust flow from the first stage is also laminar and viscous. Laminar flow requires that $q_{K1} < 2300$; thus

$$p_{K1} < \frac{2300}{S_1}. \tag{3.19}$$

The viscous flow criterion requires that $p_{K1} \cdot d_{K1} > 0.6$ mbar·cm, which means

$$p_{K1} > \frac{0.6}{d_{K1}}. \tag{3.20}$$

Finally, the assumption that the flow through the first aperture is blocked requires

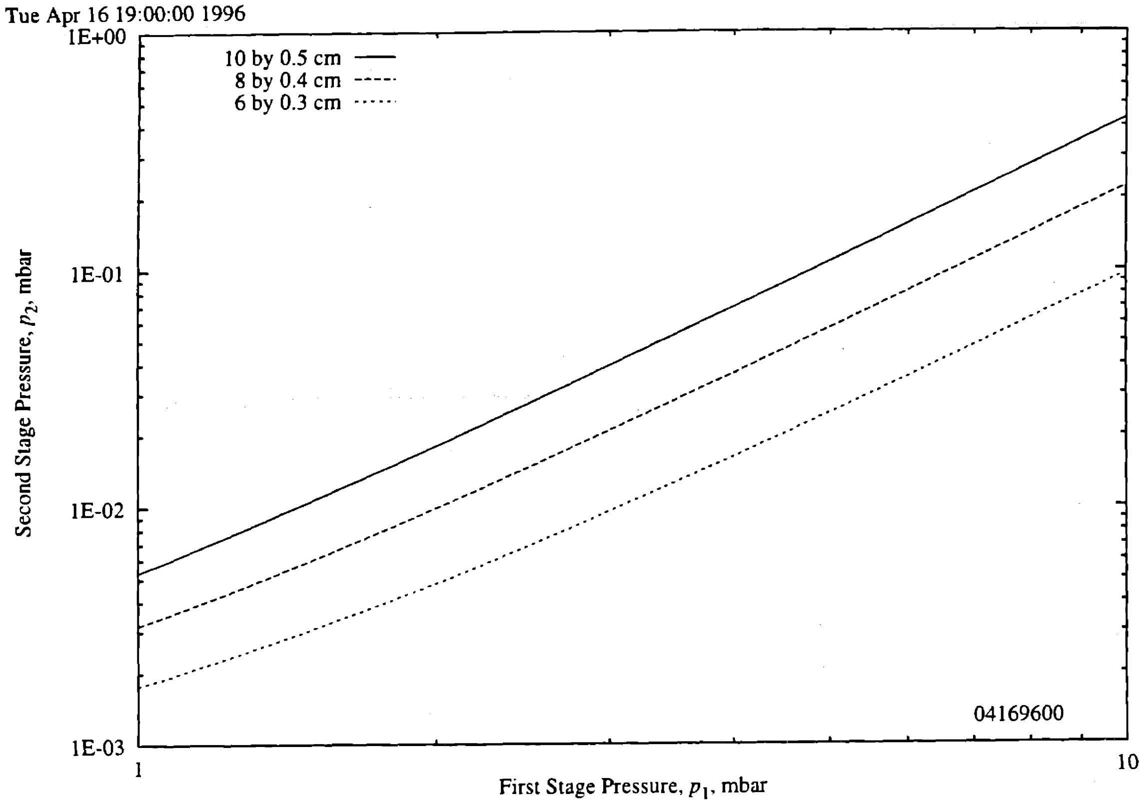

Figure 3-4: Pressure in the second stage as a function of that in the first stage.

that

$$p_1 < \frac{4.51 \cdot \left(\frac{d_1^3 p_0^2}{2 l_1}\right)^{4/7}}{d_1}, \tag{3.21}$$

while critical flow through the second aperture requires

$$p_2 < 2.3 \cdot \frac{d_2^2}{l_2} \cdot p_1^2. \tag{3.22}$$

If we repeat our iterative mass balance for the second stage of the system, using

$$\Delta p_2 = q_1^* - q_2 - q_{K2}, \tag{3.23}$$

we find that the second stage pressure p_2 depends upon p_1 as shown in Figure 3-4.

The flow through the second aperture (q_1^*) is given by Equation 3.7. The third stage is in the Knudsen flow regime, so the flow through the third aperture (q_2) is

$$q_2 = \frac{\pi}{128} \cdot \frac{d_3^4}{\eta l_3} \cdot \frac{(p_2 - p_3)^2}{2} + \frac{1}{6} \cdot \sqrt{\frac{2\pi RT}{M}} \cdot \frac{d_3^3}{l_3} \cdot \frac{1 + \sqrt{\frac{M}{RT}} \cdot \frac{d_3}{\eta} \cdot \frac{p_2+p_3}{2}}{1 + 1.24 \cdot \sqrt{\frac{M}{RT}} \cdot \frac{d_3}{\eta} \cdot \frac{p_2+p_3}{2}} \cdot (p_2 - p_3), \quad (3.24)$$

from Equation 2.15.

If we substitute the values for deuterium at room temperature, we get

$$q_2 = 98 \cdot \frac{d_3^4}{l_3} \cdot (p_2 - p_3)^2 + 32.6 \cdot \frac{d_3^3}{l_3} \cdot \frac{1 + 51.5 \cdot d_3 \cdot (p_2 + p_3)}{1 + 63.5 \cdot d_3 \cdot (p_2 + p_3)} \cdot (p_2 - p_3). \quad (3.25)$$

The flow from the exhaust of the second stage is again laminar and viscous, and given by

$$q_{K2} = p_2 \cdot S_{K2}, \quad (3.26)$$

where

$$S_{K2} = \frac{S_2}{\sqrt{1 + x_2}}, \quad (3.27)$$

and

$$x_2 = \frac{2 \cdot 128 \cdot \eta l_{K2} S_2}{\pi d_{K2}^4 \cdot p_{K2}}. \quad (3.28)$$

The flow through the second aperture was shown above to be viscous and laminar. The flow through the third aperture was assumed to be Knudsen flow. This is the case if $p_2 \cdot d_3$ lies between 0.01 and 0.6 mbar·cm;

$$\frac{0.01}{d_3} < p_2 < \frac{0.6}{d_3}. \quad (3.29)$$

The viscous flow criterion for the exhaust of the second stage requires

$$p_{K2} > \frac{0.6}{d_{K2}}. \quad (3.30)$$

The laminar condition requires that

$$p_{K2} < \frac{2300}{S_2}. \quad (3.31)$$

For the third stage pressure, we have

$$\Delta p_3 = q_2 - q_3 - q_{K3}. \tag{3.32}$$

For the flow through the fourth aperture (into the accelerator), Equation 2.16 gives

$$L_4 = \sqrt{\frac{M_{air}}{M_{deuterium}}} \cdot L_{e4} \cdot \left(1 + \frac{3}{4}\frac{l_4}{d_4}\right)^{-1} \xi_4^{-1}, \tag{3.33}$$

where the constant factor is to account for the difference between air and deuterium.

For the the exhaust line to the third stage, the conductance can be calculated, again from Equation 2.16, as

$$L_{K3} = \sqrt{\frac{M_{air}}{M_{deuterium}}} \cdot L_{eK3} \cdot \left(1 + \frac{3}{4}\frac{l_{K3}}{d_{K3}}\right)^{-1} \xi_{K3}^{-1}. \tag{3.34}$$

We can now calculate the flow rate through the fourth aperture (into the accelerator) as

$$q_3 = L_4(p_3 - p_4), \tag{3.35}$$

where the pressure p_4 is that at which the accelerator should be maintained. The effective speed of the pump on the third stage is

$$S_{K3} = \frac{S_3}{1 + \frac{S_3}{L_{K3}}}. \tag{3.36}$$

If we then estimate the pressure in the third stage, p_3, then the flow rate through the exhaust of the third stage is

$$q_{K3} = p_3 S_{K3}. \tag{3.37}$$

We then use Equation 3.32 to perform a mass balance on the third stage, and iterate p_3 until $\Delta p_3 = 0$.

If we perform this procedure, using a desired value of $p_4 = 1.33 \times 10^{-6}$ mbar, we arrive at the relationship shown in Figure 3-5. The only assumption made during this procedure is that we are in the molecular flow regime. This requires that $p \cdot d <$

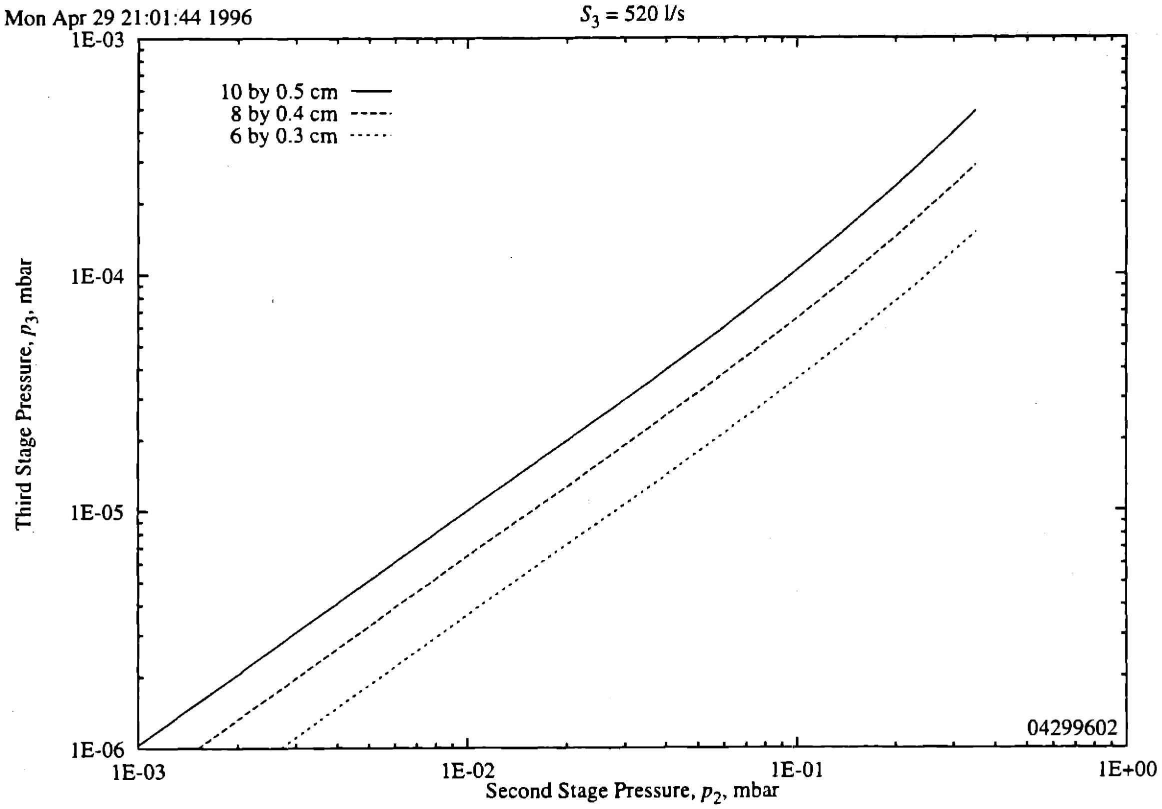

Figure 3-5: Third stage pressure as a function of second stage pressure.

0.01 mbar·cm. For the exhaust line we have

$$p_{K3} < \frac{0.01}{d_{K3}}, \tag{3.38}$$

and for the fourth aperture

$$p_3 < \frac{0.01}{d_4}. \tag{3.39}$$

If we collect all the various bounding values, they can be more easily compared.

$$\begin{array}{rcccl}
\sqrt{54.9\frac{l_1}{d_1^3} + \frac{0.36}{d_1^2}} & < & p_0 & & \\
0.5108\sqrt{\frac{l_2}{d_2^3}} & < & p_1 & < & \sqrt{\frac{7.5777 \cdot l_2/d_2^3}{1 - 2.3 \cdot d_2^2/l_2}} \\
 & & p_1 & < & \frac{4.51 \cdot \left(\frac{d_1^3 p_0^2}{2l_1}\right)^{4/7}}{d_1} \\
\frac{0.6}{d_{K1}} & < & p_{K1} & < & \frac{2300}{S_1} \\
\frac{0.01}{d_3} & < & p_2 & < & \frac{0.6}{d_3} \\
 & & p_2 & < & 2.3 \cdot \frac{d_2^2}{l_2} \cdot p_1^2 \\
\frac{0.6}{d_{K2}} & < & p_{K2} & < & \frac{2300}{S_2} \\
 & & p_{K3} & < & \frac{0.01}{d_{K3}} \\
 & & p_3 & < & \frac{0.01}{d_4}
\end{array} \tag{3.40}$$

The limits in Equations 3.40 can be summarized as

$$\begin{array}{rcccl}
105 & < & p_0 & & \\
4.57 & < & p_1 & < & 25.4 \\
 & & p_1 & < & 125 \\
0.06 & < & p_{K1} & < & 8.27 \\
0.02 & < & p_2 & < & 1.20
\end{array} \tag{3.41}$$

$$\begin{aligned} p_2 &< 2.47 \\ 0.06 < p_{K2} &< 9.20 \\ p_{K3} &< 1 \times 10^{-3} \\ p_3 &< 2 \times 10^{-3}. \end{aligned}$$

All of the values in Table 3.1 are within these limits.

A final check for consistency requires that the pumps chosen for each of the three stages are capable of the calculated throughput at the calculated inlet pressure.

3.3 Measurements

A testbed was assembled to measure the pressure drops obtainable across various apertures in those pressure ranges expected to occur in the gas target system. The equipment used in the testbed is as follows: The turbopumps are a Balzers model TMU 260 and a Balzers model TMU 520. The TMU 260 is rated at a speed of 210 ℓ/s for nitrogen, and 220 ℓ/s for helium. The rated compression ratio of this turbopump is $> 10^9$ for nitrogen, and 3×10^5 for helium. The TMU 520 is rated at a speed of 500 ℓ/s for both nitrogen and helium. The rated compression ratio is $> 10^{12}$ for nitrogen, and 5×10^7 for helium. In both turbopumps, the rated speed begins to fall off sharply at inlet pressures of approximately 0.01 mbar. The Roots blower is a Balzers WKP 1000, as part of a WOD 900 B pumping unit, which includes a DUO 120 A two stage rotary vane backing pump. This system is rated at 900 m^3/hr.

Pressures are measured using two Balzers TPR 010 Pirani gauges, which can measure air/nitrogen pressures from 8×10^{-4} mbar to 10^3 mbar, and two Balzers IKR 050 Cold Cathode gauges, which can measure from 2×10^{-9} mbar to 5×10^{-3} mbar. The Pirani and cold cathode gauges are calibrated for nitrogen, with conversion factors for other gasses provided by the manufacturer. These Pirani gauges are incapable of measuring pressures higher than approximately 10 mbar in helium, given their present calibration. For pressures above this value, a Wallace & Tiernan FA 223 Bourdon absolute pressure gauge and a Varian DV100 capacitance manometer were used.

A controlled gas flow is provided by a Balzers EVN 116 manual dosing valve. This valve will admit a controlled flow rate ranging from 5×10^{-6} mbar·ℓ/s to 10^3 mbar·ℓ/s for air. The flow rate for a given digital setting of the valve is not particularly reproducible—one should consider the pressures attained and the pressure differential as being more indicative of the flow rate than the digital setting itself.

3.3.1 Blocked Turbulent Flow

Figure 3-6 shows the pressure difference supported across an aperture 10 cm long and 0.5 cm in diameter, compared to calculated values for various apertures. These calculations indicated that the flow should be considered turbulent and blocked. The calculations (here and below) were performed for deuterium. The measurements were made with helium. Were the calculations to be done for helium, the results would change by less than 1%.

The pump used for the experiments was a Balzers WOD 900 B Roots pumping unit. The calculations were performed for $S_1 = 1000$ m^3/hr. The calculations appear to have been reasonably accurate. The measurements were taken over a range in p_1 that encompassed the largest pressure the Pirani gauges were capable are capable of measuring, given their calibration. A linear fit to the data gave a target pressure of 190 mbar for a first stage pressure of 6.5 mbar.

3.3.2 Blocked Laminar Flow

Figure 3-7 shows the pressure difference measured across various apertures for conditions calculated to exist for blocked laminar flow. The data show that the original calculations were somewhat inaccurate. Fortunately, they also appear to have underestimated the pressure drop supported across that aperture. It is possible that the flow through this aperture is not, as was predicted, viscous, laminar, and blocked. It is also possible that the tubes in question do not meet the criteria for being considered "long." In any event, while the source of the differences is not immediately clear, the measurements do indicate that, whatever the reason, the predicted pressure ratios

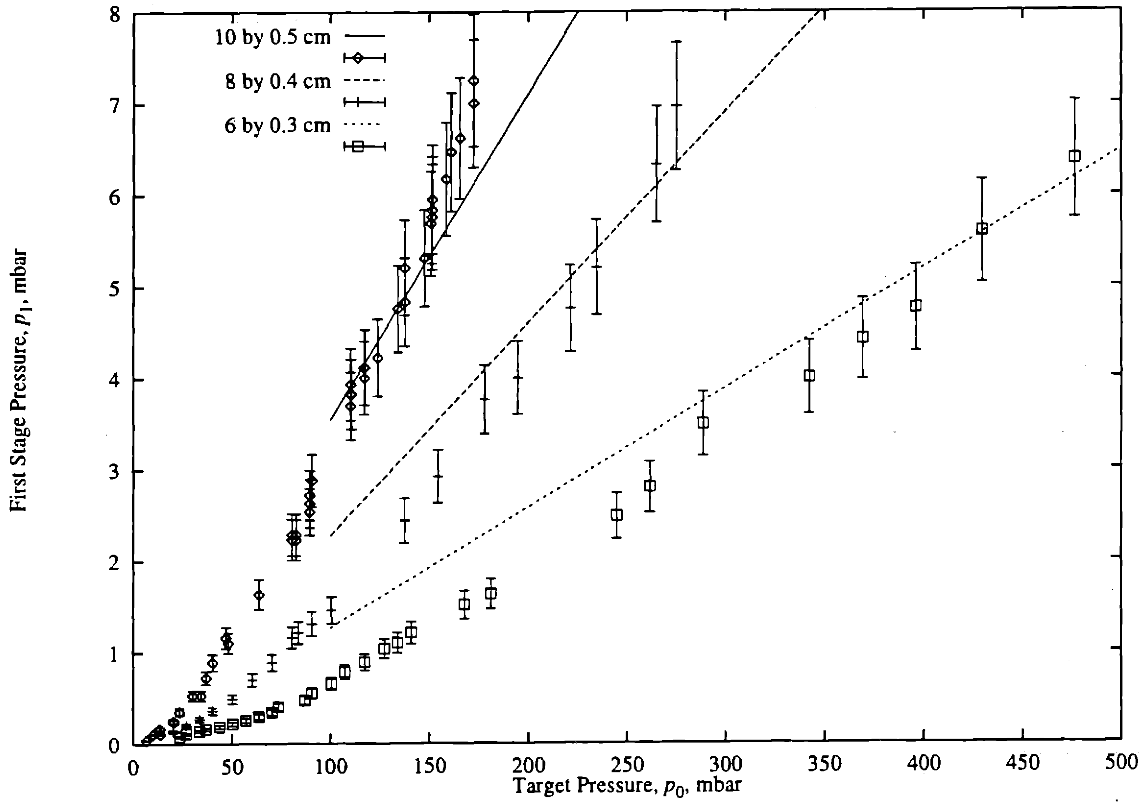

Figure 3-6: Comparison of measurements and calculations for the first pumping stage. The points are measurements across a 10 cm long by 0.5 cm diameter aperture, with a WOD 900 B Roots pumping unit. The lines are calculations for various apertures with a pumping speed of 1000 m^3/hr.

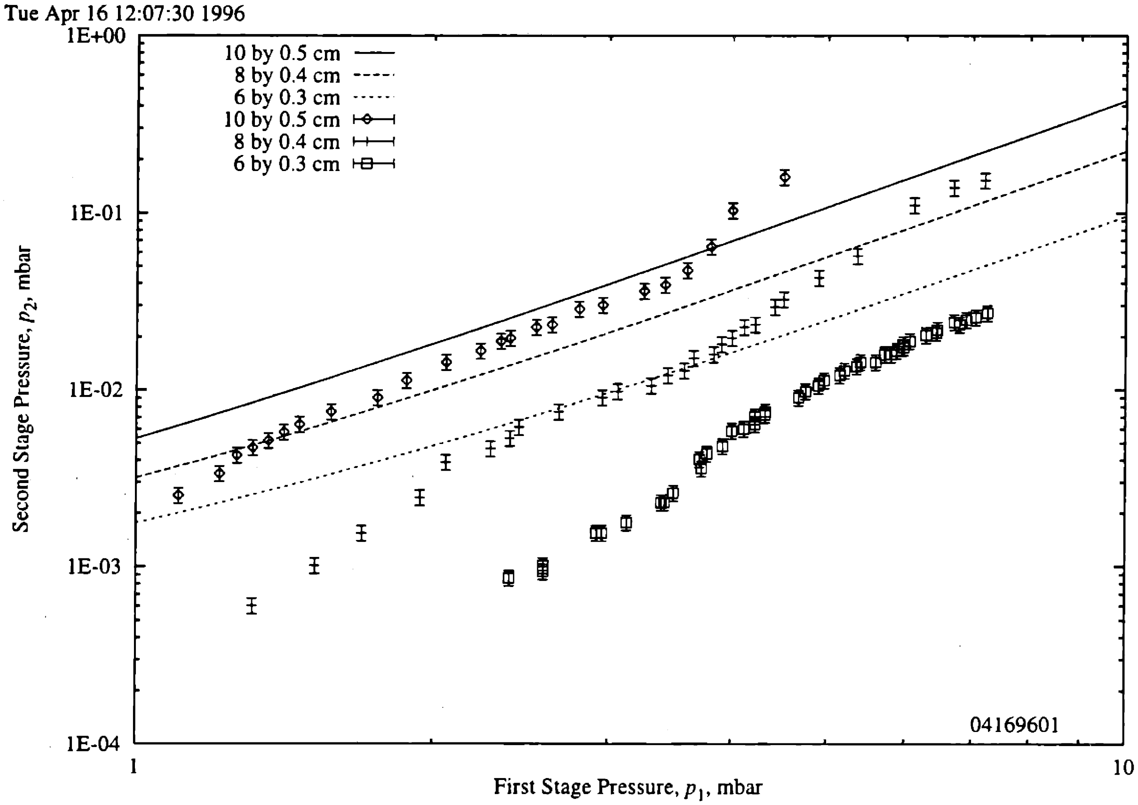

Figure 3-7: Comparison of calculated (helium) pressure difference across the second aperture to the measured pressure difference. The calculations were done for a pumping speed of 250 ℓ/s, and the measurements were taken using a TMU 260.

can not only be obtained, but can be bettered.

In making these measurements, it was apparent that the turbopumps have difficulty operating at approximately 0.05 mbar inlet pressure and greater. In the case of the TMU 260, this resulted in a sharp increase in pressure at the pump inlet for a small increase in the upstream pressure. At a pressure of about 0.067 mbar, the pump began to lose speed, and the pressure steadily increased. At 0.04 mbar, the pump was able to maintain speed, but was obviously under some strain, as evidenced by a slowdown in rotation speed, 1007 Hz as compared to 1009 Hz for operation below 1×10^{-6} mbar and an increase in current required by the motor, from 1.0 A below 1×10^{-6} mbar to 3.9 A. At startup from atmosphere, the motor draws 4 A.

The constriction factor, mentioned in Section 2.5.1, may explain the apparent inaccuracy in the predictions. If we use the downstream pressure p_2 to calculate the incoming gas flux q_1, we obtain the data shown in Figure 3-8. The data in Figure 3-7

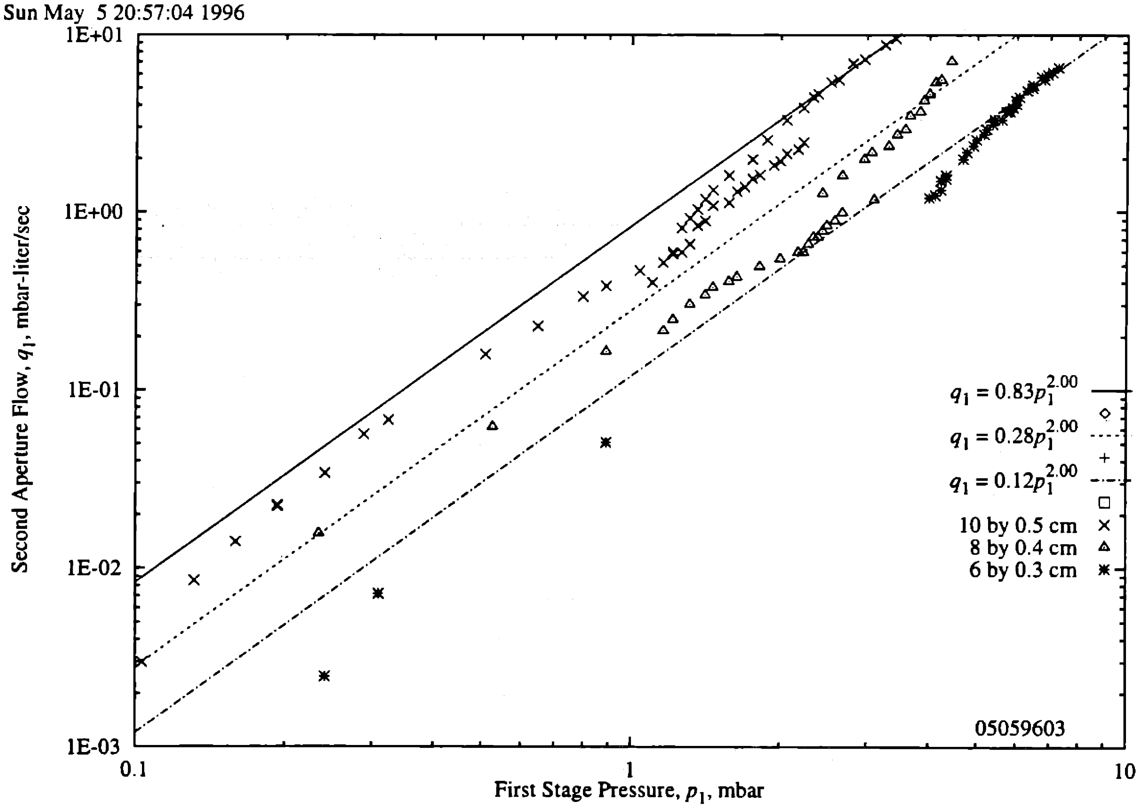

Figure 3-8: Inferred flow rate through second aperture.

Aperture (cm)	Calculation		Fit	α	
	Long Tube	Eq 3.43	(mbar·ℓ/s)	Long Tube	Eq 3.43
10 by 0.5	1.07	0.81	0.83 ± 0.04	0.77	1.02
8 by 0.4	0.56	0.44	0.28 ± 0.02	0.50	0.64
6 by 0.3	0.24	0.20	0.12 ± 0.01	0.51	0.60

Table 3.2: Evaluation of constriction factor α for second aperture flow rate data. Fitted coefficient dimensions are in liters per second per mbar, α is dimensionless.

in the regime in which the turbopump had difficulty operating were rejected, as the resulting reduction in pumping speed prevents the throughput from being accurately inferred. The lines shown in Figure 3-8 are the result of regression fits done to the data, in which the power to which the pressure was raised was fixed at two (Equation 2.10 clearly shows that the flow rate is directly proportional to the square of the driving pressure). The fit is, of course, more strongly weighted by the higher flow rate data, as evidenced in the graph. The fitted coefficients of the curves appear in Table 3.2.

If the apertures are not accurately representable as long tubes, the nozzle and tube flow equations from Section 2.5.1 can be combined. This results in the numbers agreeing somewhat better, but not by a tremendous amount. If the conductance C of an aperture is defined in the standard fashion,

$$C = \frac{q}{p_u - p_d}, \tag{3.42}$$

where q is the gas flow rate and p_u and p_d are the upstream and downstream pressures, respectively, then $C \approx q/p_u$, as $p_u \gg p_d$. Then

$$\frac{1}{q} = \frac{1}{q_{nozzle}} + \frac{1}{q_{tube}}. \tag{3.43}$$

The comparison between this prediction and measurements is shown in Figure 3-9, which is analogous to Figure 3-7. For the combined data expressed as flow rates, the comparison becomes as shown in Figure 3-10.

If we go yet further, and perform the calculations for q_1 as a function of pressure

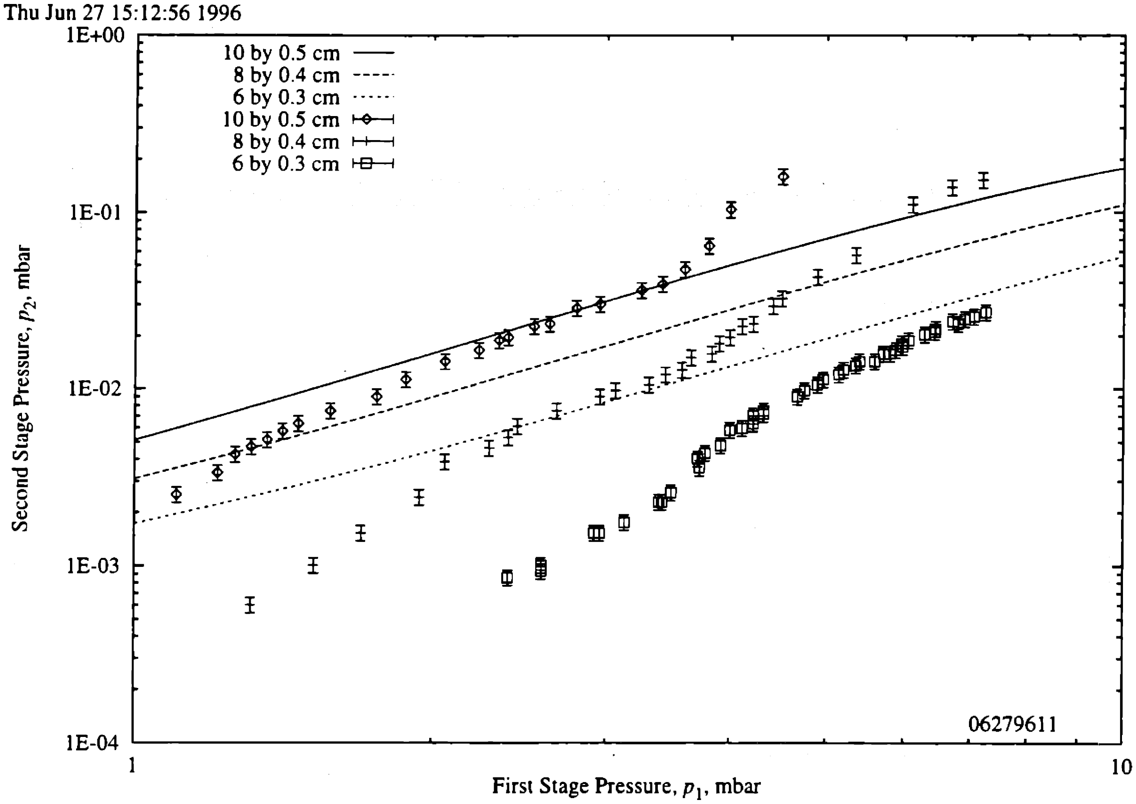

Figure 3-9: Comparison of pressure difference across the second aperture calculated using Equation 3.43 to the measured pressure difference.

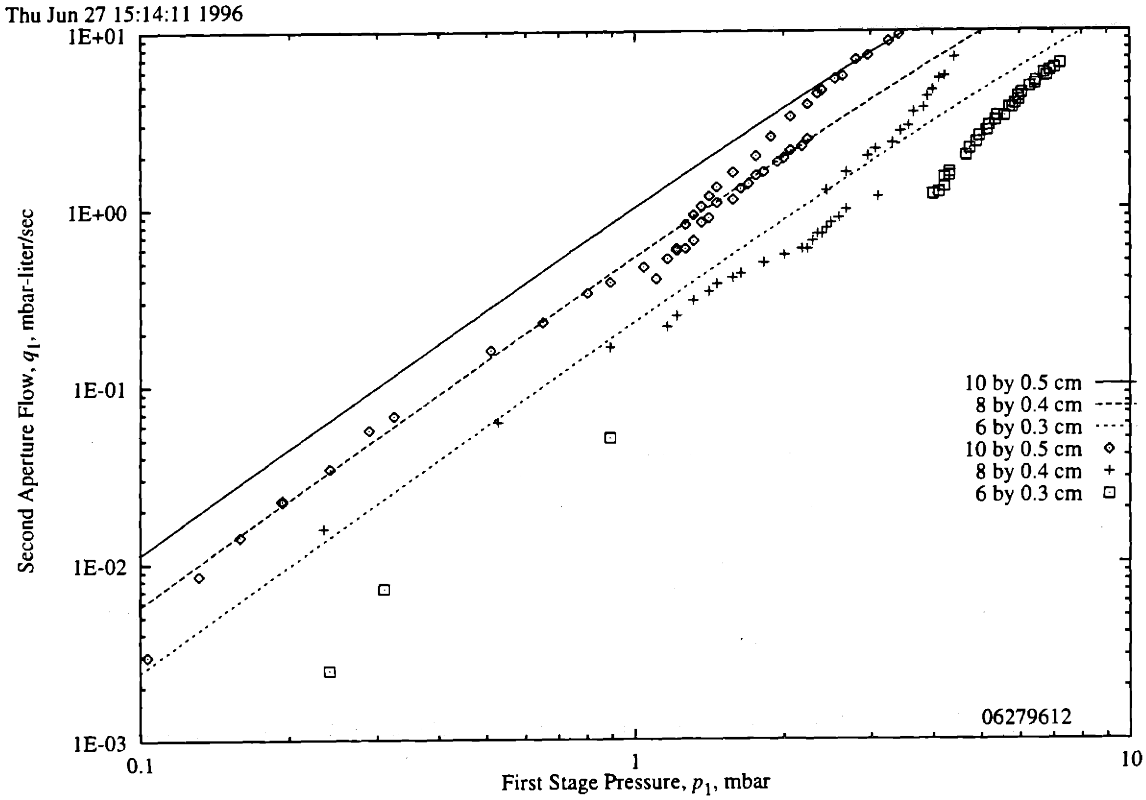

Figure 3-10: Comparison of the flow rates calculated using Equation 3.43 with the flow rates inferred from measured data, both across the second aperture.

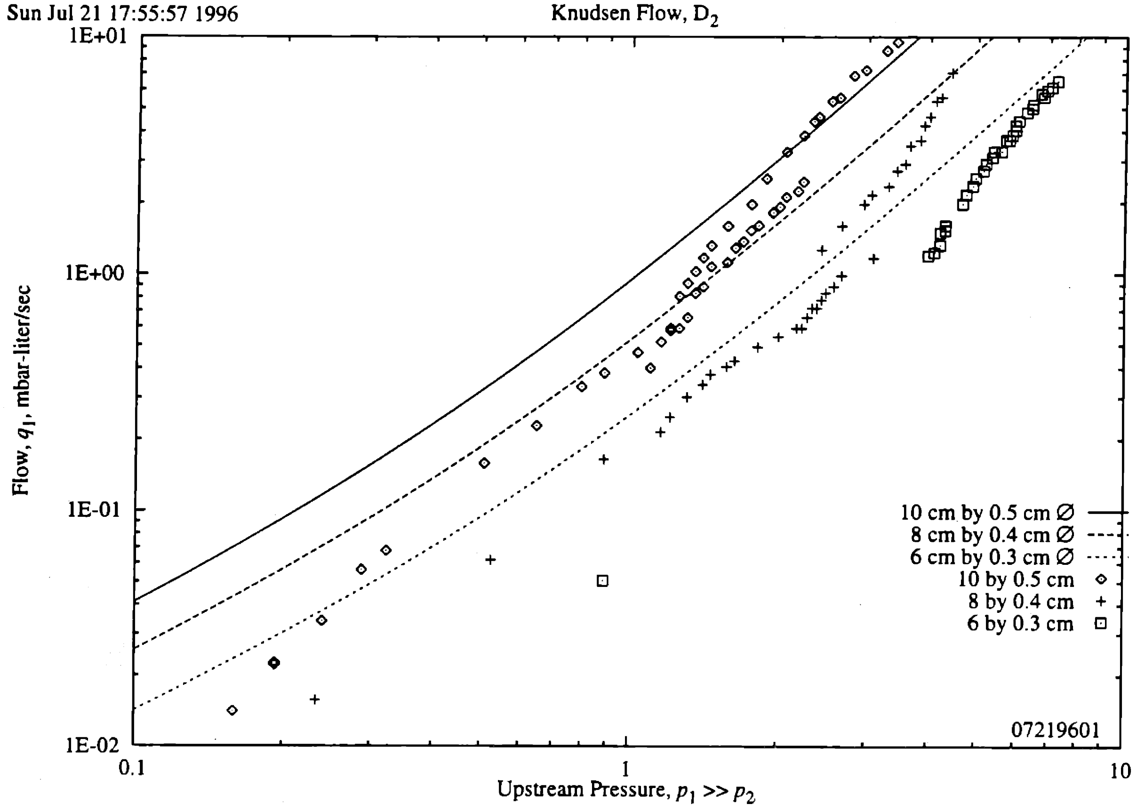

Figure 3-11: Comparison between flow rates measured across the second aperture and flow rates predicted for Knudsen flow through long tubes.

p_1 using Equation 3.25, we obtain the data shown in Figure 3-11. To perform this calculation, we must assume that the downstream pressure p_2 is negligible as compared to p_1. We can see that the Knudsen flow equations clearly do not describe the data more accurately than the calculations based upon blocked laminar flow.

3.3.3 Transition Flow

Figure 3-12 compares the measured pressure difference supported across various apertures by the TMU 520 with the calculated values for a 560 ℓ/s pump. The calculation appears to have been fairly accurate, with the increasing differences at lower pressures due to the fact that the inserted gas flow (which comes solely into the upstream chamber) becomes similar to that virtual flow outgassing from the walls of the system (which comes from both chambers). This flow would be reduced by increasing the

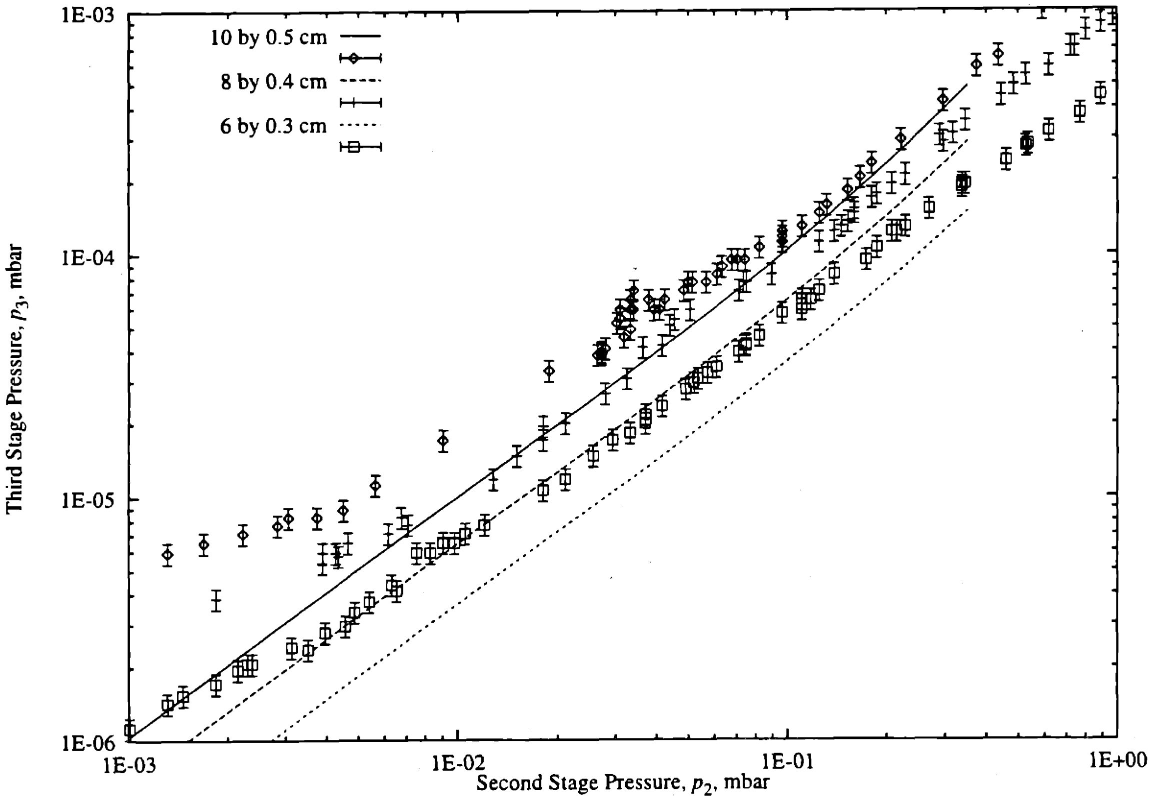

Figure 3-12: Comparison of calculated (helium) pressure difference for a 520 ℓ/s pump across the third aperture to the measured pressure difference for a TMU 520.

time for which the system was baked and pumped out before use. A smaller pressure drop (leading to a higher p_3 is observed upon the initial operation of the testbed than in subsequent instances. Operation of the testbed, at least with helium, appears to "sweep" the system clean of other gasses which do not desorb as quickly as does the helium that replaces them.

3.4 Revised Design

For a revised design, consider a target system appearing in Table 3.3. These pressures are based upon the measurements performed with the testbed described previously. The primary differences between the initial design and the revised design are that the predicted pressure drops are based upon measurement rather than calculation, and the pressure in the second stage is reduced to a level at which the turbopump on that stage would be able to function.

Stage	Pressure (mbar)	Pump Type	Capacity (at pressure)	Entrance l	Entrance d	Pump l_K	Pump d_K
Target	1.0×10^2	—	—	—	—	—	—
1	3.0×10^0	Roots	278 l/sec	10	0.5	10	10
2	3.0×10^{-2}	Turbo	250 l/sec	10	0.5	10	10
3	2.0×10^{-5}	Turbo	560 l/sec	10	0.5	10	10

Table 3.3: Characteristics of a sample gas target system. Dimensions are in centimeters.

The limits from Equations 3.40 are

$$\begin{aligned}
66.3 < \; & p_0 & \\
4.57 < \; & p_1 & < 25.4 \\
& p_1 & < 95.6 \\
0.06 < \; & p_{K1} & < 9.20 \\
0.02 < \; & p_2 & < 1.20 \\
& p_2 & < 0.518
\end{aligned} \tag{3.44}$$

$$\begin{aligned} 0.06 < \; & p_{K2} && < 9.20 \\ & p_{K3} && < 1 \times 10^{-3} \\ & p_3 && < 2 \times 10^{-3}. \end{aligned}$$

The minimum value criterion for p_1 is not met for this design. This indicates that the flow through the second aperture may not be viscous. This criterion, referring to Equation 3.13, is conservative, as the pressure in the aperture itself should never be as low as p_1^*. Nonetheless, the flow through the second aperture may not be well described by the equations set forth. This corresponds with the observation made in Section 3.3.2 regarding the difference between the predicted and measured pressure ratios, especially considering that the equations described in Section 2.5.1 are typically off by as much as 10% within the "bounds of validity." [62] All other criteria are met.

3.5 Conclusions

These measurements indicate that the operation of a static differentially pumped gas target at pressures up to 100 mbar is possible. The limiting factor on the static target pressure is the load on the second stage pump (the higher pressure turbopump). Such a target, with three pumping stages separating apertures of 10 cm length and 0.5 cm diameter, would allow much greater beam currents than are possible with either a solid target or a windowed gas target. Furthermore, the differentially pumped target would not be subject to the same levels of background radiation (from window and substrate materials) as would a windowed target. The windowless target would be better suited to thin target applications, as it would be simple to construct a target of such width as would lead to a very small energy spread in the resulting neutrons. This is an advantage over both a solid target, which would require more thickness for physical stability, and a windowed gas target, which would introduce beam straggling.

There are two conclusions which must be drawn from the measurements described. First, the turbopumps used are not capable of running at the pressures that would occur in the second stage of a 150 mbar static target, but limit the target pressure to 100 mbar. Higher pressures would allow much greater flexibility and utility in the target's applications.

Second, the calculational procedure used to design this target system is useful and effective as a means of predicting its behavior. In fact, it is somewhat conservative. This conservatism does introduce some error into the modeling procedure.

Chapter 4

Pulsed Target

The DL-1 RFQ with which the target system is used is a pulsed accelerator, operated with duty factors of approximately 2%. One immediate possibility raised by the pulsed nature of the incident ion beam is that the aperture could perhaps be made "low duty factor" as well.

To reduce the effective conductance of an aperture, one can allow gas to pass through that aperture, i.e., open the aperture, only for that portion of the duty cycle during which one wishes to inject the beam. This reduction in gas flow will allow a greater effective pressure drop across a given aperture. This could allow the pressure of the gas target system to be increased considerably.

4.1 Theory

If we consider an aperture which is blocked off by some sort of intermittent valve arrangement, a valve efficiency f may be defined as

$$f = \frac{q'}{q}, \tag{4.1}$$

where q' is the time-averaged flow rate through the aperture-valve combination, and q is the flow through the aperture without the valve. We can model the effect of this valve by repeating the flow balancing procedure described previously, replacing the

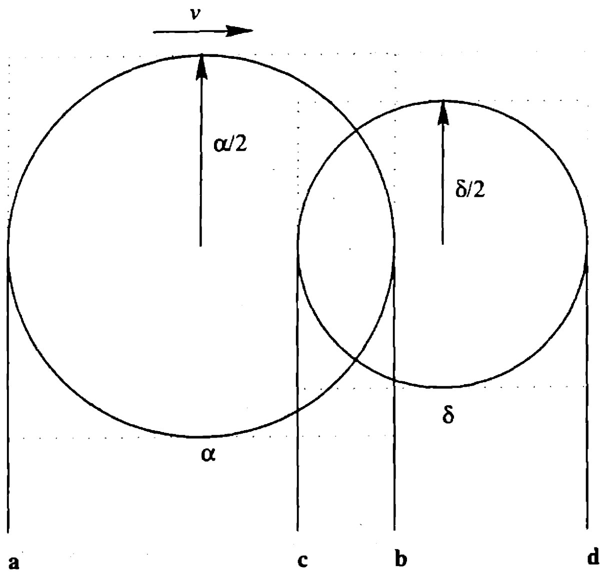

Figure 4-1: Naming conventions for describing the interaction of a moving aperture with a stationary aperture.

predicted flow rate between stages as calculated by standard conductance formulae with the product of that flow rate and this efficiency f. Several sources [58, 62] indicate that the value of the efficiency f could approach 0.1.

Any shutter apparatus will have to open for a certain period of time to allow the entrance of the beam. For that time period the noninfinitesimal opening will have to be completely open. Consider the shutter shown schematically in Figure 4-1. Define various times in the cycle of the opening of the aperture as t_1; the time that **b** passes **c**, t_2; the time that **b** passes **d**, t_3; the time that **a** passes **c**, and t_4; the time that **a** passes **d**. The values of the various times in the opening cycle will depend upon the nature of the relative velocity v of the apertures.

Constant Aperture Motion

For one aperture moving at a constant velocity v past another aperture, the times in the cycle are evaluated as:

$$t_1 = 0$$

$$
\begin{aligned}
t_2 &= \delta/v \\
t_3 &= \alpha/v \\
t_4 &= (\alpha+\delta)/v.
\end{aligned}
$$

Motion of this sort would result from an aperture located a distance r from the center of a disk rotating at shaft speed ω, where

$$v = 2\pi r\omega, \tag{4.2}$$

and ω is in cycles per second. The fully open time is

$$t_f = t_3 - t_2 = \frac{\alpha-\delta}{v}, \tag{4.3}$$

the opening (or closing) time is

$$t_o = t_2 - t_1 = t_4 - t_3 = \frac{\delta}{v}, \tag{4.4}$$

and the diameter α of the moving aperture required for a given t_f is

$$\alpha = vt_f + \delta. \tag{4.5}$$

As the turbulent flow rate through an aperture is generally proportional approximately to the square of the diameter (see Equation 2.5 and Equation 2.8), and thus to the area, a reasonable figure-of-merit for the efficacy of a suggested valve is the average open area of the aperture. This value can be obtained by multiplying the pulse rate by the integral of the product of time and open area over a single pulse.

If we assume square apertures, as also shown in Figure 4-1, then the integrated product of time and open area for a single pulse is

$$T\cdot A = \underbrace{\frac{1}{2}\delta^2\frac{\delta}{v}}_{opening} + \underbrace{\delta^2\frac{\alpha-\delta}{v}}_{open} + \underbrace{\frac{1}{2}\delta^2\frac{\delta}{v}}_{closing} = \frac{\delta^2\alpha}{v}. \tag{4.6}$$

Equation 4.6 provides an upper estimate of the integrated time area for circular apertures.

Given a rotating disk of velocity ω, with n equally spaced holes at a distance r from the center of rotation, the velocity v of the holes relative to a similarly located stationery hole will be as in Equation 4.2, and the frequency with which the aperture opens will be

$$F = n\omega. \tag{4.7}$$

The open time-area is

$$T \cdot A = \frac{\delta^2}{2\pi F} \cdot \left(2\pi r \frac{F}{n} t_o + \delta\right) \tag{4.8}$$

per pulse.

Sinusoidal Aperture Motion

If the relative velocity of the apertures is

$$v(t) = B\sin(2\pi\omega t), \tag{4.9}$$

where ω is one half of the desired pulse frequency, then the distance by which the center of the moving aperture trails the center of the stationary aperture is

$$h(t) = A\cos(2\pi\omega t). \tag{4.10}$$

Negative values of $h(t)$ indicate that the moving aperture has "already passed" the stationary aperture during that cycle. The various times in the opening cycle can then be defined as

$$t_1 = \frac{1}{2\pi\omega} \arccos\left(\frac{\alpha+\delta}{2A}\right) \tag{4.11}$$

$$t_2 = \frac{1}{2\pi\omega} \arccos\left(\frac{\alpha-\delta}{2A}\right) \tag{4.12}$$

$$t_3 = \frac{1}{2\pi\omega}\left[\pi - \arccos\left(\frac{\alpha-\delta}{2A}\right)\right] \tag{4.13}$$

$$t_4 = \frac{1}{2\pi\omega}\left[\pi - \arccos\left(\frac{\alpha+\delta}{2A}\right)\right]. \tag{4.14}$$

The times above can be determined by solving the equations

$$h(t_1) - \alpha/2 = \delta/2 \tag{4.15}$$

$$h(t_2) - \alpha/2 = -\delta/2 \tag{4.16}$$

$$h(t_3) + \alpha/2 = \delta/2 \tag{4.17}$$

$$h(t_4) + \alpha/2 = -\delta/2. \tag{4.18}$$

The fully open time t_f is

$$t_f = t_3 - t_2 = \frac{1}{2\pi\omega}\left[\pi - 2\arccos\left(\frac{\alpha-\delta}{2A}\right)\right]. \tag{4.19}$$

The time during which the aperture is opening or closing is

$$t_o = t_2 - t_1 = t_4 - t_3 = \frac{1}{2\pi\omega}\left[\arccos\left(\frac{\alpha-\delta}{2A}\right) - \arccos\left(\frac{\alpha+\delta}{2A}\right)\right]. \tag{4.20}$$

Finally, the integrated time area product can be calculated (again for square apertures) using the open height $H(t)$, which is defined (for the opening segment of the cycle, $t_1 \le t \le t_2$) as

$$H(t) = \frac{\delta}{2} - \left(h(t) - \frac{\alpha}{2}\right) = \frac{\alpha+\delta}{2} - Acos(2\pi\omega t). \tag{4.21}$$

The integrated time area for the first portion of the cycle is

$$T \cdot A = \int_{t_1}^{t_2} \delta H(t)\, dt. \tag{4.22}$$

Evaluation of this integral gives

$$T \cdot A = \frac{\delta}{2\pi\omega}\left\{\frac{\alpha+\delta}{2}\left[\arccos\left(\frac{\alpha-\delta}{2A}\right) - \arccos\left(\frac{\alpha+\delta}{2A}\right)\right] - A\left[\sqrt{1-\left(\frac{\alpha+\delta}{2A}\right)^2} - \sqrt{1-\left(\frac{\alpha-\delta}{2A}\right)^2}\right]\right\}. \quad (4.23)$$

While this calculations are made for square apertures, it should be noted that the integrated product of time and area for square apertures approaches that of round apertures as the two diameters α and δ approach each other. Furthermore, the results will be used in a comparative fashion. Thus, the approximation should not have a significant effect.

In order to compare apertures moving in a constant-velocity fashion with apertures moving in a sinusoidal fashion, we can require that they produce the same effective aperture opening during the cycle. The constants α and A can be determined by fixing any two of the three values t_f, t_o, and $T \cdot A$. As a given fully-open time t_f is required, either t_o or $T \cdot A$ can be used to fix the values of α and A using Equations 4.19, 4.20, and 4.23, respectively.

For example, consider an aperture of 5 mm diameter which is fully open for a period of 56.4 μs at a frequency of 200 Hz. The diameter α of the aperture moving at constant velocity is given by Equation 4.5. The minimum number of holes for a balanced rotor is two. One solution for such a system has apertures of diameter $\alpha = 6.35$ mm for a radius $r = 38.1$ mm. The value $T \cdot A$ for this case would be 16.65 ms$\cdot$mm^2 per pulse, which gives a time-averaged open area of 1.33 mm^2, resulting in an areal duty factor of 6.36%. If an aperture moving in a sinusoidal manner were matched to the same fully open time $t_f = 56.4$ μs and the same open time $t_p = 475$ μs, the moving aperture has a diameter $\alpha = 6.35$ mm, and the amplitude $A = 38.1$ mm. The resulting $T \cdot A$ is 12.6 ms$\cdot$mm^2 per pulse. If, however, t_f and $T \cdot A$ are used in the matching process, the required $\alpha = 7.70$ mm, and the amplitude $A = 76.2$ mm. Realizing that the actual range of motion of the sinusoidal aperture is twice the value of A, it is readily apparent that such a system cannot be based upon an aperture moving in a sinusoidal manner, at least not for this large an aperture.

Were the aperture small enough that a sinusoidal actuating mechanism could work, and perhaps the desired pulse rate lower, there are a number of ways in which very small devices could be used to actuate the valve. Piezoelectric actuators, shape memory wires, and solenoids could all possibly be used to actuate very small resonant systems through a range of motion of 2–3 mm.

4.2 Factors Affecting Valve Efficiency

A number of factors other than those discussed in the previous section may influence the efficiency of a rotating valve arrangement. Characterizing the valve by the dimensionless efficiency f will allow study of more of these dependencies in an independent manner than would characterizing the valve by the absolute difference in flow rates.

Obviously, the size of the apertures α and δ and the upstream pressure p_u will have the greatest effect on the flow rate through an aperture. However, these parameters are not really characteristic of the valve, but of the entire flow system. The specifics of the valve system which may be of importance could include the dimension of the gap between the rotating disk and the stationary flange will affect leakage past the valve, as would the radius of the rotating disk and the position of the aperture along that radius. The amount of time the aperture spends opening and the amount of time between open periods may affect the formation of equilibrium flow, thus changing the gas flow rate. These formation times may be affected by the speed of sound in the gas, and thus by the gas pressure. Finally, if there are multiple valved apertures, there may be coupling between them dependent upon the physical distance between the valves.

The magnitude of f was determined in order to assess the value of a rotating valve arrangement within a differentially pumped system. The dependence of the valve efficiency f upon the gap width g, the upstream p_u, and the opening frequency F was measured to determine an appropriate regime of operation for such a differentially pumped system. The dependencies measured indicate possible routes for the

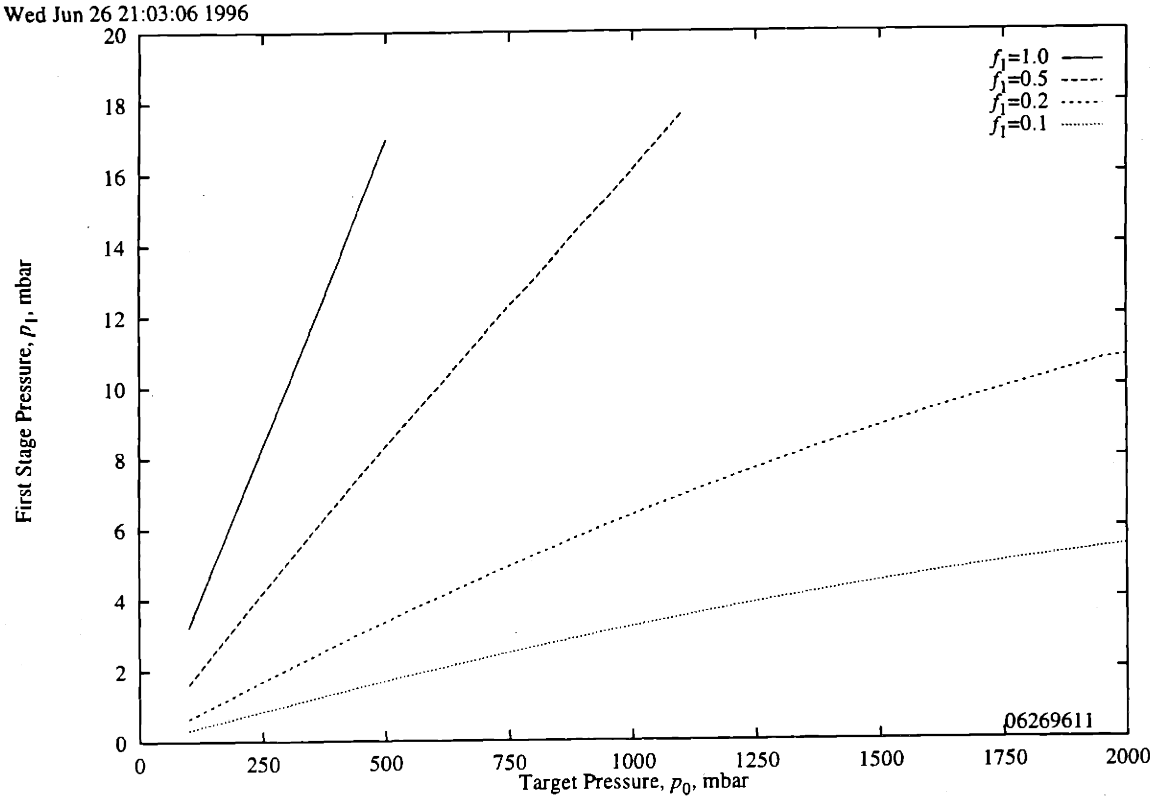

Figure 4-2: Equilibrium first stage pressure for various target pressures and various valve efficiencies f_1. The higher pressure aperture is 25 cm long and 0.5 cm in diameter, the lower pressure aperture is 10 cm long and 0.5 cm in diameter.

improvement of this type of valve, but an exhaustive optimization of the valve is beyond the scope of this work.

4.3 Predicted Effects

The effects of such flow reductions can be predicted by repeating the calculations in Section 3.1 for gas inputs scaled by the factor f. In the case of the first pumping stage, the static calculations lead to pressure differences as shown in Figure 3-3 for various apertures. In the case of the 25 cm long by 0.5 cm diameter aperture, reducing the incoming flow q_1^* to $f_1 \cdot q_1^*$ for various values of f_1 results in the pressure drops shown in Figure 4-2.

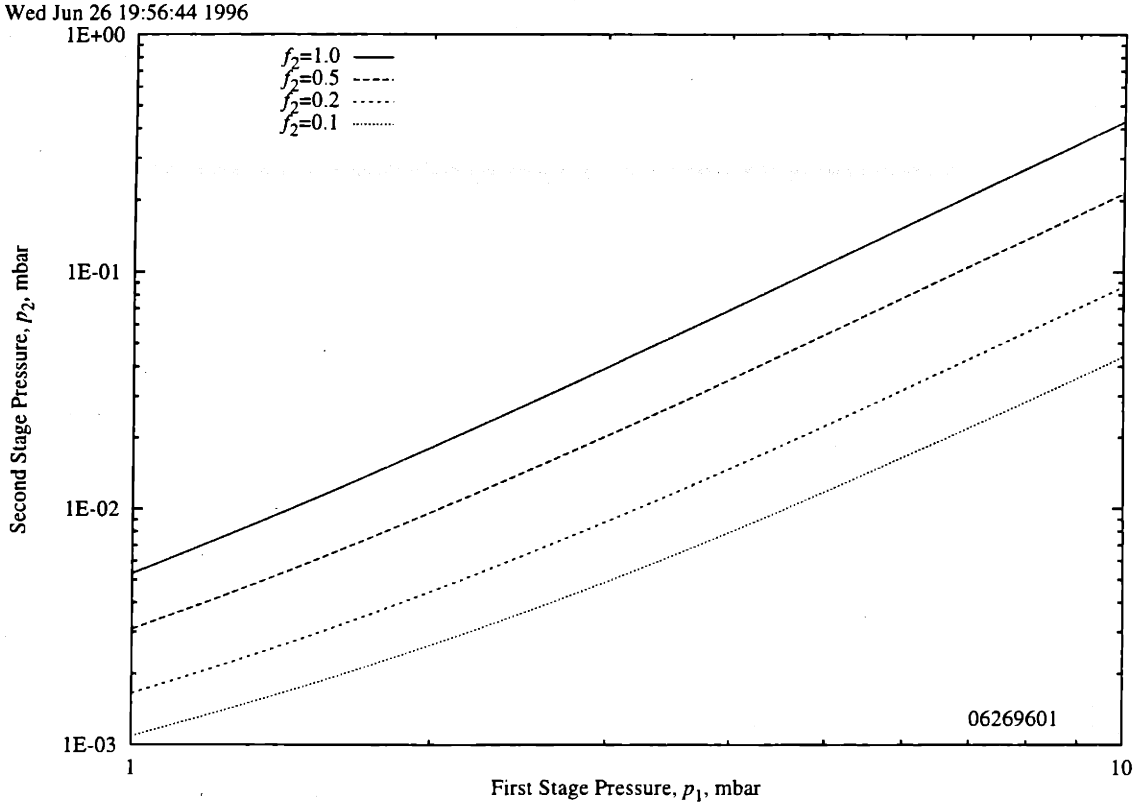

Figure 4-3: Equilibrium second stage pressure as a function of first stage pressures for various valve efficiencies f_2. Both the upstream and downstream apertures are 10 cm long and 0.5 cm in diameter.

For the second aperture, the static pressure drop for various apertures was calculated previously as shown in Figure 3-4. The same scaling process for a 10 by 0.5 cm aperture as used on the first aperture yields the data shown in Figure 4-3. A similar effect can be seen for the third aperture, for which the static data are shown in Figure 3-5. The results are shown in Figure 4-4.

4.4 Valve Design

As a result of calculations performed in the previous section, a rotary valve was designed to operate on the first and second apertures of the differentially pumped target. The rotor arrangement is located within the target, which is a 4" vacuum

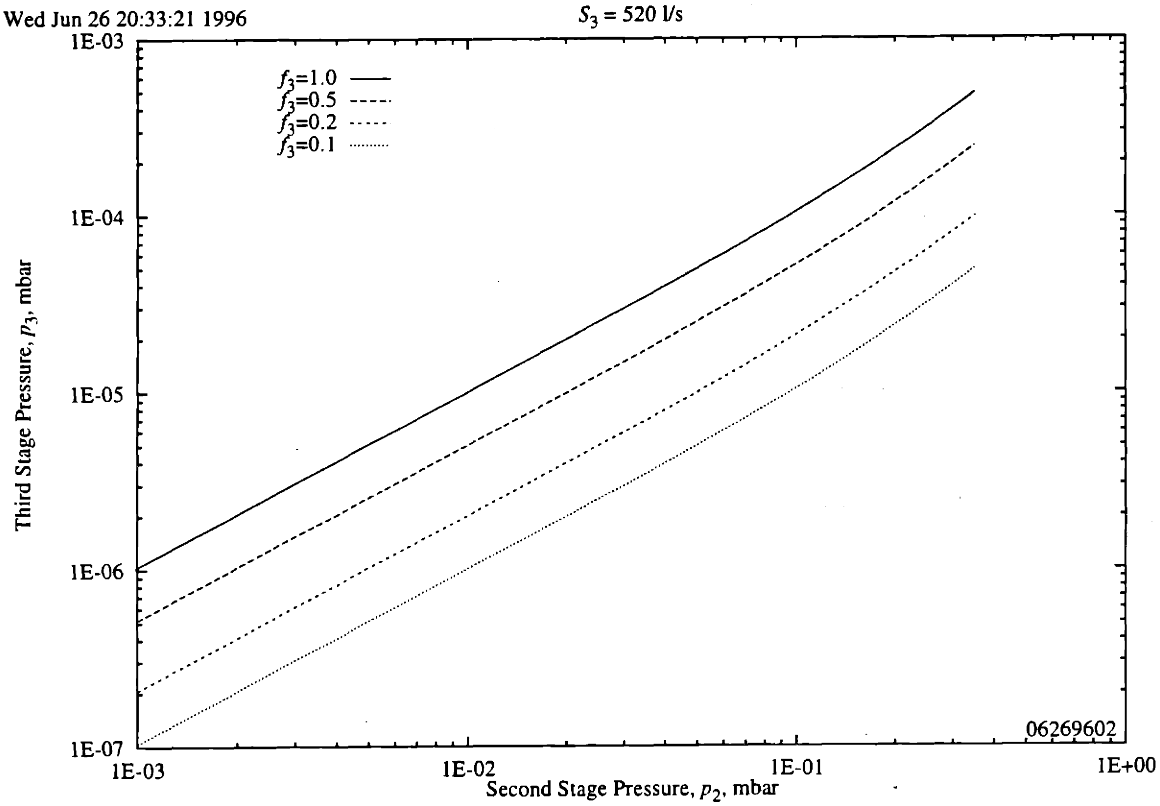

Figure 4-4: Third stage pressure as a function of second stage pressure for various valve efficiencies f_3 (10 cm by 0.5 cm apertures).

tube described in Figure 4-5.

A schematic drawing of the rotor and drive assembly appears in Figure 4-6. The rotor fits into the first pumping stage, shown in Figure 4-7. The clearance between the faces of the rotor and the stationary plates can be varied from 0.13–0.65 mm. The rotor is magnetically coupled through a 1.6 mm wall of 304 stainless steel. This magnetic coupling permits the motor and drive system to be external to the vacuum system. The single shaft design of the rotor guarantees that the apertures are aligned and synchronous. The rotor assembly is composed of 316 stainless steel and 6061 aluminum, with bearings of a Teflon-loaded polymer. All materials were selected for low out-gassing and reasonable heat resistance. As the shaft is intended for possible high-speed (6000 rpm) use, it was further designed to be quite stiff.

4.5 Valve Construction

Some difficulties were experienced in the construction of the target and rotor assemblies. The pumping flange in the first pumping stage contracted somewhat after being welded into the primary pipe, resulting in the pipe bending such that the flange and the end-wall of the first stage were laterally displaced from one another by some 0.090 inches, and were out of parallel by 0.040 inches over their 4 inch diameters. As a result, the rotor assembly as designed was unable to turn within the space provided.

To overcome this difficulty, the face of the first stage end-wall was faced off smooth and perpendicular to the beam apertures. The conflat flange to which the "Near Flange" is bolted was faced off smooth and parallel to the end-wall, and pinned such that the near flange would be centered relative to the end-wall. The rotor shaft was recut to fit the modified target assembly, to a length of 5.895 inches within a space of 5.907 inches. The remaining 0.012 inches of space was taken up by Belleville washers, which also increased the stiffness of the bearing assembly, increasing the critical shaft speed. The rotors were stepped and chamfered on their outer diameters to provide a more labyrinthine pathway for the gas. However, the space within which the rotors turned was somewhat oversized, resulting in a typical gap (on the

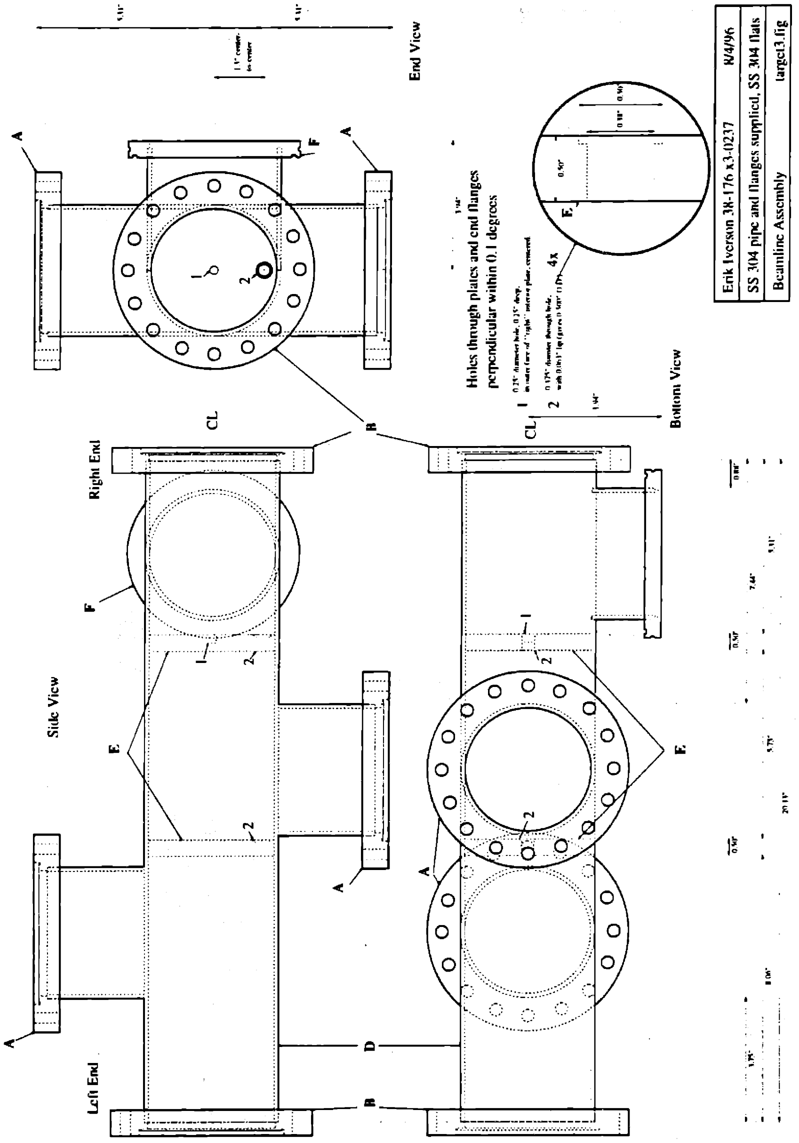

Figure 4-5: Shop drawings for the gas target assembly.

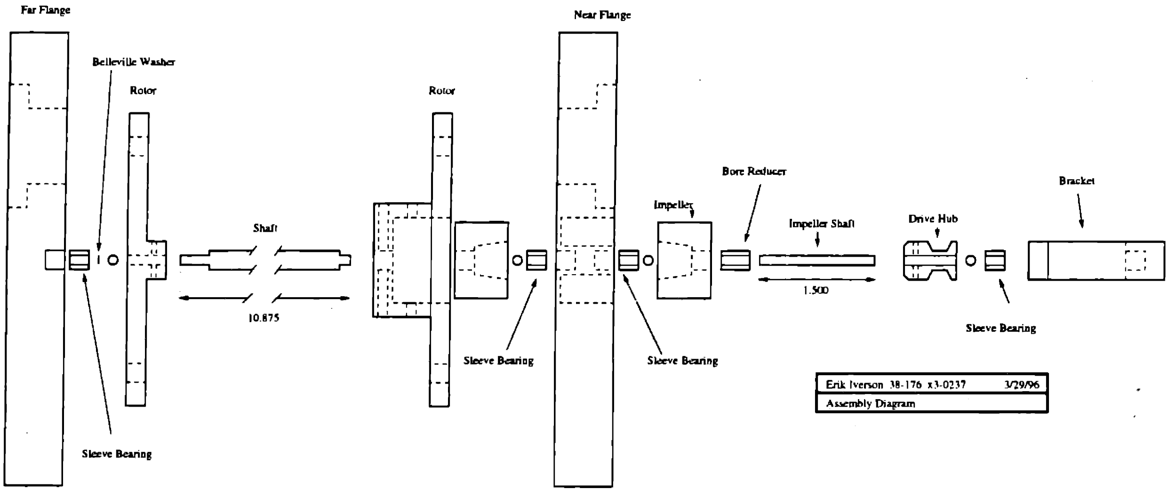

Figure 4-6: Schematic of rotor and drive assembly.

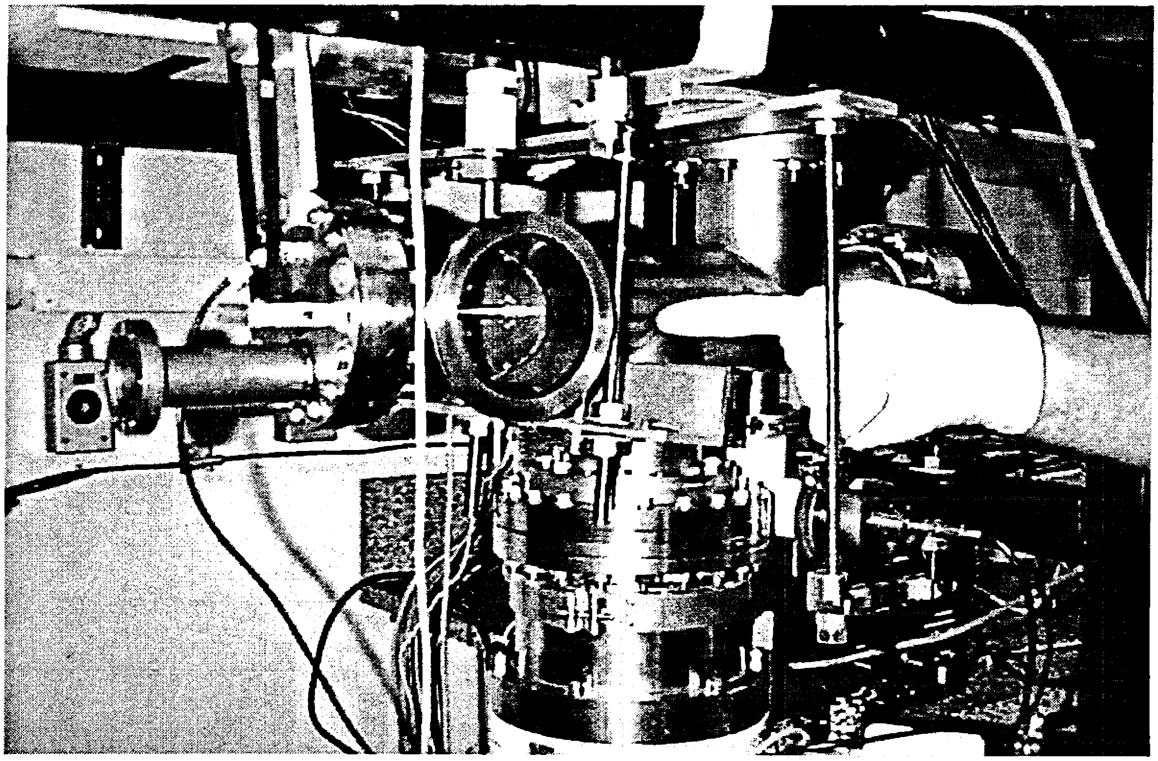

Figure 4-7: Gas target showing installed rotor. The Roots blower and target plenum have been removed.

diameter), approaching 1.5 mm. However, this proved to be necessary, as the shaft journals were poorly matched to the bearings (3.15 and 3.23 mm respectively), and the rotor displayed some eccentricity which led to rapid bearing wear and increased runout.

The magnetic drive assembly was chosen to permit economical high-vacuum operation at high rotational speeds. Typical rotary vacuum feedthroughs are capable of limited speeds, typically on the order of 500 rpm. Ferrofluidic seals were deemed too expensive in the initial design. Placing the motor within the vacuum chamber involves a much greater cost and much bulkier vacuum system. The magnetic feedthrough is extremely cost-effective, with all parts totaling less than $250. It is capable of sustained high-speed operation (greater than 6500 rpm), and requires only that the flange material be relatively non-conductive, such as stainless steel. All small mechanical components were obtained from Precision Industrial Components (Middlebury, Connecticut). The drive magnets are Alnico 5 rotor magnets, with each rotor face an alternating pole. The magnets were purchased from McMaster-Carr Supply Company (New Brunswick, New Jersey).

An S27311 optical sensor was positioned opposite the beam aperture to monitor the rotor motion. This is a reflective infrared device which, when used with a T41300 high speed amplifier, is capable of rise times on the order of 10 ns and frequencies of hundreds of kilohertz. The sensor and amplifier were obtained from the Clarostat Sensors and Controls Group.

4.6 Valve Performance

The efficiency of valves were measured by monitoring the pressures upstream of the valve locations for constant flow rates. Various values of upstream pressure p_u, pulse rate F, and gap spacing g were used for both the first stage aperture valve and the second stage aperture valve. Furthermore, the tests of the second stage valve were performed with and without first stage pumping to determine any coupling between the two apertures.

4.6.1 Laminar Uncoupled Flow

The valve efficiency was first tested for conditions such that the flow in the corresponding static case was laminar. Only the second pumping stage (i.e., the higher-pressure turbopump) was used, so that the degree of coupling, if any, between the two rotors could be determined. To perform these tests of the valve efficiency f, the flow rate through the system was held constant. When the rotor rotation began the upstream pressure increased until it drove this flow rate through the pulsed aperture under (assumed) blocked flow conditions. Referring to Equation 3.7, such a flow rate should be proportional (for round static apertures) to the square of the driving pressure. Thus, the valve efficiency f is evaluated as

$$f = \left(\frac{p}{p'}\right)^2 , \tag{4.24}$$

where p is the upstream pressure in the static case, and p' is the upstream pressure in the pulsed case. In the event that the flow rate through the dosing valve changes (due to a change in pressure or temperature of the feed gas, for example), the inlet pressure at the turbopump can be used for normalization;

$$f = \frac{p'_K}{p_K}\left(\frac{p}{p'}\right)^2 . \tag{4.25}$$

Figure 4-8 shows the valve efficiency f measured for air under these conditions for a variety of upstream pressures p_u and gap thicknesses g as a function of shutter frequency F. Similar data for helium is shown in Figure 4-9.

The data graphically show what can be statistically demonstrated; the valve efficiency f is independent of the shutter opening frequency F and the upstream pressure p_u, and is strongly affected by the gap spacing g. The dependence upon F was determined by calculating the Fisher's z coefficient for each set of data $f(F)$ for a given g and p_u. The significance of the dependence upon F ranged from 0.10 to 0.75, indicating no significant correlation.

Once f was shown to be independent of F, the Student's t test indicates whether

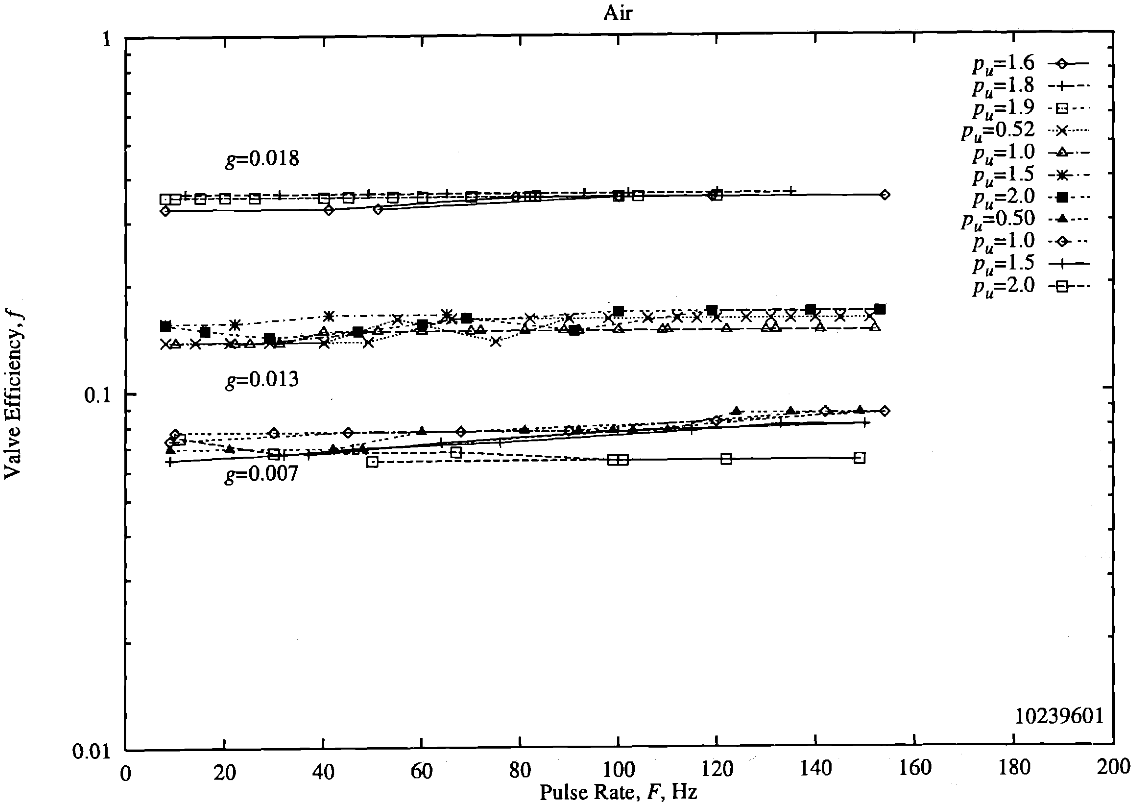

Figure 4-8: The efficiency of the rotating shutter valve in air as a function of opening frequency for various pressures and gap thicknesses (g in inches).

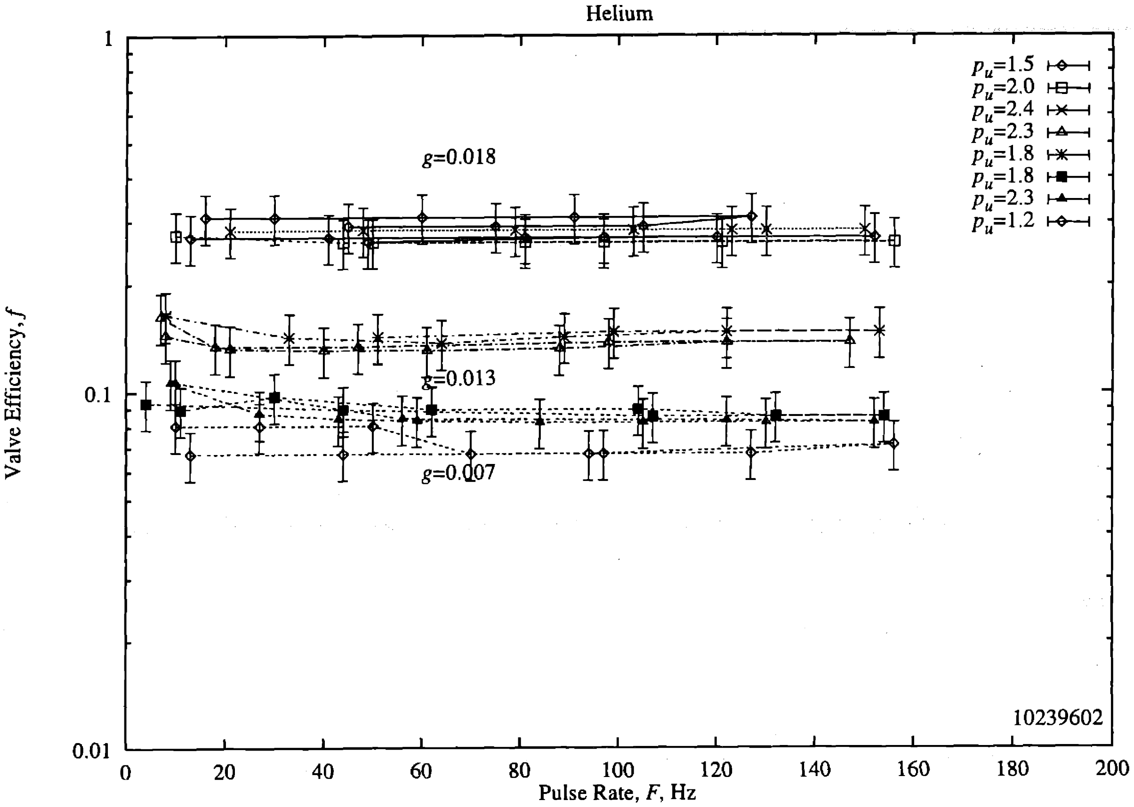

Figure 4-9: The efficiency of the rotating shutter valve in helium as a function of opening frequency for various pressures and gap thicknesses (g in inches).

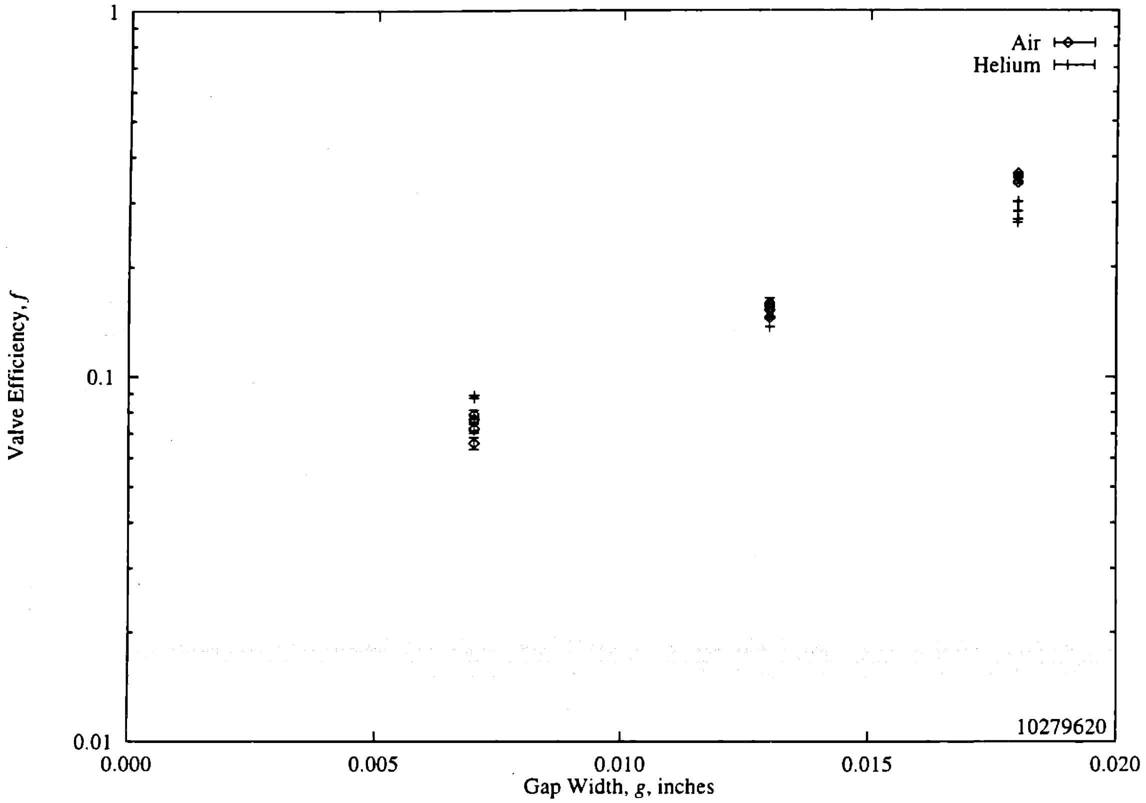

Figure 4-10: The efficiency f of the rotating shutter valve in laminar flow as a function of the gap width g.

f is dependent upon p_u and/or g. The data were found to be independent of p_u, with significances ranging from 0.3 to 0.9, and dependent upon g, with significances less than 0.01. Figure 4-10 shows f averaged over F and p_u as a function of gap width g for both helium and air. Comparing the data for the two gasses at each of the gap widths indicated that the valve efficiency was not determined by the gas species, with significances of 0.2 to 0.6. Rough extrapolation of the data in Figure 4-10 to $g = 0$ gives a valve efficiency very similar to the areal duty factor of 6.4% calculated previously.

4.6.2 Turbulent Flow

The valve efficiency f for an aperture with turbulent flow displayed behavior quite similar to that displayed for laminar flow. There was no significant dependence upon

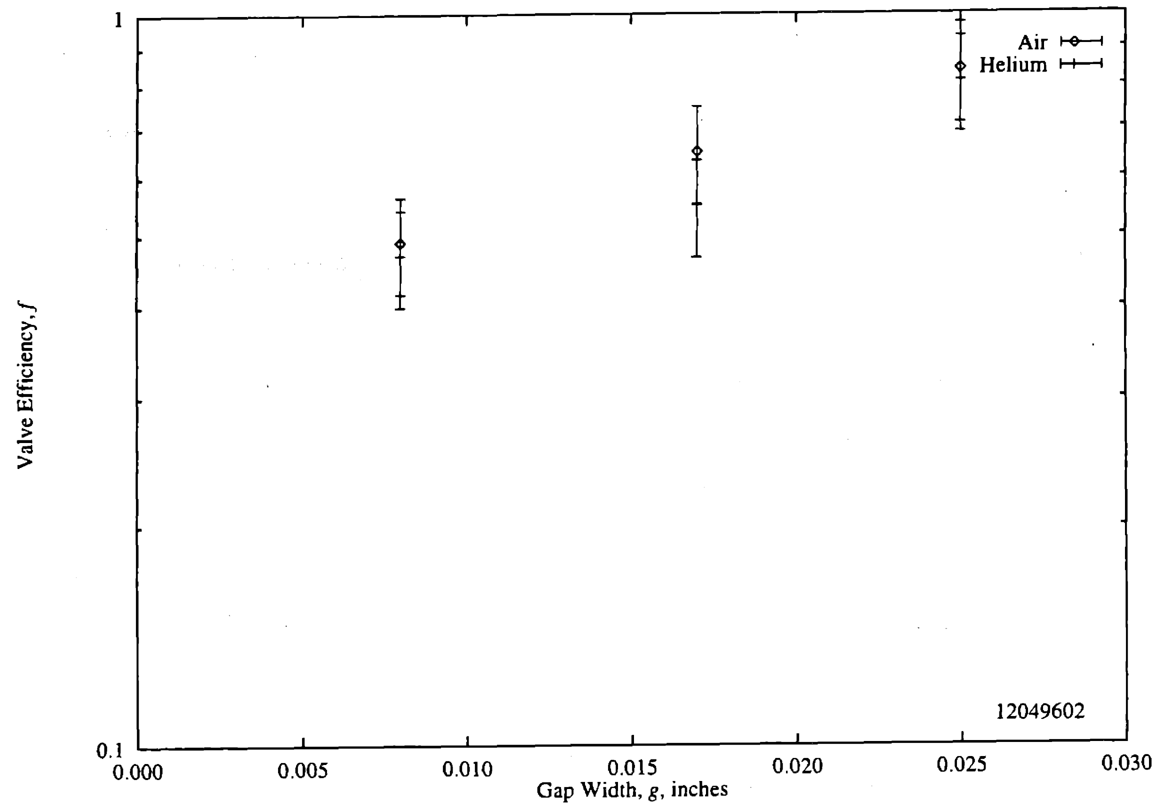

Figure 4-11: The valve efficiency $f(g)$ as a function of gap width g for turbulent flow.

gas species, upstream pressure, or opening frequency F, as for laminar flow. Finally, the gap width g had significant influence upon f, as shown in Figure 4-11.

It should be noted, however, that f is significantly different for turbulent flow than it is for laminar flow. This can be seen in Figure 4-12, which shows all aggregate data for $f(g)$. One explanation for this difference is that the motion of the rotor induces turbulence in the laminar flow, thus decreasing the flow rate. When the flow is already turbulent, this contribution to the valve efficiency would not occur. This hypothesis could be tested by some means of flow visualization, or possibly by some other means of inducing turbulence in normally laminar flow.

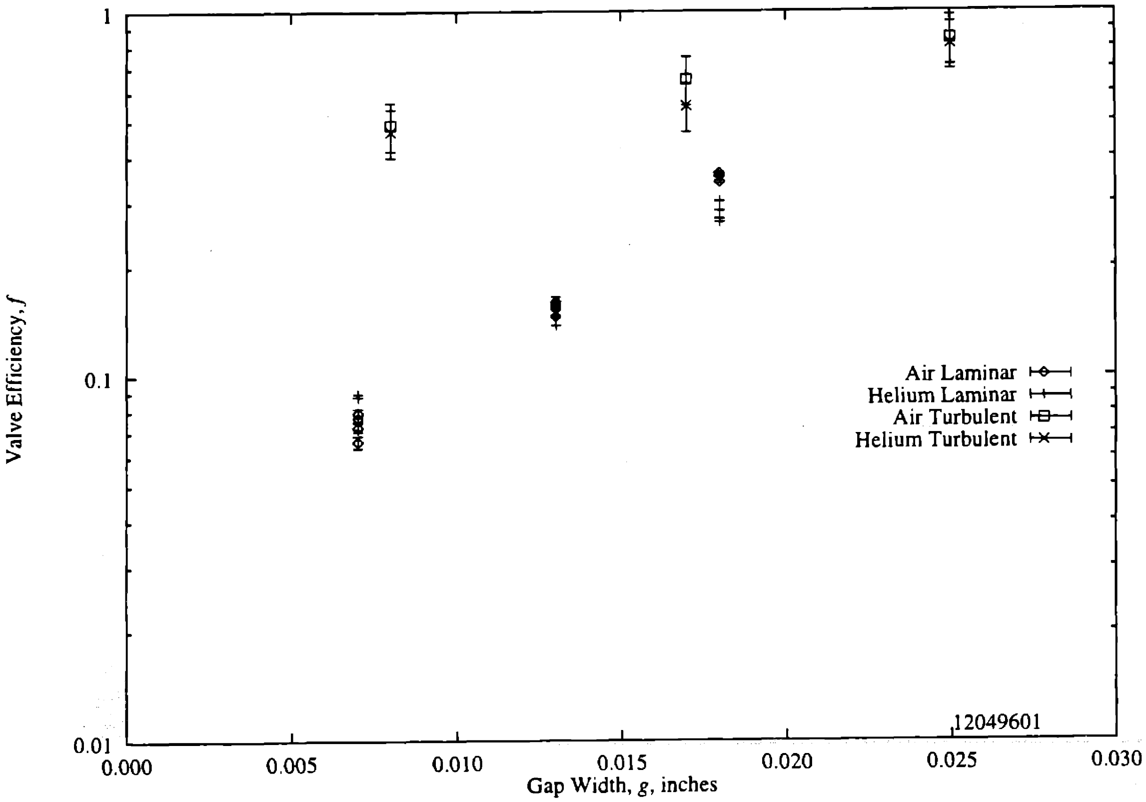

Figure 4-12: The valve efficiency $f(g)$ as a function of gap width g for both turbulent and laminar flow.

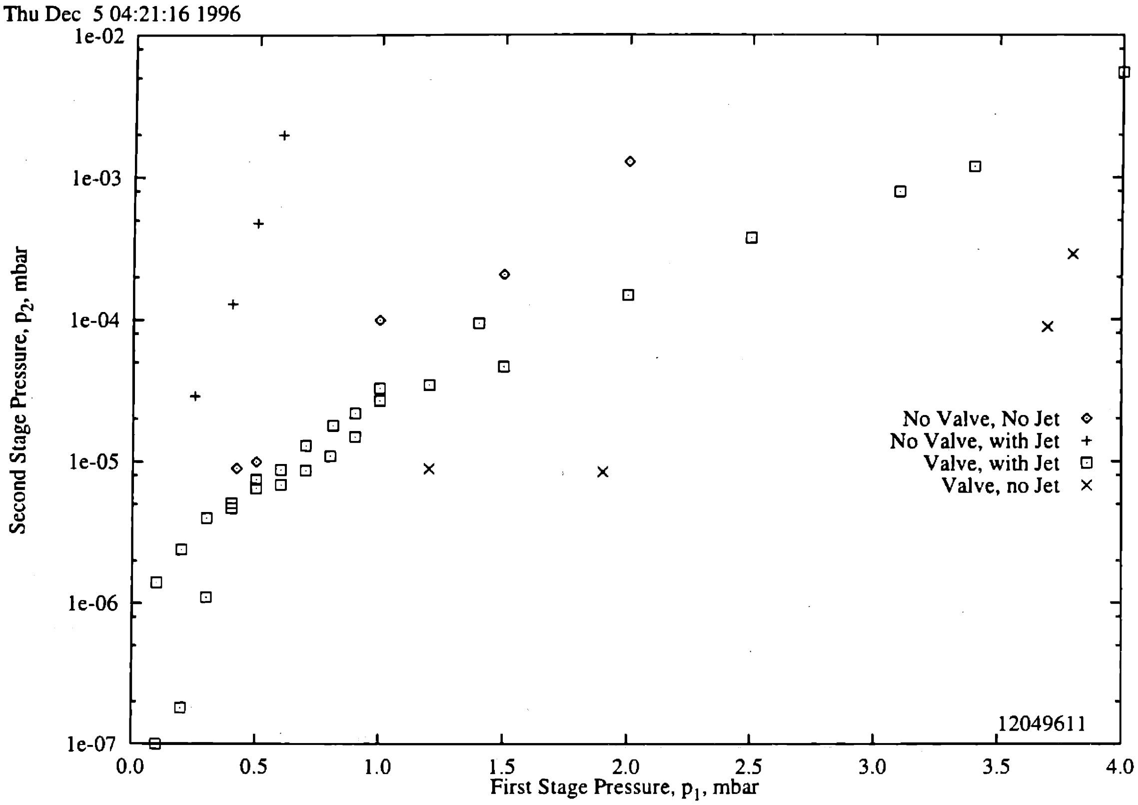

Figure 4-13: Comparison of coupled and uncoupled apertures.

4.6.3 Coupled Flow

A further consideration is coupling between the two apertures. As the apertures are relatively close to each other, and must be aligned in order to permit the passage of the accelerator beam, it is not impossible that the free-jet expansion of the blocked flow from the higher pressure aperture will result in a smaller pressure drop across the second aperture, due to both the increased local pressure around the beginning of the second aperture, as well as to the fact that the flow would be anisotropic, with the strongest component directly in line with the second aperture. Figure 4-13 shows four different sets of data;

1. $p_0 = p_1$, i.e., there is no first aperture and no rotary valve (diamonds),

2. $p_0 > p_0^* > p_1$, with no rotary valve (crosses),

3. $p_0 > p_0^* > p_1$, with rotor spinning (squares),

4. $p_0 = p_1$, i.e., there is no first aperture and the rotary valve is in place (diagonal crosses).

As can be seen from the data, the presence of the jet from the first aperture significantly degrades the performance of the second aperture, both with (squares to diagonal crosses) and without (crosses and diamonds) the rotating valve in operation. However, comparing squares to diamonds indicates that the jet from the first aperture, while it does still degrade the performance of the second aperture, is countered by the rotor's effect, although such countering could be attributable to either the first or second rotor. Further tests could be designed to determine which rotor was responsible, if not both.

In summary, the coupling between the apertures is very definitely a significant concern in the design of such a system. An arrangement of flow "scrapers," which did not block the beam line but did direct at least a portion of the expansion jet away from the second aperture could have a significant benefit. Furthermore, the coupling of the first and second aperture indicate that there could be a similar state of affairs between the second and third apertures. The design of this target prevented a third rotating valve from being implemented—it could be very advantageous to modify the design in such a way that this would be possible.

4.7 Attainable Pressure Drops

The maximum attainable target pressure is determined by the load on the higher-pressure turbopump, which is function of the pressure in the second pumping stage. Figure 4-14 shows the second stage pumping pressure p_2 that results from the target pressure p_0 for air in the static and pulsed cases. Immediately apparent from the graph is the tremendous increase in target pressure possible given the use of the rotating valve. The corresponding data for helium is shown in Figure 4-15. It is obvious here as well that the use of the rotating disk valve significantly increases the

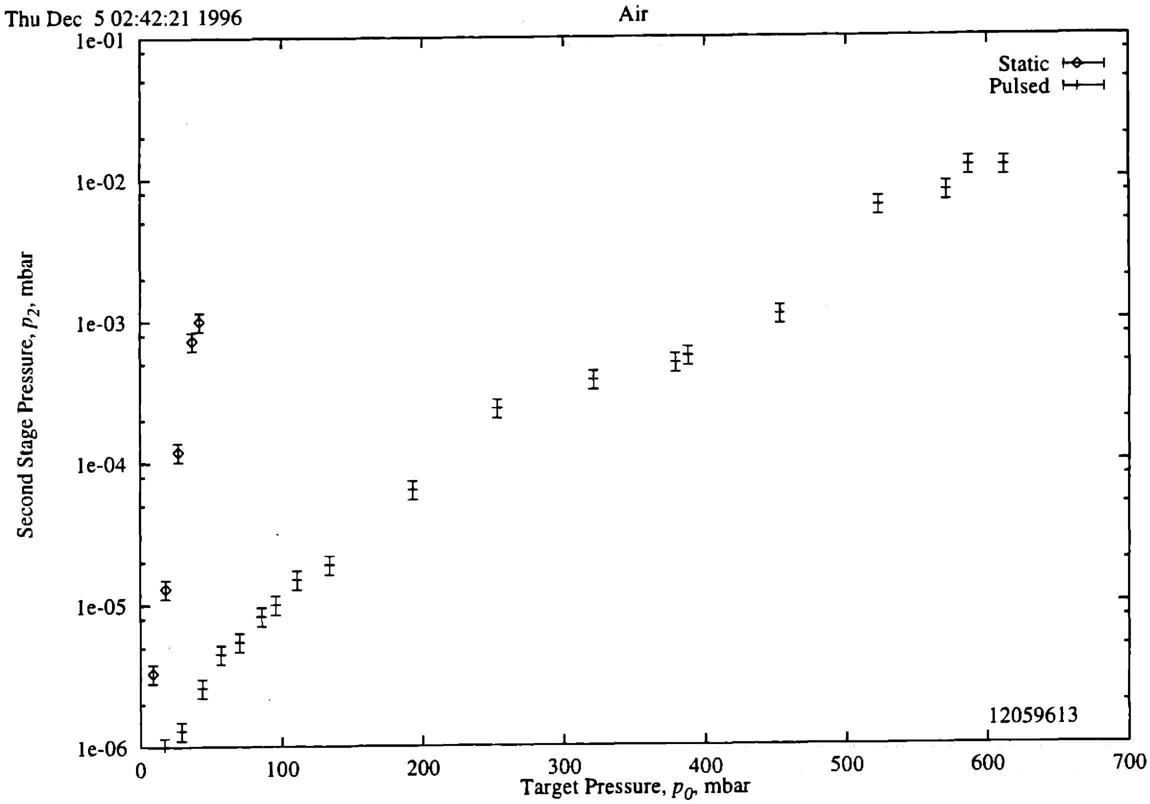

Figure 4-14: The air target pressure which results in the limiting pressure in the second pumping stage.

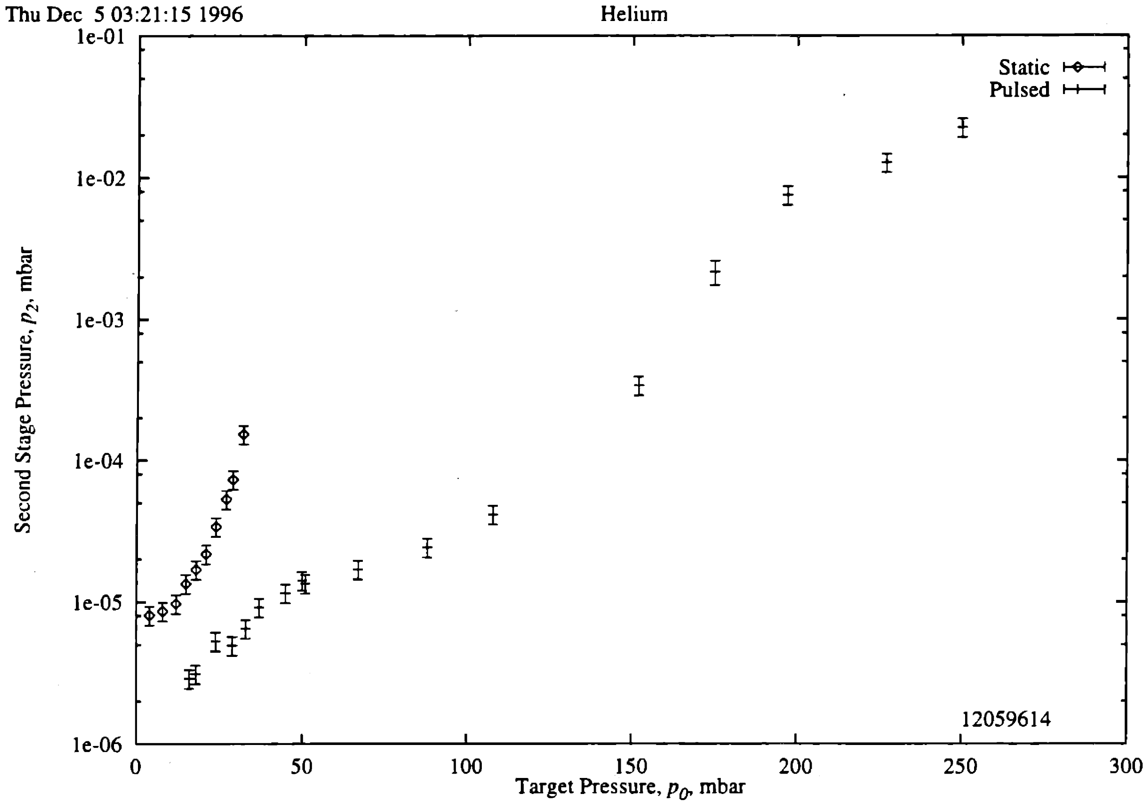

Figure 4-15: The helium target pressure which results in the limiting pressure in the second pumping stage.

maximum target.

4.8 Conclusions

As can be seen in the previous sections, the inclusion of a rotating valve arrangement results in considerable reduction of the gas flow between differentially pumped stages of the gas target system. This reduction extends the maximum pressure attainable with a gas target tremendously. The most significant effect observed was the reduction in the coupling between the two valved apertures. Using the rotating disk valve permits the operation of the gas target to be extended from approximately 40 mbar for either air or helium in the static case to some 600 mbar for air and 250 mbar for helium in the rotating valve case. In either situation, the limiting factor is the pressure in the second pumping stage, which results in the TMU 520 turbopump working at its maximum capacity as indicated by the drive current required to maintain speed.

Chapter 5

Gas Target Operating Experience

5.1 Target Installation

The gas target assembly described in Chapter 4 was installed on the beamline of the DL-1 accelerator. The primary challenges involved in the installation of the target system included the alignment of the differentially pumped apertures with the beam and the relative timing between the rotating shutter apparatus and the accelerator pulse.

Alignment

The gas target assembly was installed on the beamline of the DL-1 accelerator. The assembly was optically aligned with the line of the beam by sighting with a level transit along the bore of the RFQ through a glass viewport at the end of the target, while the system was under vacuum and the injector arc was operating. The deuterium arc in the ion source provided lighting for the entire process. Obviously, this operation was performed with the accelerator itself off, as well as the high-voltage extraction and focusing anodes. The deuteron energy was thus not high enough to give rise to radiological concerns.

The reference points used for alignment were as follows:

1. The aperture in the plasma expansion cup in the duoplasmatron (0.50 mm in

diameter). The light emitted from this aperture provided a defocused backlighting for the remaining reference points.

2. The end of the RFQ vanes nearest the target system. These vanes are separated by a distance of 3.20 mm, and appear as shadows entering the bore of the machine at 90° intervals.
3. The target aperture nearest the accelerator. This aperture has a diameter of 5.00 mm, and appears as a circular shadow against the purple glow of the ion source.
4. The target aperture nearest the accelerator. This aperture also has a diameter of 5.00 mm, and is actually visible from the front.

By estimating the degree of eccentricity of each of these reference points as a fraction of their characteristic dimension, it was possible to align each section of the target and accelerator to within 0.25 mm of the same line.

Because of the particulars of this target arrangement, it was impossible to do a bore sighting to align the end of the beam tube farthest from the accelerator. The beam tube was aligned in much the same fashion as described above, prior to the installation of the target. The reference point used was the turned center of a blanking flange on the gate valve at the end of the beam tube. Unfortunately, it proved impossible to install the target and connect it to the beam tube without disturbing this alignment. As the rest of the system was aligned, the eccentricity of focusing magnets resulted in the beam being steered away from the actual apertures. That portion of the beam which did then pass through the apertures was on the tail of the focussed spot. This could clearly be seen by the nature of the beam spot when the accelerator was operated. This spot, as viewed remotely via a video camera observing the scintillation light from a quartz beamstop, was somewhat off-center and occluded if the alignment was only slightly off. If the misalignment was large, the halos that surround a focused beam were clearly visible, their curvature indicating the location of the true beam centroid. The end of the beam tube could then be moved until beamspot was centered within the aperture. An additional check was provided by the vacuum gauge on the target system, near the first aperture which collimates the beam. When the beam was poorly aligned, this gauge registered a marked increase in pressure due to the ions causing rapid desorption of gas from the target system wall. This increase was much reduced once the beam was aligned. The beam focusing done as described in Appendix B was such that a reasonable portion (approximately 70%) of the beam which reached the end quartz without the apertures also did so with the apertures in place.

Timing

The matching of the rotating shutter and the accelerator pulse was accomplished by monitoring the rotation of said shutter with an electro-optical scanning device as previously described. This device provides a signal nominally associated with the angular proximity of the scanner to the shutter hole opposite the one actually crossing the beam aperture. The field-of-view of the scanner provides some uncertainty in the actual relationship between the beginning of the observed pulse and the time at which the aperture begins to be either partially or fully open. However, this uncertainty did not significantly affect the way in which the signal was employed.

One option for matching the pulse time and the open time is to drive a synchronous motor in such a way that the shuttered aperture is opened at the appropriate time to admit the beam. This time would be provided by the internal clock mechanism of the accelerator system, which allows a pulse rate of approximately 2–640 Hz. The disadvantage with this method of timing is that the motor required to perform such a task at high speeds would be relatively expensive. As most of the applications foreseen for this target would not require a particularly consistent pulse rate, a more convenient arrangement is to have the accelerator itself triggered from the signal provided by the optical scanner described above. As the DL-1 accelerator used was not configured to allow an external trigger, it was accordingly modified.

One complication in such modification is that, as described in Section 4.1, the beam aperture actually begins to open a considerable time before the aperture is

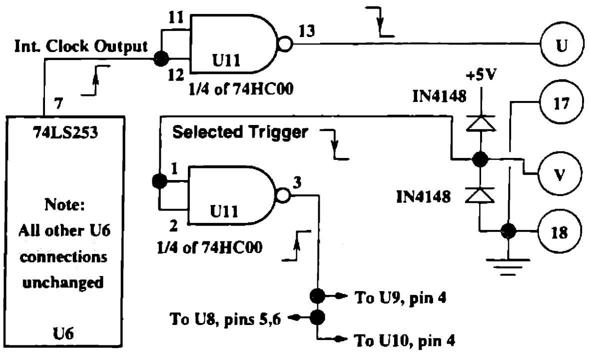

Figure 5-1: Modifications to the DL-1 Timing Generator Board for external triggering.

fully open and the accelerator can be triggered. Even at the maximum speed for which the shutter system was designed (200 Hz), the necessary delay is on the order of 200 μs—more than twice the adjustable delay provided for in the accelerator control system. The signal generated by the optical scanner is therefor given a digital delay empirically determined to be slightly less than half of the total length of the signal from the scanner. For operation as described below, at low pulse rates (25 Hz), this was quite adequate as the accelerator pulse, which is limited by the RF electronics and the control system to no more than 100 μs, was required to be within a 500 μs window of opportunity. The total length of the signal generated by the scanner in this configuration was 2.3 ms. Thus the timing was fairly forgiving of error at these rotation speeds and beam pulse lengths.

Portions of the timing generator board of the DL-1 as modified to allow a selection between internal and external triggering appear in Figure 5-1. These modifications required no additional chips, as chip U11 (a quad channel NAND gate) had two unused channels. The modifications did require the addition of two IN4148 diodes.

Two female BNC bulkhead connectors and a single-pole double-throw switch were added to the injector control cabinet to allow for trigger input, monitoring, and selection. The switch selects between the output of the internal clock and the input of the external trigger, returning the selected signal to the timing generator board. The input of the external trigger was put through a current limiting 100 Ω resistor.

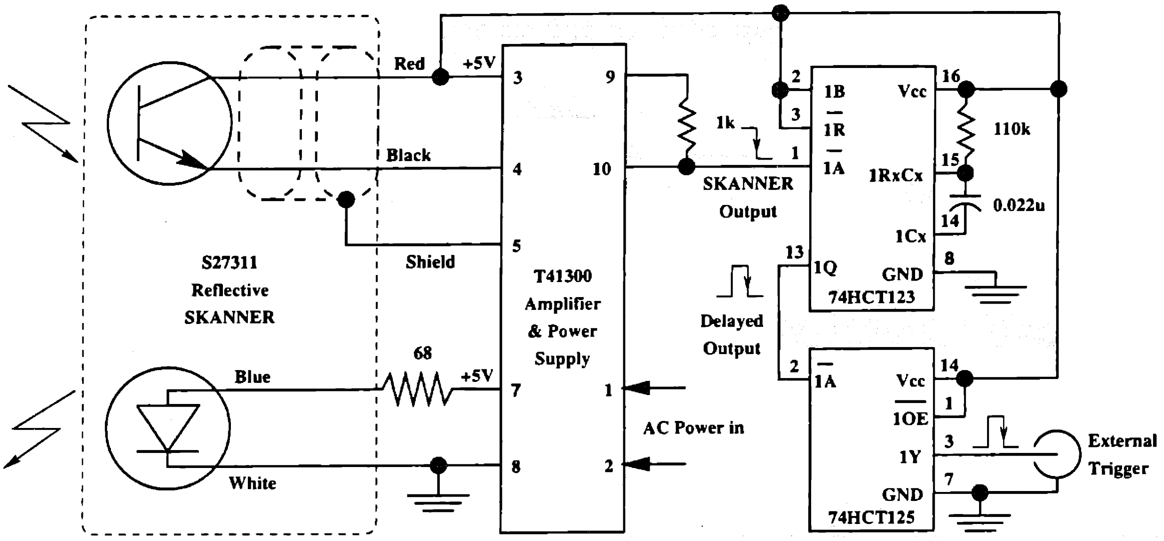

Figure 5-2: The electronics for triggering the accelerator from the rotating shutter.

The output of the optical scanner is amplified with a high-speed open transistor output amplifier and digitally delayed by a preset amount, empirically determined for a particular shaft speed. This circuit is described in Figure 5-2. The 74HCT123 monostable multivibrator provides a positive pulse beginning with the negative-going edge from the amplified scanner signal. The length of this pulse is determined by the value of the RC circuit external to the chip. This pulse length then determines the delay seen from the negative-going edge of the output from the scanner and the output from the multivibrator, which is then passed through a 74HCT125 line buffer to the external trigger input of the accelerator. The RC value shown in Figure 5-2 provides for an edge delay of 1.04 ms, which matches the timing requirements of the shutter apparatus opening with a frequency of 25 Hz.

5.2 Instrumentation

Target Pressures

Pressures in the target system were monitored using a Varian DV100 Capacitance Manometer (p_0), two Balzers TPR 010 Pirani gauges (p_1 and p_2) and a Balzers

IKR 050 Cold Cathode gauge (p_3). The Balzers gauges were read with a Balzers TPG300 readout unit that was connected to a desktop computer which monitored the gauge pressures as a function of time. The DV100 output was remotely monitored using a voltmeter. The pressure in the gas plenum feeding the target was measured with a Wallace & Tiernan FA 223 Bourdon absolute pressure gauge, which was not remotely readable.

Neutron Yield

The neutrons produced by the gas target were monitored with a NRC NG-2A neutron-gamma survey meter from Nuclear Research Corporation, Warrington Pennsylvania (calibration date 23 September 1995). The dose meter was located 1.6 m from the beam stop, at an angle of approximately 5° from the deuteron beam.

Beam Current

The beam current was monitored by a Model 4688 toroidal transformer (from Pearson Electronics, Inc., Palo Alto California) located prior to the target system, on the end of the beam transport tube. This signal was amplified by a broadband amplifier. A number of measurements were performed without target gas to compare the measurements of this toroid to the measured charge collected on the isolated beam stop. The current was bled from the beam stop through a 100 Ω resistor. This calibration procedure indicated that the amplified toroid signal was equal to 2.3 ± 0.1 V per mA of beam current. It should be noted that the charge collected on the beam stop during operation of the gas target will not accurately reflect the incident beam current due to secondary ion and electron production as well as neutralization of the incident ions.

5.3 Predicted Yield

The yield of a thin deuterium gas target per unit deuteron current is

$$\frac{dY}{d\Omega}(\theta, E_d) = \frac{1}{e} \cdot \frac{d\sigma}{d\Omega}(\theta, E_d) t N \tag{5.1}$$

where e is the charge of an electron, t is the thickness of the target, and N is the atomic number density of the target material. Equation 5.1 assumes that the cross section $d\sigma/d\Omega$ is constant over the thickness t of the target. Targets in which $d\sigma/d\Omega$ is not adequately constant over t can be divided into appropriate segments and the resulting yields summed. The deuteron current is assumed to be constant over the full length of the target, as the cross sections are relatively small. The neutron yield $dY/d\Omega$, in neutrons per second per unit current per unit solid angle, can be converted into a fluence rate measurable at a detector location in the usual manner. In this case, the physical thickness of the target is relatively large when compared to the thickness when measured in terms of the deuteron energy loss, as well as the distance available to a useful detector location. Thus, the yields of the individual target segments described above must be weighted for their respective distances to the detector location, and not treated as a point source. If one defines the distance R as the distance between the beam stop and the detector location, then the fluence rate from the thin target is

$$\phi(\theta, E_d) = \sum_i \frac{1}{R_i^2} \frac{dY_i}{d\Omega}(\theta, E_d), \tag{5.2}$$

in neutrons per square centimeter per second per Ampere. The summation is carried out over all segments i such that the deuteron energy E_d lies between the incident energy E_i and the final energy E_f of the deuterons when they impact the beam stop.

The cross section for neutron production $d\sigma(E_d)d\Omega$ is taken from the computer code `WHIYIE` [2], which catalogs angle-dependent neutron yields from thick targets. This code does not include data for gas targets, but the microscopic cross section data are available as well. These data are summarized in Figure 5-3, scaled to fit the

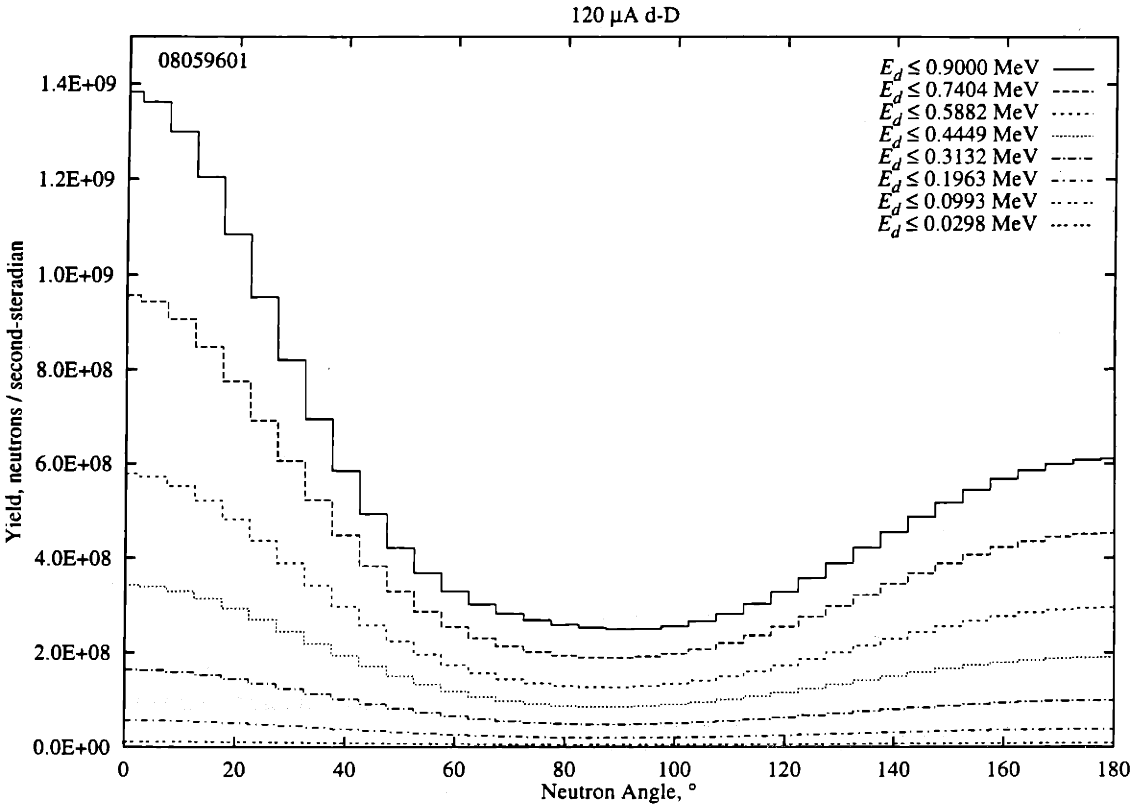

Figure 5-3: Neutron yield theoretically attainable from the DL-1 as a function of energy and angle.

maximum output of the DL-1 accelerator. The relevant values from Figure 5-3 are given numerically in Table 5.1.

Performing this calculation for a number of target pressures and a given target length (270 mm) at a given angle (5°) gives the neutron yields shown in Table 5.2. The thickness of the target in terms of deuteron energy (equal to the difference between the incident energy of $E_i = 900$ keV and the final energy E_f shown in Table 5.2) was calculated by means of TRIM [63], a Monte Carlo code for the transport of ions in matter. This code was also used to determine the lateral straggling of the beam as it traversed the length of the target, to assure that such straggling was negligible compared to the size of the beam spot. Such straggling was found to be less than 2% of the size of the beam spot.

Finally, the flux-to-dose conversion factor used in Table 5.2 is 1.50×10^{-4} rem/hr

E_d (kev)	$d\sigma/d\Omega$ (mb/ster)
900	2.5×10^1
817	2.3×10^1
736	2.1×10^1
657	1.9×10^1
581	1.7×10^1
506	1.5×10^1
434	1.3×10^1
366	1.1×10^1
300	8.8×10^0
239	6.8×10^0
183	5.0×10^0
131	3.3×10^0
87	1.7×10^0

Table 5.1: The differential cross section for the production of neutrons from d-D at 5° as a function of deuteron energy.

Pressure	E_f	Yield per μA	
(mbar)	(keV)	(n/cm^2·s)	(mrem/hr)
25	820	231	34.7
50	733	289	43.4
75	638	488	73.2

Table 5.2: Neutron fluence rates at detector located a distance 1.6 m from the gas target beam stop at an angle of 5° from the deuteron beam.

per n/cm^2·s.[64] This factor varies over the 2.8 to 4.0 MeV neutron energy range in question by less than 10%.

An uncertainty analysis of the terms in the summation in Equation 5.2 indicates that

$$\left(\frac{\varsigma_{\phi_i}}{\phi_i}\right)^2 = 4 \cdot \left(\frac{\varsigma_{R_i}}{R_i}\right)^2 + \left(\frac{\varsigma_{d\sigma_i/d\Omega}}{d\sigma_i/d\Omega}\right)^2 + \left(\frac{\varsigma_{t_i}}{t_i}\right)^2 + \left(\frac{\varsigma_{N_i}}{N_i}\right)^2 . \tag{5.3}$$

The uncertainty in R_i comes about from the size of the detector unit (approximately 300 mm long, as compared to a nominal distance of 1.6 m, for a relative uncertainty of 19%). The uncertainties in $d\sigma_i/d\Omega$, t_i, and N_i are due to the discretization process, which was selected such that there would be no more than a 5% error in any component. Thus

$$\left(\frac{\varsigma_{\phi_i}}{\phi_i}\right)^2 = 4 \cdot (0.19)^2 + (0.05)^2 + (0.05)^2 + (0.05)^2 = (0.38)^2 , \tag{5.4}$$

which is independent of i. The uncertainty in ϕ is then

$$(\varsigma_\phi)^2 = \sum_i (\varsigma_{\phi_i})^2 , \tag{5.5}$$

which is

$$(\varsigma_\phi)^2 = (0.38)^2 \cdot \sum_i (\phi_i)^2 . \tag{5.6}$$

For the 25, 50, and 75 mbar target yields shown in Table 5.2, the relative uncertainties are 30%, 21%, and 22%, respectively.

The numbers given in Table 5.2 must further be corrected by absorption in the beam stop and the target apparatus. The beam stop is 0.125" thick quartz, while the flange in which it is mounted is stainless steel approximately 0.50" thick. The total neutron cross section for either silicon or oxygen at 3.5–4.0 MeV is approximately 2 barns, which gives a macroscopic cross section of 0.21 cm^{-1}, for a transmission of 0.94. [65] The total neutron cross section for iron is approximately 3.5 b, which gives a macroscopic cross section of 0.30 cm^{-1}, for a transmission of 0.68. The diameter of the quartz viewport is such that the steel flange shadows approximately half of the detector, so the aggregate transmission can be approximated as (0.94+0.68)/2 = 0.81.

Pressure (mbar)	Yield (mrem/hr per μA) produced	transmitted
25	35 ± 10	28 ± 9
50	42 ± 9	35 ± 9
75	73 ± 16	59 ± 15

Table 5.3: Neutron fluence rates at detector located 1.60 m from the gas target beam stop and 5° away from the deuteron beam.

By inspection, the uncertainty in the cross section is approximately 0.5 barn. Thus, the relative uncertainties in ς_{ϕ} can be added in quadrature with $0.5/3.5 = 0.14$, with the results appearing in Table 5.3.

5.4 Static Target

After installation, the gas target was operated without the shutter apparatus installed, using helium gas. The shutter was then installed, and the target operated with the rotating shutter apparatus stationary, again using helium. The helium measurements confirmed the measurements previously described, and verified that the system was performing in a consistent manner. The gas system was then converted to deuterium and the target operated with the rotating shutter apparatus again stationary.

5.4.1 Gas Measurements

When operated in recirculating mode with deuterium gas, the gas target displayed the pressure profile describe in Table 5.4. The beam current for this test was an current of 0.280 mA averaged over the pulse of 40 μs at 100 Hz, for a time averaged current of 1.1 μA. As shown in Table 5.4, injection of the deuteron beam did not result in a significant change in the pressure profile of the target. At these beam currents, that is not particularly surprising.

This was the maximum pressure at which the static target could be operated, due to the flow rate in the second pumping stage, which resulted in the TMU 520 turbopump drawing the maximum current permissible.

Stage	Pressure (mbar)	
	without beam	with beam
Target	$2.0 \times 10^{+1}$	$2.0 \times 10^{+1}$
1	5.7×10^{-1}	5.3×10^{-1}
2	5.4×10^{-3}	6.7×10^{-3}
3	3.3×10^{-6}	3.1×10^{-6}

Table 5.4: Static gas target pressure profiles without beam and with a time-averaged current of (1.1 ± 0.1) μA.

5.4.2 Neutron Production

The neutron production from the gas target as operated in Table 5.4 was measured as previously described. When the beam was injected into the target without the target gas present, the dose meter indicated a neutron-only dose rate of (3.5 ± 0.1) mrem/hour. With target gas, the dose rate was measured to be (30 ± 0.1) mrem/hour, giving a yield (in the units adopted previously) of (24 ± 2) mrem/hour per μA, as compared to the predicted result of (28 ± 9) mrem/hour per μA.

5.5 Pulsed Target

The gas target was next operated with the shutter apparatus rotating. Experience in previous measurements described above indicated that the shutter apparatus would not operate reliably at speeds over 900 rpm (corresponding to a pulse rate of 30 Hz) at pressure differentials of more than 15 mbar. The shutter was therefor operated at a constant shaft speed of 750 rpm (25 Hz) for all pulsed tests. More stable operation yet is possible at even lower speeds, but the pulse length from the accelerator is limited to approximately 85 μs, even when the duty factor drops below the nominal 2% limit. Thus, at 25 Hz, the maximum duty factor available from the accelerator is 0.2%, which limits the neutron production rate. Using the dose meter described previously, these doses are near the limit of reliable sensitivity.

Stage	Pressure (mbar)	
	without beam	with beam
Target	$5.0 \times 10^{+1}$	$4.9 \times 10^{+1}$
1	3.8×10^{-1}	5.1×10^{-1}
2	$u.r \times 10^{-3}$	$u.r \times 10^{-3}$
3	7.7×10^{-7}	8.6×10^{-7}
Target	$7.3 \times 10^{+1}$	$7.5 \times 10^{+1}$
1	$1.0 \times 10^{+0}$	9.2×10^{-1}
2	$u.r \times 10^{-3}$	$u.r \times 10^{-3}$
3	1.1×10^{-6}	1.2×10^{-6}

Table 5.5: Pulsed gas target pressure profiles without and with beam. The time-averaged beam current was (200 ± 20) nA in either case.

5.5.1 Gas Measurements

The maximum pressure at which the target could be run before causing instabilities in the rotating shutter was 75 mbar. Pressure profiles and neutron yields were measured at 50 mbar and 75 mbar target pressures. The results of the gas measurements appear in Table 5.5. The pressures indicated for the second stage in either run are below the range of the Pirani gauge used on that stage.

As mentioned above, the limitation on the target pressure arose from the instability of rotating shutter, not from the pressures or flow rates for any of the pumps. In the higher pressure trial described in Table 5.5, the current drawn by the TMU 520 (which was the limiting factor for the static case) was 2.6 A; less than half the maximum current allowable. This would indicate that operation at three to four times this target pressure would be possible.

5.5.2 Neutron Production

The yield measured during the tests described in Table 5.5 was (33 ± 3) mrem/hr per μA for the 50 mbar target, and (40 ± 4) mrem/hr per μA for the 75 mbar target. These compare favorably to the predicted values of (35 ± 9) and (59 ± 15) mrem/hr per μA, respectively.

Target Pressure (mbar)	Rotating Shutter Operating	Predicted Yield	Measured Yield	Δ (%)	Limitation on higher pressure operation
		(mrem/hr per μA)			
25	No	28 ± 9	24 ± 2	-16	p_2
50	Yes	35 ± 9	33 ± 3	-6	n/a
75	Yes	59 ± 15	40 ± 4	-32	Shutter stability

Table 5.6: Summary of neutron production for a target length of 270 mm.

5.6 Summary of Operational Results

Table 5.6 summarizes the results of measurements of the operation of the gas target. These results indicate that the procedure used to predict the yield of the thin gas target was reasonable, and that the gas target was functioning in an appropriate manner. Measured neutron production was well within the bounds of uncertainty of the predictive calculations. This indicates that the beam was impinging the target as intended, and that the target material was uncontaminated by leakage into the gas recirculation system. Target behavior was as anticipated, and the pressure profile was as expected.

Chapter 6

Conclusions

6.1 Success of Original Goals

The original goal of this work was the construction of a windowless deuterium gas target of greater than 150 mbar operating pressure. This goal has been met with either the pulsed target system. For monoenergetic neutron production, this target can be operated at a pressure of approximately 250 mbar, and has been demonstrated on the DL-1 accelerator at pressures of 75 mbar. This is considerably greater than any windowless gas target actually demonstrated previously for such a large beam footprint. At 75 mbar target pressure, the target region is sufficiently compact to provide a well-collimated useful beam of neutrons with energies from 3.7–4.0 MeV. More optimal matching of the accelerator pulse characteristics and the rotating disk valve characteristics would allow the production of such neutrons with a fast neutron fluence rate of approximately 1.5×10^5 n/cm^2·s at a distance of one meter averaged over the 5° cone of forward emission (an area of 250 cm^2) for the maximum DL-1 current of 120 μA.

6.2 Scalability

This target is in no way limited to the present accelerator setup. In fact, this target is the basis for the design of similar targets being constructed or considered at cooperating facilities elsewhere. [66, 67]

6.3 Utility of Present Target

This gas target has conclusively demonstrated the value of restricting the gas flow through a differentially pumped aperture to only that portion of the duty cycle during which the aperture must be open. This target also provides a new capability for the DL-1 accelerator installed at MIT. This machine can now be used to produce useful fluxes of monoenergetic neutrons from 2–4 MeV for use in elementary substance identification and localization. It will permit the study of fast neutron radiography and prompt and inelastic gamma spectroscopy to reach levels of sophistication and specificity that were not possible with the previous target system.

6.4 Suggestions for Further Work

This target has an even greater value that in demonstrates a fundamental increase in the target density available from a windowless gas target. There are quite a number of ways in which the target could be further improved that would lead to even higher pressures and even greater flexibility. These include increasing the obtainable target density by

- cooling the target gas, resulting in greater density for an identical pressure,
- improving the design of the rotating valve assembly, decreasing the leakage through the gap between the rotor and the stator,
- implementing a method which would permit rotors at all three differentially pumped apertures (also a margin of safety issue),
- investigating methods of disrupting the influence of free-jet expansions on an aperture from apertures upstream.

There are questions which invite further study on the behavior of this sort of gas target. Namely, it would be worthwhile to explore the practical ramifications of high-current beam interaction with this sort of gas flow, and the modifications in such flows caused by high rates of power deposition. There are also questions of the exact mechanism of the impact the rotary valve has on the gas flow through the aperture. The hypothesis present previously, that the rotor was inducing turbulence in an otherwise laminar flow, could be tested by some means of flow visualization, or possibly by some other means of inducing turbulence in normally laminar flow.

Engineering improvements that would make the system more robust and flexible include

- redesigning the rotor system to give more rotational stability at greater pressure differences,
- redesigning the rotor system to smaller tolerances resulting in less gas leakage,
- redesigning the timing generator on the rotating valve to permit adaptive delays, thus requiring no operator intervention upon changing the pulse structure of the beam.

Specific examples of such improvements include replacing the shaft bearings with more robust designs, replacing the "soft" magnetic clutch motion feedthrough with a high-speed physical feedthrough such as those available from Ferrofluidics, and constructing a digital delay circuit which directly measures the time for which an aperture is open during a pulse and sets the delay for the next pulse equal to some appropriate fraction thereof.

6.5 Contributions of this Thesis

This thesis has demonstrated the operation of a windowless differentially pumped gas target at pressures twenty-five times greater than previously demonstrated for beams and apertures of similar size ($\approx$ 5 mm). This was possible by the development and implementation of a rotating disk valve which markedly reduced gas flow from one stage to the next, taking advantage of the low duty-factor existing in many types of commercially-available accelerators. Those parameters which were significant in the application of such a valve were identified for further study.

This thesis has further provided a valuable extension to the capability of the DL-1 neutron source facility on campus, permitting it to function as a source of monoenergetic neutrons for research into various methods of non-destructive testing.

Appendix A

Safety Analysis Report

As part of a number of ongoing projects, our research group is installing a DL-1 Neutron Generator made by AccSys Technology, Inc., Pleasanton, California. This device is installed in room NW13-038b, with the target assembly in room NW13-020. NW13-020 is a concrete vault with 32 inch walls. There are two beam ports in the walls, both fourteen inches in diameter. One of the ports opens into room NW13-038b, and one into NW13-038a.

A.1 Machine Description

The AccSys Model DL-1 Linac Neutron Generator system is a compact Radio Frequency Quadrupole (RFQ) linear accelerator (linac) that accelerates deuterium ions to an energy of 900 keV and bombards a beryllium target to produce neutrons. This final deuteron energy cannot be varied. The Model DL-1 Linac Neutron Generator was specifically designed as a replacement for the Kaman A-711 sealed neutron generator tube which utilizes the D(d,n) reaction. The pertinent operating parameters for the Model DL-1 are listed in Table A.1.

The Model DL-1 Linac Neutron Generator produces a positive ion beam by the ionization of deuterium gas in a duoplasmatron ion source. The ion source and the power supplies required to operate it are isolated at 25 kV. This voltage results in an ion beam being extracted from the plasma in the ion source anode and accelerated

Accelerated Particle	d^+	
Operating Frequency	425	MHz
Input ion energy	25	keV
Final ion energy	900	keV
Acceptance (normalized)	0.04	π cm-mrad
Current limit	21	mA
Final synchronous phase	-28.0	degrees
Average bore radius	1.60	mm
Maximum vane modulation	2.26	
Intervane voltage	45.0	kV
Maximum surface gradient	38	MV/m
Cavity RF power (w/o beam)	39.5	kW
Vane length	72.6	cm
Total length	1.016	m
RF drive loop	1 5/8"	coaxial
System weight	450	lbs
Vacuum pumps (2)	8"	cryopumps
Design input current	5–15	mA
Input emittance (normalized)	0.02	π cm-mrad
Beam transmission at 10 mA	> 90	%
Output energy spread (90%)	$< \pm 15$	kV
Beam pulse length	5–100	μsec
Cavity fill time	2	μsec
Pulse repetition rate (max)	640	Hz
Total RF power	48	kW
Maximum Duty Cycle	2.00	%

Table A.1: Model DL-1 System Specifications.

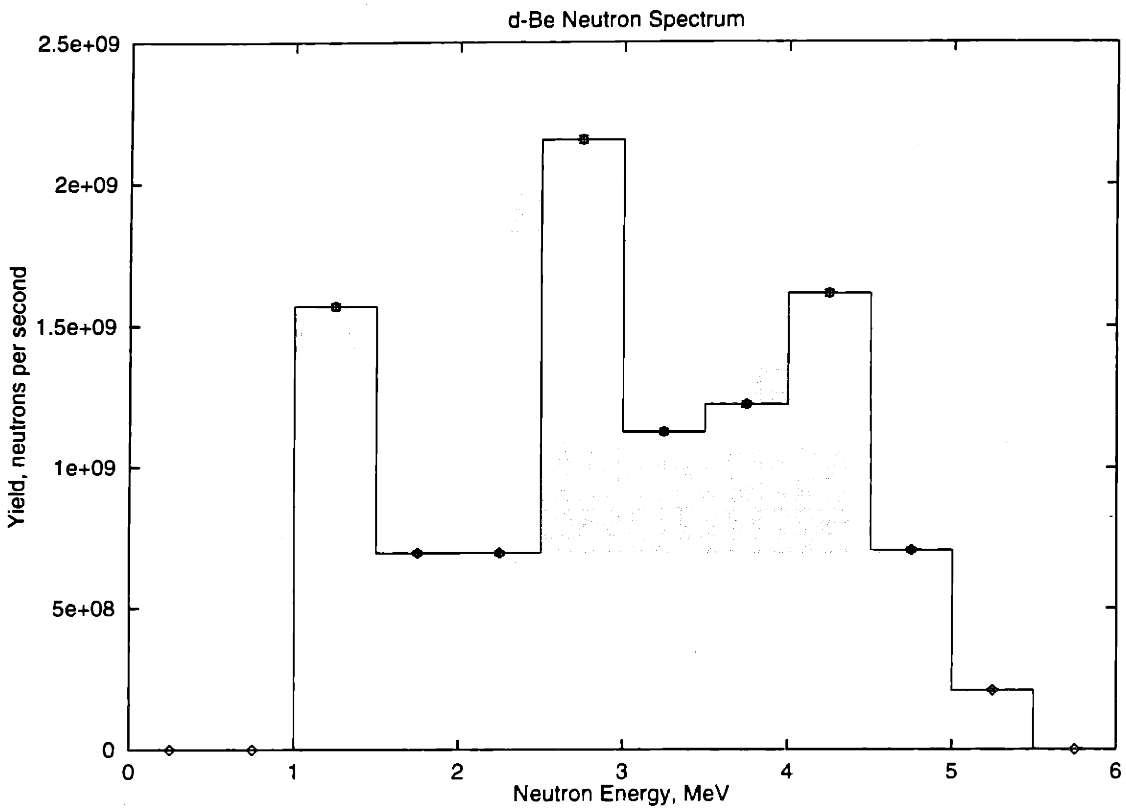

Figure A-1: Neutron source spectrum used in modeling 900 keV deuterons on beryllium. Normalized to a total yield of 10^{10} neutrons per second.

across the high voltage gap through the grounded extraction electrode. The extracted deuterium ion beam (80–90% d^+, 10–20% d_2^+) exits from the accelerating gap through an aperture in the extraction electrode and is measured in a beam current toroid before being focused into the RFQ linac by an electrostatic einzel lens.

This source is designed to produce 10^{10} neutrons per second, with the source spectrum appearing in Figure A-1. [68] The control system is software interlocked to prevent operation at greater than 2.0% duty factor, and the RF power system is physically unable to provide more than 2.25% duty factor. The design filament and target are unable to handle greater than 10 mA of (peak) current. The figure of 10^{10} neutrons per second is based on 120 μA of beam current (time-averaged). Until we have verified the dose predictions below, the source will not be run over 10% of full current.

A.2 Use of Facility

This facility will be used for:

- research into fast and thermal neutron radiography of industrial components,
- fast neutron-prompt gamma analysis related to the detection of contraband,
- measurements related to the source reactions, both neutron and gamma.
- time-of-flight experiments with thermal neutrons.

A.3 Floor Plan

The floor plan of the area appears in Figure A-2. This shows the accelerator room (038b), the control room (039), and the vault area (020), as well as the surrounding rooms and hallways. The walls shown as solid are new, as part of the renovations. The walls shown in outline are pre-existing construction. The shield wall around the accelerator in room 038b is solid concrete block, a minimum of 24 inches thick, or an equivalent or greater hydrogen thickness of water in polyethylene tanks. The entire area past the doors marked "3" and "5" is accessible only through those doors. These doors and all interior doors will be part of the interlock system described below.

A.4 Potential Hazards

The potential hazards involved in the operation of this machine include high voltage (25 kV), explosive gas (deuterium) and both neutron and gamma radiation.

The high voltage is contained within lockable electrical cabinets in room 133a, the ion source in room 038b, and the cables between them. Both the electrical cabinets and the ion source are shielded with lucite panels, connected to an electrical system interlock that activates a mechanical crowbar, shorting out the high voltage. The deuterium gas bottle and system are contained in the same shielded areas, and are at very low pressures. The interlock systems on this commercial device are intended to

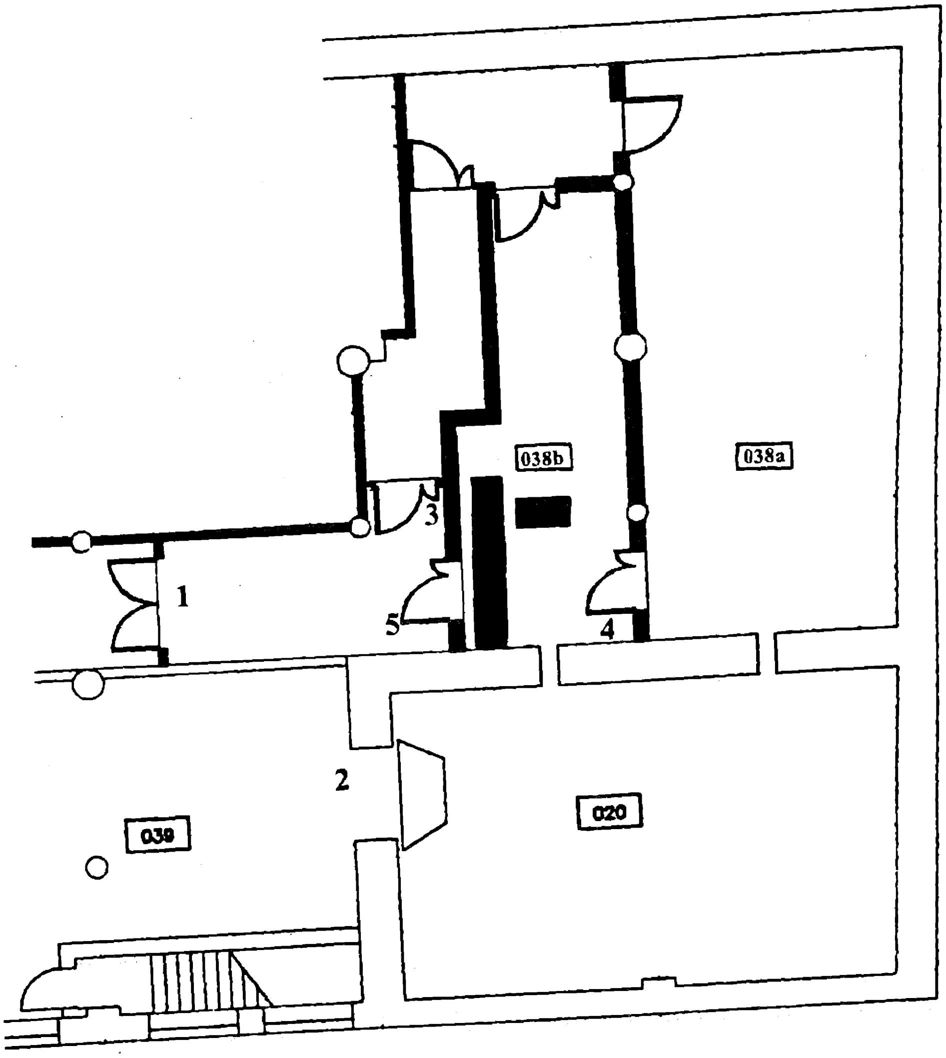

Figure A-2: Floor plan of accelerator area.

prevent safety hazards due to high voltage and explosive gas. The mixed radiation field from the accelerator is discussed below.

A.5 Radiation Shielding

The neutron source is located just inside the concrete wall of the vault, centered on the hole bored through the wall for the end of the accelerator. The hole is fourteen inches in diameter, and is filled with polyethylene around the beam line. The target is surrounded by 30 cm of polyethylene within the vault. The shield wall behind the accelerator is floor-to-ceiling solid concrete block at least 32 inches thick, or the hydrogen equivalent in water. The primary areas (see Figure A-2) of concern for dose calculations are as follows:

- Corridor doors (5 and 3). These doors are interlocked into the control system, and the area past them will be inaccessible while the neutron source is enabled. These doors (5 and 3) will be considered the boundary of the publicly accessible area.

- Vault door (2). This is the massive concrete block that closes off the vault (020) from the control room (039). Room 039 will be accessible only to operators and experimenters during operation of the neutron source. The vault door is also interlocked into the control system.

- First floor laboratory. The area immediately above rooms 039, 038a and 38b is a classroom/laboratory space, NW13-133 and NW13-133a. The top of the vault extends approximately six feet in height into the southeast corner of this area. The electronics for the DL-1 accelerator are set up in room 133a, and several cables penetrate the floor into room 038b. The area (which will be referred to as area 14) immediately over these holes is covered with additional concrete block. Other than this area, the room is completely shielded by the walls of the vault. This area will be considered accessible by the public. The area on top of the vault will be referred to as area 30.

- NW13 exterior wall (12, not shown). The south wall of the concrete vault is also the exterior wall of building NW13. The area to the south of the building is publicly accessible, although on the railroad right-of-way.

A.6 Estimated Dose Rates

The RFQ device itself produces 25 keV (maximum) x-rays from its vanes. During operation of the RFQ, these x-rays lead to a dose rate of about 100 mrem/hour at the surface of the RFQ chamber. This is an experimental measurement, taken by the manufacturer. These x-rays are shielded with eighth-inch lead sheet draped around the RFQ tank. The attenuation coefficient of lead for 100 keV x-rays is 5.29 cm^2/g. [69] The attenuation of the x-ray field by the (0.32 cm) lead sheet is then conservatively estimated to be

$$\frac{I}{I_0} = e^{-\frac{\mu}{\rho}\rho t} = e^{-5.29 \cdot 11.34 \cdot 0.32} = e^{-19} = 5 \times 10^{-9}.$$

The uncollided dose outside the lead is then miniscule, some 5×10^{-7} mrem per hour. The buildup factor is conservatively estimated to be 2.75 (this is for 500 keV, $\mu t = 20$, lead). [70] This still leaves the x-ray dose on the outside of the lead sheet on the order of nanorem per hour.

The d-Be reaction produces approximately 3×10^{-5} photons per deuteron, with a maximum energy of 3.4 MeV. [71] The yield of the various photons and their energies appears in Table A.2. We assume that there is a minimum chord length of 81 cm (32 inches) of concrete between the target and any area of concern. This gives a total dose rate of 0.84 mrem/hour at one meter. The dose rates at various locations due to the direct photons are estimated from that number, reduced by geometric attenuation.

The dose rates at various locations due to neutrons and induced photons were estimated by Monte Carlo analysis using the code MCNP. [72] The walls were modeled as ordinary concrete, with a density of 2.35 g/cm^3. The source neutron distribu-

Energy (MeV)	Yield per deuteron	μ/ρ (cm^2/g)	rem/hr per γ/cm^2·sec	Buildup Factor	Dose Rate (mrem/hour)
0.413	1.2×10^{-6}	0.0943	9.9×10^{-7}	81.05	1.4×10^{-5}
0.717	13.7×10^{-6}	0.0747	1.6×10^{-6}	44.67	6.1×10^{-3}
1.022	3.9×10^{-6}	0.0629	2.0×10^{-6}	22.29	1.0×10^{-2}
1.433	2.5×10^{-6}	0.0530	2.6×10^{-6}	14.04	3.6×10^{-2}
2.151	1.2×10^{-6}	0.0433	3.4×10^{-6}	7.55	7.8×10^{-2}
2.871	2.4×10^{-6}	0.0374	4.1×10^{-6}	5.34	4.1×10^{-1}
3.580	0.9×10^{-6}	0.0336	4.8×10^{-6}	4.26	3.0×10^{-1}

Table A.2: Dose rates at one meter due to photons coming from target. These figures assume a minimum of 81 cm (32 inches) of concrete. The total dose rate at one meter is 0.84 mrem/hour.

Area	Neutron	Induced γ	Direct γ	Total
2	0.14 ± 15%	0.28 ± 3%	0.03	0.45 ± 0.02
5	0.09 ± 26%	0.04 ± 11%	0.11	0.24 ± 0.02
12	0.28 ± 13%	0.08 ± 6%	0.01	0.37 ± 0.04
14	0.11 ± 14%	0.05 ± 8%	0.09	0.25 ± 0.01
30	0.27 ± 12%	0.10 ± 6%	0.02	0.39 ± 0.04

Table A.3: The estimated dose rates (in mrem/hour) at various locations around the facility at 100% strength. The uncertainties quoted are $1 \cdot \sigma$, and are the precisions associated with the Monte Carlo estimates.

tion used is given in Figure A-1. The flux-to-dose conversion factors used are from ANSI/ANS-6.1.1-1977.

As these calculations are very time-consuming, a subset of the above locations were chosen as bounding values. Area 5 was chosen as a bounding value for areas 1 and 3. Area 12 was chosen as a bounding value for any area outside building NW13. Area 30 was chosen as a bounding value for any surface of the vault with the exception of area 14, which is near the source itself and the beam port.

The Monte Carlo results are such that the dose estimates cannot be considered fully converged—i.e., such that distribution of contributions follows a normal distribution, and one can safely expect that the actual expectation value of that quantity is within $1 \cdot \sigma$ of the quoted result. The unconverged values (i.e., those with precisions poorer than 5%) are likely to be within a factor of a few of the true value, but cannot be considered to be properly converged and are therefore not completely reliable. The behavior of the results indicate that the important phase space regions of the problem were in fact well sampled, but that insufficient particle histories were simulated to allow for more reliable figures.

A.7 Interlock System

The interlock system is designed to prevent access by anyone (including users) to areas subject to radiation doses above 5 mrem/hour. The interlock system prevents the application of RF power to the RFQ unless the doors to all interlocked areas are closed and secure. This prevents both neutron production from the target and x-ray production from the vanes of the RFQ tank. The system is fail-safe, and works by non-powered magnetic proximity switches on all doors. The interlock system requires searches of all radiation areas, and and a key to enable the accelerator. The interlock system also stops the beam if the doors to any radiation area are opened while the beam is enabled. If this happens, the interlock system must be reinitialized. The door to the vault area is interlocked at a different level than are the doors to the accelerator area. The vault can therefore be opened and closed without repeating the search of the accelerator rooms.

The interlock system includes an Emergency Off switch, a Search switch, and a Warning light in room 038a, in room 038b, in each of the three corridor segments, in the vault (020), and in the control room (039). The system also includes proximity switches on each door within the above areas, and is controlled from a panel in room 039.

The interlock system operates at four levels.

1. DISABLED. This level allows complete access to all rooms in the accelerator area and the vault. No radiation-producing equipment can be activated. This is the beginning state of the system. The system will return to this state upon the opening of any interlocked door except the door to the vault area. The

interlock system will also return to this level if any Emergency Off switch is activated.

2. SEARCH. This level can be reached from the first level by closing a key-switch on the control panel. This level is indicated by a Warning light in the control room. This switch also activates the Warning lights in the accelerator rooms (038a and 038b) and corridors. The interlock system then requires the operator to search through each of the accelerator rooms and the corridors, in order, closing momentary switches. One of these switches requires the same key as does the key-switch on the control panel. The key must be removed from the control panel during the search process. The key-switch in the interlocked area must be momentarily moved to a position that does not allow the key to be removed from it, and then returned to the original position that does allow removal to complete the search process. This key is then returned to the control panel when the search is completed. The key-switch on the control panel bypasses the door switches, allowing the search to take place. Once the search is completed, the key-switch can be turned away from the search setting, so that it no longer bypasses the door switches.

3. ACCELERATOR SECURE. This level is indicated by a green light on the control panel, which verifies that the search process was satisfactorily completed and the doors to the accelerator areas are shut. Any of these doors opening will reset the interlock system back to the first level. This level is reached by completing the search process, and leaving all doors to the accelerator area closed.

4. VAULT SECURE. This level is indicated by a yellow light on the control panel. It can be reached only by completing the search process (reaching the previous level), returning the key to the control panel, turning the key-switch on the control panel to a position that does not permit removal, and closing the vault door. Opening the vault door or removing the key from the key-switch will return the interlock system to the Accelerator Secure level (green light), not requiring a further search of the accelerator rooms.

5. ENABLED. This level is indicated by a red light on the control panel. It can be reached by closing a momentary contact on the control panel when the system is in the Vault Secure state (yellow light). The system can be returned to the Search level (green light) by opening the key-switch on the control panel. When the interlock system is in the Enabled state, a switch on the frequency controller for the RFQ system can be closed, activating the neutron source. This switch has no effect on anything if the interlock system is not Enabled.

A.8 Operational Procedure

The operation procedure requires the search of all radiation areas before the machine is activated. The user areas will be surveyed with a Model NG-2 Snoopy neutron/gamma monitor when the machine is first turned on, and every time the system or its operating parameters are changed. The results of these surveys will be recorded in the logbook. The areas to be surveyed are areas 2 and 5, as marked in Figure A-2, and at the surface of the cave in room 133b (area 14). The machine will not be left unattended in such a state that it can be turned on. The opening of any doors into radiation areas will cause the machine to shut down, and require all areas to be re-searched. A log book will be used to record the actual amount of beam on target and the pulse repetition rate, which can be used to obtain the maximum possible total neutron production over any given time. As the target surface conditions can degrade the source output considerably, a more accurate monitoring system will be obtained.

All users will wear radiation badges (both neutron and gamma) provided by the Radiation Protection Office. These badges will be monitored monthly. Similar badges will be positioned at various locations around the facility as area monitors. Surveys will be done (using the above-mentioned Snoopy detector) of the vault and equipment therein when the vault is opened after the neutron source has been operating.

The interlock system will be tested every time it is modified, and either monthly or upon every use, which ever is less frequent.

A.9 Usage Factor

It is estimated that the facility will operate at no more than 72 mA-hours (600 full-strength hours) per year. This should result in the maximum annual dose in any public area being less than 250 mrem, one half the limits required by the guidelines of the Radiation Protection Office for a non-controlled area. [27]

A.10 Credible Accidents

A worker in the interlocked area could somehow not notice the search procedure, and not be noticed by the worker conducting the search. If someone found themselves in such a position, they would either hit an Emergency Off button, or open any door within the area, and the beam would be shut off. The interlock system would not permit the beam to be restarted until a new search takes place.

Some section of shielding could be removed. If this were to happen, it would be noticed both during the search procedure, and during the survey of the area after the machine is started up.

The interlock system could fail by a door switch being destroyed or removed. As these switches are normally open, this would not allow the search to be completed.

The interlock system could fail by an Emergency Off switch not opening. If this were to happen, the doors in the interlocked area will still function as beam kill switches.

A.11 Interlock Diagram

A circuit diagram of the interlock system appears in Figure A-3.

A.12 Interlock Procedure

1. Visually check rooms NW13-038a and NW13-038b to insure that nobody is in these rooms before beginning the interlock procedure. This is a courtesy

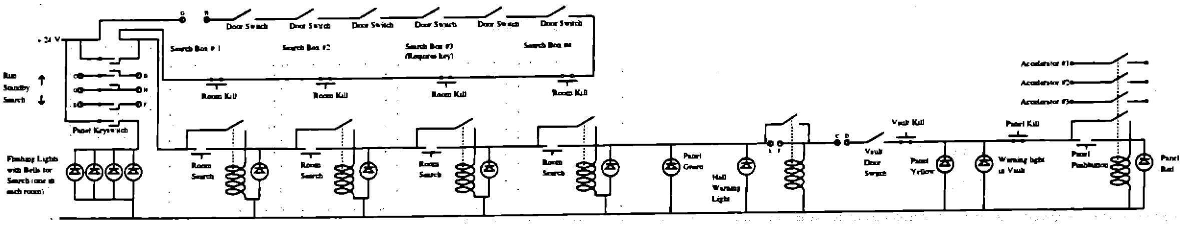

Figure A-3: Circuit diagram for Safety Interlock system of the DL-1 Neutron Source Facility.

measure to prevent accidentally turning the loud alarm bells on while people are in these rooms.

2. Begin the interlock procedure by turning the key in the control box counterclockwise. This will cause alarm bells to start ringing in the search area. Remove the key while it is in the counterclockwise position, as it is required to complete the search procedure.

3. Begin the search procedure. Visually inspect the corridor between NW13-039 and -038b, making sure it is clear of hazards and people. If the space is clear, press the green button under the bell. The yellow light should come on.

4. Enter NW13-038b and visually inspect the room, making sure to check behind any shielding for hazards and people. If the space is clear, press the green button on the interlock box. The green light should come on.

5. Exit NW13-038b and close the door to NW13-038b. Visually inspect the small area outside of NW13-038a and -038b for hazards and people. If the space is clear, place the interlock key in the interlock box and turn clockwise. The red light should come on.

6. Enter NW13-038a and visually inspect the room. If the space is clear of hazards and people, press the green button on the interlock box. The green light should come on.

7. Return to the control room (NW13-039), closing all doors behind you. The large red strobe light in the corridor between NW13-039 and -038b should be blinking and the green light on the interlock control box should be on, indicating that all four inspection switches have been closed in order and all doors are shut. If the green light is not on, the switches were either closed out of order, a switch was missed, or a door was not closed tightly.

8. Place the interlock key in the interlock control box and turn the key one step clockwise (to the six o'clock position.) The bells should stop ringing and the green light should stay lit.

9. Inspect the vault for hazards or people.

10. Close the vault.

11. Turn the key in the interlock control box one more position clockwise. The yellow light on the interlock control box should come on, indicating the vault door is closed.

12. Press the green button on the interlock control box to allow RF power to be applied to the cavity. The red strobe light above the computer control console should start flashing.

A.13 Emergency Shut Off Procedure

If the system must be shut down for any emergency, the following methods may be applied:

- Press the kill switch in any of the search areas. The kill switches are red buttons and are located next to each of the four search switches.

- Press the kill switch in the vault. This switch is located on the wall of the vault next to the door, on the left. This switch can only be reset with a key.

- Press the kill switch on the interlock control panel. This switch is a large red button.
- Open any door in the interlocked area. This includes the vault door and any door between the control room (NW13-039) and either accelerator room (NW13-038a and -038b) except the large double doors just outside of the control room. Opening any of these doors will break the interlock system and shut down the RF power.
- Turn the interlock key in the interlock control box counterclockwise.

A.14 Measurements for d-Be neutrons

On September 27, 1995, the DL-1 Neutron Source Facility was operated at 61 μA, in accordance with the decision of the Radiation Protection Committee at the meeting held September 12, 1995. A survey was performed with the NRC NG-2 Snoopy detector to determine relevant dose rates for comparison to values predicted in the Safety Report. These measurements are reported in Table A.4. All dose rates are given in mrem/hour. As pointed out previously, the precisions given by MCNP are such that one would expect the calculated values to be within a factor of two or three of the true values, rather than being distributed about the true value with a standard deviation equal to the reported precision. The estimated values appear to

Area	Predicted Neutron	Actual Neutron	Predicted γ	Actual γ	Predicted Total	Actual Total
2	0.07 ± 0.01	0.08	0.16 ± 0.01	0.10	0.23 ± 0.01	0.18
5	0.05 ± 0.01	0.04	0.08 ± 0.01	0.04	0.12 ± 0.01	0.08
12	0.14 ± 0.02	0.03	0.05 ± 0.01	0.05	0.19 ± 0.02	0.08
14	0.06 ± 0.01	0.08	0.07 ± 0.01	0.04	0.13 ± 0.01	0.12
30	0.14 ± 0.02	0.09	0.06 ± 0.01	0.06	0.20 ± 0.02	0.15

Table A.4: Comparison of measured and predicted dose rates around the DL-1 d-Be neutron source facility.

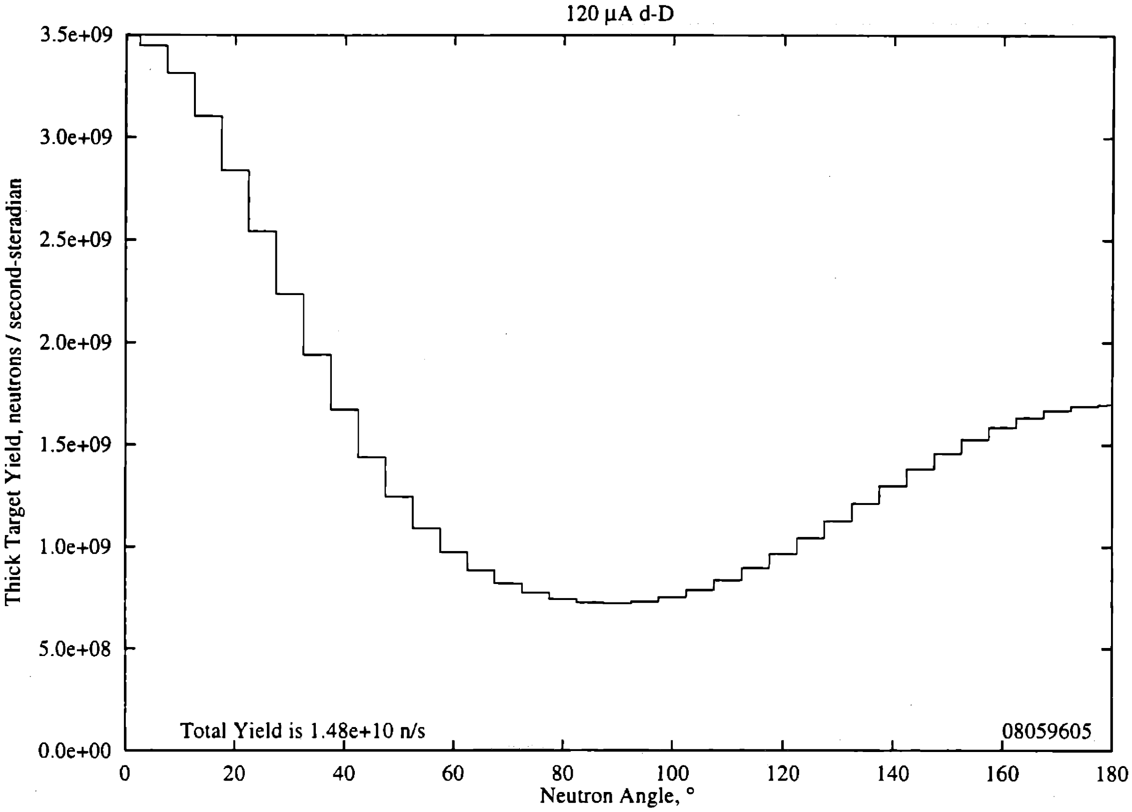

Figure A-4: Thick target d-D yield for DL-1.

be within that factor of two or three, and those which have the most disparity err on the conservative side.

A.15 Modification for d-D neutrons

The calculations for the deuterium gas target were done in a similar fashion with MCNP. The d-D reaction has a somewhat more simple spectrum than does the d-Be reaction. The thick target yield for the d-D reaction with 900 keV incident deuterons is shown in Figure A-4. The average neutron energy from this thick target yield is 2.71 MeV, while the maximum neutron energy is 4 MeV. When compared with the d-Be reaction, which has an average energy of 2.75 MeV and a maximum energy of 6 MeV (in the spectrum used in our calculations), one would expect a decrease in the dose rates due to the softer spectrum. In fact, this shift in spectrum reduces the dose

	d-Be, 120 μA			d-D, 120 μA		
	Neutron	γ	Total	Neutron	γ	Total
2	0.14 ± 0.02	0.31 ± 0.01	0.45 ± 0.02	0.14 ± 0.01	0.42 ± 0.02	0.57 ± 0.02
5	0.09 ± 0.02	0.15 ± 0.01	0.24 ± 0.02	0.02 ± 0.01	0.04 ± 0.01	0.07 ± 0.01
12	0.28 ± 0.04	0.09 ± 0.01	0.37 ± 0.04	0.41 ± 0.08	0.13 ± 0.01	0.54 ± 0.08
14	0.11 ± 0.02	0.14 ± 0.01	0.25 ± 0.01	0.11 ± 0.02	0.08 ± 0.01	0.18 ± 0.02
30	0.27 ± 0.03	0.12 ± 0.01	0.39 ± 0.02	0.17 ± 0.02	0.14 ± 0.01	0.31 ± 0.02

Table A.5: Comparison of dose rate predictions for d-D as compared to d-Be sources.

rate more than enough to compensate for the 48% greater neutron yield.

Table A.5 compares the predicted dose rate estimates for the two targets. A little arithmetic will show that the average change in the dose rate due to the change in neutron spectrum is a decrease of 9%. Note that this does not include the reductions expected for the change in the position of the source. When this 20% decrease is added as well, one can estimate a reduction in dose rates (in areas accessible to workers) of approximately 30%, as shown in the memorandum to the Radiation Protection Office dated 22 July 1996.

A.16 Tritium Production

A d-D yield of 1×10^9 neutrons per second will result in the production of less than 50 pCi/s of tritium from the accompanying D(d,p)T reaction. Were this quantity of tritium to be collected in the volume of air present in the vault over an eight hour period, assuming no outside ventilation (which is not the case), this would result in a concentration of $7.2 \times 10^{-12} \mu\mathrm{Ci/cm}^3$. This concentration is 1.4×10^{-3} of the maximum permissible concentration of airborne tritium for occupational exposure, and 3.6×10^{-3} of the maximum permissible concentration for public exposure. [69]

A.17 d-D Neutron Production in the Beamline

The d-D production within the beamline of the target will be directly proportion to the pressure. Thus, less than one part per thousand of the neutron yield will be coming from within the beamline portion of the target system, This portion of the target system is also within the vault proper, and is thus shielded to the same extent as the target itself.

Appendix B

Beam Optics

A significant consideration in the design of a differentially pumped target system for high current beams involves the optics of the charged particle beam. Such beams will begin to diverge at some distance from the output of the accelerator which produces them, and will rapidly become larger than the apertures through which the beam must travel. The beam from the DL-1 accelerator diverges to a beamspot of 50 mm diameter after approximately 600 mm travel—the location of the beginning of the differentially pumped apertures. The beamspot at the location of the target region itself is some 100 mm in diameter, as can be seen in Figure B-1, the origins of which are explained below.

A High Energy Beam Transport (HEBT) system is required to focus the beam in such a way that it will travel through the aperture system without excessive losses. Of course, the focusing system which does this also minimizes the size of the beamspot at the target. This small spot size is very beneficial for many applications.

To function best with a set of differentially pumped apertures, a beam should be focused to a minimum within the bounds of the system. This would indicate a "waist" in the particle beam, of footprint smaller than the size of the apertures. Centering this waist along the length of the series of apertures results in the narrowest point of the beam typically being at or near the center aperture. The beam then expands to the location of the first aperture, which defines the target region. This results in an inefficient target—the most important quantity determining the nature of the

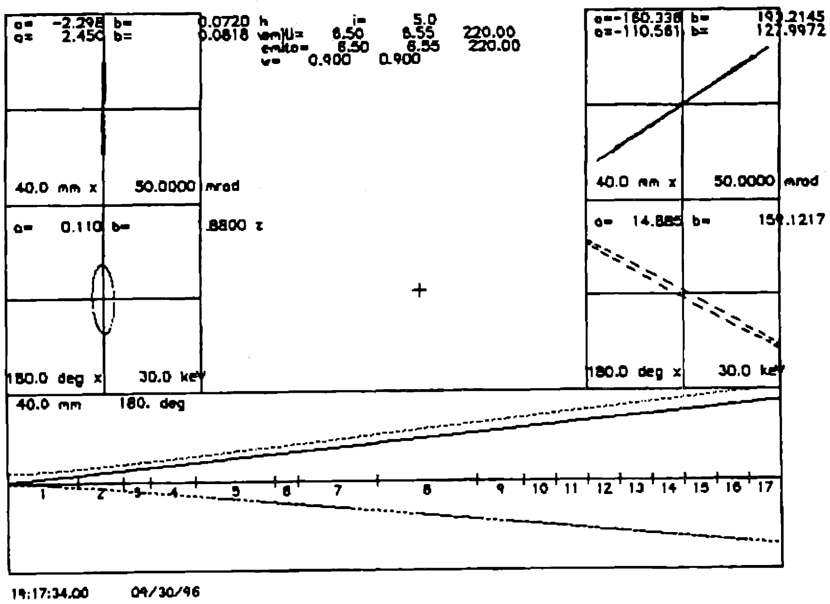

Figure B-1: The deuteron beam without focusing. The position of the differentially pumped target system is forced (by the wall of the vault) to begin at the right edge of region "10."

target system is the flow of gas though the target aperture. This flow is very strongly dependent upon the diameter of the aperture. Thus it is most advantageous to focus the beamspot on the plane of the target itself, providing that the nature of the beam (especially the space charge) so permits.

B.1 Theory

A bunched charged particle beam traveling through a beam transport system can be characterized by a beam envelope. This envelope is a hyperellipsoid in six-dimensional phase space. The dimensions in question are the transverse extent of the envelope (x and y), the angular divergence of the envelope (x' and y'), the longitudinal extent of the envelope (z), and the rate of change in the longitudinal extent of the envelope ($\Delta p/p$). The projection of the hyperellipsoid on any two-dimensional plane is the ellipse which defines the boundary of the beam in that plane. The hyperellipsoid is defined by a 6×6 matrix, and the projections of the hyperellipsoid onto the transverse and longitudinal phase planes provide six parameters, often called the Twiss parameters. These parameters are used with the emittances of the beam to follow said beam through various elements in the beam transport system by a sequence of matrix transformations.

In this case, these calculations were performed using the code TRACE 3-D. [73] From the manual for TRACE 3-D;

> TRACE 3-D is an interactive beam-dynamics program that calculates the envelopes of a bunched beam, including linear space-charge forces, through a user-defined transport system. TRACE 3-D provides an immediate graphics display of the envelopes and the phase-space ellipses and allows nine types of beam-matching options.

The method of matching a given beam (in this case the beam from the DL-1 accelerator) to the desired target system is as follows.

1. The diameter of the target aperture is specified. This specifies the maximum

transverse extent of the beam allowed at the location of the aperture, thus fixing two of the six Twiss parameters.

2. The diameter of the aperture at the low-pressure end of the target system is specified. This determines the maximum transverse extent of the beam at this location, fixing two more parameters.

3. The maximum transverse extents of the beam at any other location along the beamline uniquely determines the beam envelope, and thus the beam emittances. Thus, the emittances of the existing DL-1 beam were used to fix the remaining two Twiss parameters.

In the TRACE 3-D parlance, this is done by using the "l" option, which determines the emittance ellipses from three profile measurements. Two of the three profile measurements are fixed as the aperture sizes, and the remaining profile measurement is varied until the calculated emittance ellipses match those of the actual beam.

The above procedure results in the beam being optimally matched to the aperture system. In order to obtain that beam from the existing beam, the parameters characterizing the focusing system are varied until the desired Twiss parameters are matched. As there are six Twiss parameters which must (nominally) be determined, all six of the HEBT parameters are varied (using TRACE 3-D's matching facility—the "m" option) until the resulting beam most closely matches the desired parameters. This is a non-linear optimization process, and repeated iteration between the "l" option and the "m" option is necessary. To link the two iteration processes, the "profile measurement" at the lowest-pressure aperture (used by the "l" option) is modified to be more like the footprint predicted at that same location by the calculated HEBT system. Iterating in this fashion allows one to arrive at a HEBT system which will focus the beam through an acceptable aperture system.

B.2 Results

The procedure described in the previous section was followed to calculate the necessary features of the HEBT system. Because of the pre-determined energy of the beam produced by the RFQ accelerator, and the space constraints placed on the HEBT system, it was determined that the most desirable focusing system was three Permanent Magnet Quadrupoles (PMQs). These magnets will not require any power supplies or external cooling. If necessary during operation, the magnets can be heated or cooled somewhat to change their coercivity, which will consequently change the field gradient. However, it is envisioned that such changes will not as a rule be necessary, and that any change in the day-to-day requirements on the HEBT system can be effected by changing the spacing of the magnets. In order to calculate the effect on the beam envelopes of a PMQ, TRACE 3-D requires the length, field gradient, and inner and outer radii of the PMQ as input. In order to make the calculation process match the use of the magnets most closely, the spacing of the magnets and the field gradients were the six parameters used in the iteration procedure. The lengths and outer radius of the magnets were chosen to match some stock magnets available from the chosen manufacturer, Aster Enterprises, Inc., North Billerica, Massachusetts, and the choice of desired field gradient determined the inner radius to which the individual magnet needed to be machined. This use of stock magnets resulted in a delivery time and cost considerably more attractive than the construction of custom magnets.

The HEBT system chosen is described in Table B.1. The lengths of the drift spaces denoted as regions 7–9 were inversely coupled to the lengths of the drift spaces denoted 1, 3, and 5, respectively. This allowed the total length of regions 1–9 to remain constant. The beam envelopes produced by this HEBT system are shown in Figure B-2 and Figure B-3.

The iterative procedure was repeated until a HEBT system that was relatively insensitive to the space charge effects of the beam was determined. Figure B-4 shows the envelopes of the beam at several different values of the peak beam current bracketing the range of currents the DL-1 can reasonably produce.

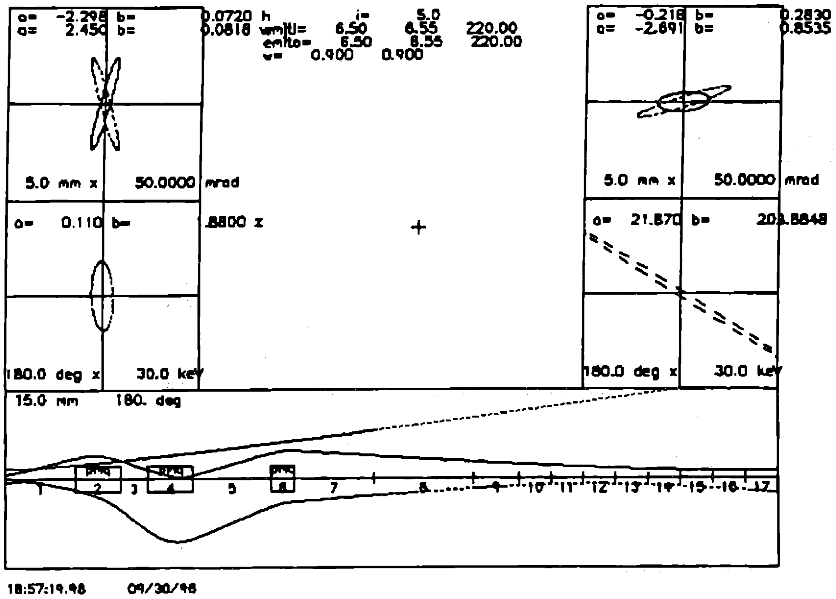

Figure B-2: The transverse half-widths of the deuteron beam through the design HEBT system.

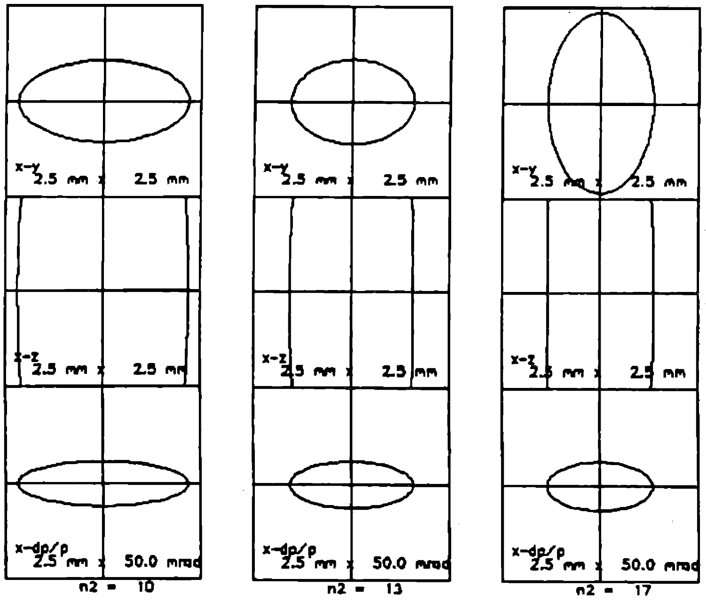

Figure B-3: The profiles of the deuteron beam at various locations within the design HEBT system.

Region	Element	Length (mm)	Gradient (T/m)	r_i (mm)	r_o (mm)
1	Drift	107.5	—	—	—
2	PMQ	70.0	49.5	15.6	26.7
3	Drift	43.6	—	—	—
4	PMQ	70.0	-35.2	17.8	26.7
5	Drift	122.2	—	—	—
6	PMQ	35.0	46.3	16.0	26.7
7	Drift	124.5	—	—	—
8	Drift	153.4	—	—	—
9	Drift	73.8	—	—	—

Table B.1: Design HEBT system parameters.

As delivered, the magnets had the parameters indicated in Table B.2 Repeating the beam matching procedure in TRACE 3-D using these PMQ parameters, and only allowing the magnet spacing to vary resulted in the drift space lengths also shown in Table B.2, and the beam envelopes shown in Figure B-5 and Figure B-6.

Region	Element	Length (mm)	Gradient (T/m)	r_i (mm)	r_o (mm)
1	Drift	107.5	—	—	—
2	PMQ	70.0	52.4	15.5	26.7
3	Drift	40.0	—	—	—
4	PMQ	70.0	-36.7	17.7	26.7
5	Drift	110.0	—	—	—
6	PMQ	35.0	48.1	16.0	26.7
7	Drift	124.5	—	—	—
8	Drift	157.0	—	—	—
9	Drift	76.0	—	—	—

Table B.2: Delivered PMQ parameters and resulting drift spaces.

It is worth noting that the footprint of the beam from the revised HEBT system is actually slightly more favorable than that from the original HEBT system.

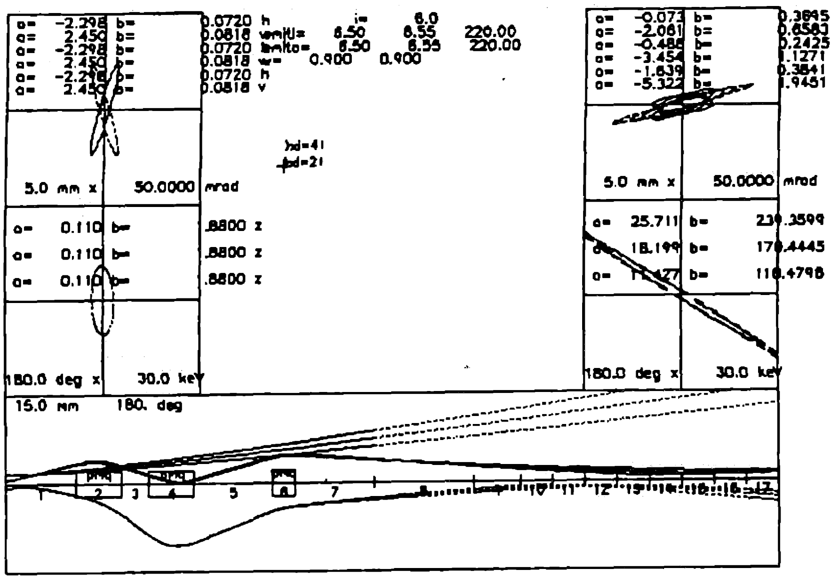

23:04:39.91 09/30/98

Figure B-4: The effect on the beam envelopes of varying the peak beam current.

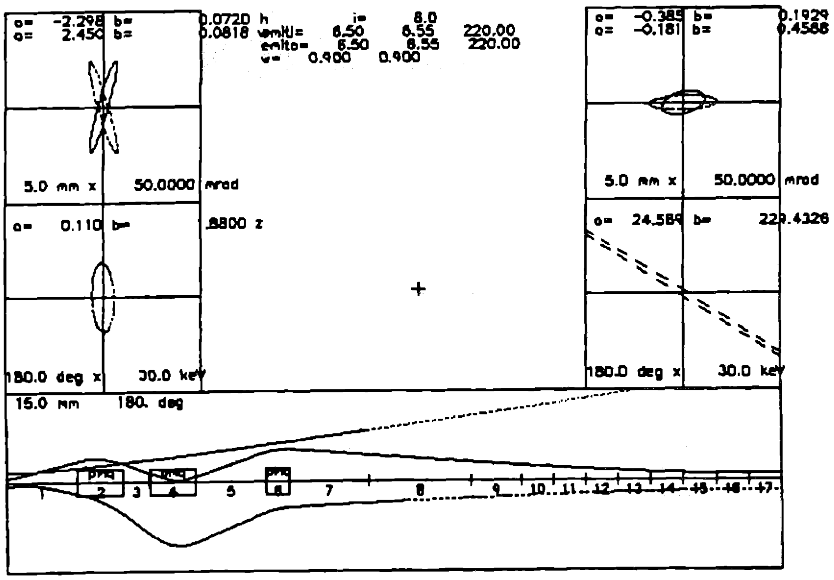

23:06:43.11 09/30/98

Figure B-5: Beam envelopes for revised HEBT system design based upon delivered PMQs.

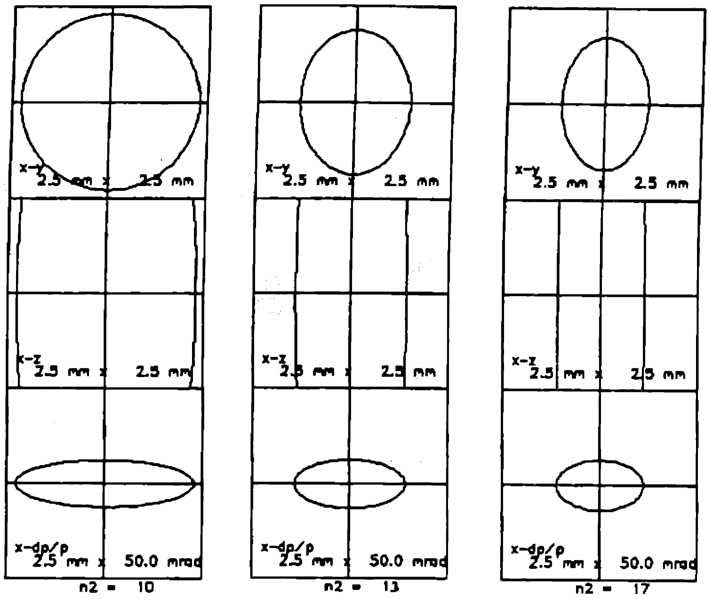

Figure B-6: Beam profiles for revised HEBT system design based upon delivered PMQs.

B.3 Measurements

The magnets were installed on the DL-1 beamline as described above. A quartz beamstop was used to view the beam spot through the scintillation of the quartz produced by the stopping of the 900 keV deuterons. In order to remove the deposited charge on the quartz plate, the surface of the quartz was etched with aluminum oxide paper and a thin layer graphite was used to coat the quartz. As the 8 μA used in the viewing process, the target produces enough neutrons to give a dose rate of approximately 40 μrem/hour (neutrons only) at 2 feet. Thus, the beam profile was viewed through a video camera which displayed a 3x magnified image outside the vault. The beamspot which appeared was obviously far larger than anticipated, as it was occluded by the beamtube prior to reaching the target. This was evident from the perfectly round shape of the very diffuse beamspot and its insensitivity to small changes in the PMQ spacing. It is assumed that the true initial beam parameters were slightly different from those supplied by the DL-1 manufacturer and used in the

TRACE 3-D calculations.

Slight modification of the PMQ spacing resulted in a much beamspot with a much more conventional appearance. This spacing is described in Table B.3.

Region	Element	Length (mm)	Gradient (T/m)	r_i (mm)	r_o (mm)
1	Drift	121.0	—	—	—
2	PMQ	70.0	52.4	15.5	26.7
3	Drift	30.0	—	—	—
4	PMQ	70.0	-36.7	17.7	26.7
5	Drift	116.0	—	—	—
6	PMQ	35.0	48.1	16.0	26.7
7	Drift	124.5	—	—	—
8	Drift	157.0	—	—	—
9	Drift	76.0	—	—	—

Table B.3: HEBT parameters obtained by observation and manual adjustment.

Beam profile measurements with this PMQ spacing were made at three locations. The results of these measurements appear in Table B.4. These measurements (which were at locations approximating the positions of the three differentially pumped apertures) indicated that the beam profile was such that a reasonable portion of the beam would pass through the apertures. However, the measurements were not, per se, physically reasonable. This can be seen from the vertical divergence of the beam between the first and second measurements, and the vertical convergence of the beam between the second and third measurements. This cannot happen with a single beam envelope in a drift space, as there is no focusing element present. However, one can envision a penumbral effect which would be coincident with the primary beam at the first lo-

Position (mm)	Predicted		Measured		Current (mA)
	x-width	y-width	x-width	y-width	
698	3.1	7.0	4.8	7.0	2.5
895	1.2	8.4	2.2	8.1	2.5
1092	1.2	9.5	3.4	4.8	2.5

Table B.4: Beam profile measurements for the HEBT system in Table B.3.

cation, considerably larger at the second location, and outside the accessible angle of view at the third location. However, such a scenario would not give the same current measurement at all three locations unless the penumbra was very small, which was not indicated by the brightness distribution within the beamspot.

The beam was then more accurately aligned, using a level transit to perform a bore sighting as described earlier. This resulted in a physically reasonable beam profile. However, the precision of the measurements of beam spot size was inadequate to evaluate an accurate evolution of the beam. Therefor, the quartz window was located at one of two locations, corresponding to the front and the of the set of differentially pumped apertures, and the magnets adjusted until the beam was of an acceptable size at either end of the region in question. As detailed previously, this resulted in approximately 70% of the beam current being located within a 5 mm spot centered along the aperture line of the target system.

Bibliography

[1] M. R. Hawkesworth. Neutron radiography: Equipment and methods. *Atomic Energy Review*, 15(2):169–220, 1977.

[2] M. Drosg. Drosg-87. Version 4.0 of the computer program published as IAEA-NDS-87, 1987.

[3] John David Carlson. Performance of a high-pressure, high-beam-current gas target. *Nuclear Instruments and Methods*, 113:541–543, 1973.

[4] Eric McFarland and Richard Lanza. Recent advances in neutron tomography. In John M. Carpenter, David B. Cline, Richard Lanza, and David F. Mildner, editors, *Neutrons, X Rays, and Gamma Rays: Imaging Detectors, Material Characterization Techniques, and Applications*, pages 101–111. Proc. SPIE 1737, July 1993.

[5] G. Pfister, A.K. Schatz, C. Siegel, E. Steichele, W. Waschkowski, and T. Bücherl. Nondestructive testing of materials and components by computerized tomography with fast and thermal reactor neutrons. *Nuclear Science and Engineering*, 110(4):303–315, April 1992.

[6] E. Elias and T. Gozani. Accurate hydrogen determination with a dual nuclear gauge. *Nuclear Instruments and Methods in Physics Research, Section A*, 353:691–694, 1994.

[7] M. J. Millen, P. T. Rafter, B. D. Sowerby, M. T. Rainbow, and L. Jelenich. Plant trial of a fast neutron and gamma-ray transmission gauge for the on-belt determination of moisture in lump coke. *International Journal of Radiation Applications and Instrumentation, Part E, Nuclear Geophysics*, 4(2):215–226, 1990.

[8] C. Oliveira and J. Salgado. Analysis of thermal neutron flux distributions in bulk coal by Monte Carlo simulation studies. *International Journal of Radiation Applications and Instrumentation, Part E, Nuclear Geophysics*, 5(3):329–338, 1991.

[9] N. G. Cutmore, P. E. Hartley, B. D. Sowerby, and J. S. Watt. On-line analysis in the Australian coal and mineral industry. *International Journal of Radiation Applications and Instrumentation Part E, Nuclear Geophysics*, 4(3):333–342, 1990.

[10] Siraj M. Khan. Review of neutron-based technologies for the inspection of cargo containers. In George Vourvopoulos and Themis Paradellis, editors, *Neutrons and Their Applications*, pages 386–401. Proc. SPIE 2339, 1995.

[11] T. J. Yule, B. J. Micklich, C. L. Fink, and D. L. Smith. Illicit substance detection using fast-neutron interrogation systems. In George Vourvopoulos and Themis Paradellis, editors, *Neutrons and Their Applications*, pages 414–423. Proc. SPIE 2339, 1995.

[12] W. H. Makky, T. G. Miller, D. L. Smith, J. W. Meadows, and P. T. Guenther. Tailoring neutron spectra for fast neutron spectroscopy. In John M. Carpenter, David B. Cline, Richard Lanza, and David F. Mildner, editors, *Neutrons, X Rays, and Gamma Rays: Imaging Detectors, Material Characterization Techniques, and Applications*, pages 356–367. Proc. SPIE 1737, July 1993.

[13] T. G. Miller and W. H. Makky. Application of fast neutron spectroscopy-radiography (FNS/R) to airport security. In John M. Carpenter, David B. Cline, Richard Lanza, and David F. Mildner, editors, *Neutrons, X Rays, and Gamma Rays: Imaging Detectors, Material Characterization Techniques, and Applications*, pages 184–196. Proc. SPIE 1737, July 1993.

[14] Geoffrey Harding, Richard C. Lanza, Lawrence J. Myers, and Peter A. Young, editors. *Substance Detection Systems.* Proc. SPIE 2092, 1994.

[15] Siraj M. Khan, editor. *Proceedings of The First International Symposium on Explosive Detection Technology*, Atlantic City International Airport, New Jersey, February 1992. FAA Technical Center.

[16] John D. Axe and Robert M. Nicklow. Neutron scattering in condensed-matter physics. *Physics Today*, 38(1):27–35, 1985.

[17] Michael T. Hutchings. Neutron diffraction measurement of residual stress fields—the engineer's dream come true? *Neutron News*, 3(3):14–19, 1992.

[18] G. S. Bauer and R. Bercher, editors. *Proceedings of the 13th Meeting of the International Collaboration on Advanced Neutron Sources.* Paul Scherrer Institut Report PSI Proceedings, November 1995.

[19] Andrew Lawler. U.S. neutron scientists settle for less. *Science*, 273:728–730, August 1996.

[20] Daniel Clery and Andrew Lawler. The looming neutron gap. *Science*, 267:952–954, February 1995.

[21] Barbara Goss Levi. The Advanced Neutron Source knocks at the door of Congress. *Physics Today*, pages 17–19, November 1994.

[22] P. A. Egelstaff and J. M. Carpenter. Miniature neutron sources: thermal neutron sources and their uses in the academic field. In John M. Carpenter, David B. Cline, Richard Lanza, and David F. Mildner, editors, *Neutrons, X Rays, and Gamma Rays: Imaging Detectors, Material Characterization Techniques, and Applications*, pages 330–343. SPIE 1737, July 1993.

[23] Committee on University Research Reactors. *University Research Reactors in the United States—their Role and Value.* National Academy Press, 1988.

[24] Chien Chung, Chih-Ping Chen, and Pao-Shu Chang. Radiation doses from medical *in-vivo* prompt γ-ray activation using a mobile nuclear reactor. *Health Physics*, 55(4):671–683, October 1988.

[25] Eric McFarland and Richard Lanza. Neutron radiography and tomography: The challenge of using non-reactor neutron sources. In *Tomographic Techniques for Industry and Medicine*, Cesena, Italy, October 1991.

[26] Kenneth S. Krane. *Introductory Nuclear Physics.* John Wiley & Sons, Inc., 1987.

[27] Massachusetts Institute of Technology Radiation Protection Office. Analytical x-ray equipment safety program, November 1989.

[28] S. Cierjacks, editor. *Neutron Sources for Basic Physics and Applications.* Pergamon Press, 1983.

[29] G. Petö and R. Pepelnik. High-intensity 14-MeV deuterium-tritium neutron generators: Present achievements and future potential. *Nuclear Science and Engineering*, 106:219–227, 1990.

[30] F. M. Bacon, R. J. Walko, D. F. Cowgill, and A. A. Riedel. Intense neutron source development for use in cancer therapy. *IEEE Transactions on Nuclear Science*, 28(2):1902–1905, April 1981.

[31] F. M. Bacon and A. A. Riedel. Intense neutron source target test facility: A 200 kV, 200 mA dc, deuterium ion accelerator. *IEEE Transactions on Nuclear Science*, 26(1):1505–1508, February 1979.

[32] H. H. Barschall. *Neutron Sources for Basic Physics and Applications*, chapter IV, pages 57–80. Pergamon Press, 1983.

[33] R. Booth, J. C. Davis, C. L. Hanson, J. L. Held, C. M. Logan, J. E. Osher, R. A. Nickerson, B. A. Pohl, and B. J. Schumacher. Rotating target neutron generators. *Nuclear Instruments and Methods*, 145:25–39, 1977.

[34] D. W. Heikkinen, C. M. Logan, and J. C. Davis. Rotating target 14-MeV neutron generators. *Nuclear Science and Engineering*, 106:228–233, 1990.

[35] J. C. Davis, D. W. Heikkinen, J. L. Held, D. M. Logan, and J. E. Osher. RTNS-II neutron sources: Status report. *IEEE Transactions on Nuclear Science*, NS-26(3):3058–3060, June 1979.

[36] D. W. Heikkinen, J. C. Davis, D. J. Massoletti, D. W. Short, and D. B. Tuckerman. The RTNS-II fusion materials irradiation facility. *Journal of Nuclear Materials*, 141–143:1061–1063, 1986.

[37] Kenji Sumita, Akito Takahashi, Toshiyuki Iida, and Junji Yamamoto. Status of OKTAVIAN I and proposal for OKTAVIAN II. *Nuclear Science and Engineering*, 106(3):249–265, November 1990.

[38] Dept. of Electronic, Information and Energy Engineering, Osaka University. Status of OKTAVIAN (online). Available as http://newjapan.nucl.eng.osaka-u.ac.jp/English/Oktavian/Specification/status.html, September 1996.

[39] J. B. Hourst and M. Roche. Design study of a low-energy and high-power accelerator. *Nuclear Instruments and Methods*, 92:589–594, 1971.

[40] R. J. Burke, J. J. Holmes, D. L. Johnson, F. M. Mann, and R. R. Miles. SUPERFMIT an accelerator based neutron source for fusion components irradiation testing. *Nuclear Instruments and Methods in Physics Research B*, 10/11:483–486, 1985.

[41] A. B. M. G. Mostafa. Development and performance of a high-current tritium gas target. *Nuclear Instruments and Methods*, 125:493–496, 1975.

[42] Jacek Guzek. Personal communication, July 1996.

[43] James W. Meadows, Donald L. Smith, and Gerhard Winkler. A high-current deuterium gas target for neutron nuclear data research. *Nuclear Instruments and Methods*, 176:439–442, 1980.

[44] P. Rostek, G. Montagnoli, U. Ratzinger, and H. Morinaga. A mercury jet as gas target window for high current beams. *Nuclear Instruments and Methods in Physics Research, Part A*, A256:251–253, 1987.

[45] D. S. Cramer and L. Cranberg. Gas target for production of monoenergetic neutrons. *Nuclear Instruments and Methods*, 93:405–407, 1971.

[46] H. Klein, H. J. Brede, and B. R. L. Siebert. Energy and angle straggling effects in a D(d,n)^{3}He neutron source using a gas target. *Nuclear Instruments and Methods*, 193:635–644, 1982.

[47] G. E. Cruz, E. D. Erikson, and T. L. Schwab. A vacuum-to-air interface for the advanced test accelerator. *Journal of Vacuum Science and Technology A*, 5(4):2352–2354, July/August 1987.

[48] J. Görres, H. W. Becker, A. Krauss, A. Redder, C. Rolfs, and H. P. Trautvetter. The influence of intense ion beams on the density of supersonic jet gas targets. *Nuclear Instruments and Methods in Physics Research, Part A*, A241:334–338, 1985.

[49] Denis Georges Colombant. *High Intensity 14 MeV Neutron Source.* PhD thesis, Massachusetts Institute of Technology, May 1969.

[50] J. H. Deleeuw, A. A. Haasz, and P. C. Stangeby. Canadian gas target neutron generator research. *Nuclear Instruments and Methods*, 145:119–125, 1977.

[51] G. M. Chenvert, P. M. DeLuca, C. A. Kelsey, and R. P. Torti. A tritium gas target as an intense source of 14 MeV neutrons. *Nuclear Instruments and Methods*, 145:149–155, 1977.

[52] Dale D. Armstrong, C. Robert Emigh, Karl L. Meier, Earl A. Meyer, and J. David Schneider. A 14 MeV intense neutron source facility. *Nuclear Instruments and Methods*, 145:127–148, 1977.

[53] Richard Bartlett Fancher. The effect of high energy absorption in a free expanding fluid flow. Master's thesis, Massachusetts Institute of Technology, August 1968.

[54] Alan Robert Forbes. *Experimental Modeling Study of an Intense 14 MeV Gas Target Neutron Source for the Fusion Materials Program.* PhD thesis, Massachusetts Institute of Technology, May 1978.

[55] D. D. Armstrong, C. R. Emigh, J. C. Hyde, E. A. Meyer, and J. D. Schneider. Tests of the intense neutron source prototype. *IEEE Transactions on Nuclear Science*, 26(3):3055, June 1979.

[56] C. A. Kelsey, G. C. Spalek, P. M. DeLuca, G. M. Chenevert, E. C. McCullough, and R. J. Nickles. High flux fast neutron source for radiation therapy. In *Proceedings of the Workshop on High Intensity Neutron Generators*, pages 147–158. U. S. Atomic Energy Commission, 1972.

[57] T. B. Lucatorto, T. J. McIlrath, and J. R Roberts. Capillary array: a new type of window for the vacuum ultraviolet. *Applied Optics*, 18(14):2505–2509, July 1979.

[58] Keith D. Bonin and T. J. McIlrath. Rotating disk valve for use in a differentially pumped gas system. *The Review of Scientific Instruments*, 55(10):1666–1668, October 1984.

[59] J. Bussière and J. M. Robson. A differentially pumped gas target. *Nuclear Instruments and Methods*, 91:103–107, 1971.

[60] A. H. Kung, N. A. Gershenfeld, C. T. Rettner, D. S. Bethune, E. E. Marinero, and R. N. Zare. XUV generation in pulsed free jets: theory of operation and application to H_2 detection. In S. E. Harris and T. B. Lucatorto, editors, *Laser Techniques in the Extreme Ultraviolet*, pages 10–21. AIP, 1984.

[61] G. Sanna, M. Nardi, and P. Cardoni. Versatile, disturbance-free, electromagnetically driven, supersonic beam source. *Review of Scientific Instruments*, 58(1):26–31, January 1987.

[62] Max Wutz, Hermann Adam, and Wilhelm Walcher. *Theory and Practice of Vacuum Technology*. Friedr. Vieweg & Sohn, 1989.

[63] J. F. Zeigler and J. B. Biersack. *TRIM The Stopping and Range of Ions in Solids*. Pergamon Press, New York, 1990.

[64] ANS-6.1.1 Working Group. American National Standard neutron and gamma-ray flux-to-dose rate factors. Technical Report ANSI/ANS-6.1.1-1977, American Nuclear Society, LaGrange Park, Illinois, 1977.

[65] Murrey D. Goldberg, Said F. Mughabghab, Benjamin A. Magurno, and Victoria M. May. Neutron cross sections. Technical Report BNL-325, Brookhaven National Laboratory, February 1966.

[66] J. I. W. Watterson. Personal communication, November 1995.

[67] J. M. Hall. Personal communication, June 1996.

[68] Michael A. Godin. Mobile neutron sources for residual stress measurement. Master's thesis, Massachusetts Institute of Technology, February 1994.

[69] John R. Lamarsh. *Introduction to Nuclear Engineering*. Addison-Wesley Publishing Company, Inc., second edition, 1983.

[70] L. Templin and M. R. Sims. Reactor physics constants. Technical Report ANL-5800, Argonne National Laboratory, 1963. 2nd edition.

[71] T. Lauritsen and F. Ajzenberg-Selove. Energy levels of light nuclei. In *Nuclear Data Sheets*. National Academy of Research Council, 1961.

[72] Editor Judith F. Briesmeister. *MCNP^{TM}—A General Monte Carlo N-Particle Transport Code*. Los Alamos National Laboratory, November 1993. Version 4A.

[73] K. R. Crandall. TRACE 3-D documentation. Technical Report LA-UR-90-4146, Los Alamos National Laboratory, December 1990. Revision of LA-11054-MS, August 1987.